

POLITECNICO DI TORINO

Master Degree in Civil Engineering



Master Thesis

Torsional instability of open thin-walled beams: Numerical and experimental investigation

Tutors

Prof. Alberto Carpinteri

Dr. Gianfranco Piana

Candidate

Giorgia Aquaro

December 2018

To the people who have
always believed in me.

Acknowledgements

I would like to thank all the people who have supported me in this important task and helped me in writing my thesis with their observations, suggestions and critics.

First of all, thank you Professor Alberto Carpinteri for giving me this assignment.

Secondly, I want to say thank you in particular to Doctor Gianfranco Piana for his constant support in the realization of this work.

Finally, last but not least, I have to thank my family, my parents, my sisters who have contributed incessantly and immensely to my personal formation.

The experimental work of this thesis, conducted at the MASTRLab of Politecnico di Torino, is part of a research project on “Numerical and experimental investigations on the static stability of thin-walled beams” promoted by Professor Giuseppe Ruta of Sapienza University of Rome, whose financial support is gratefully acknowledged.

The Company La Milano srl is also gratefully acknowledged for the accurate realization of the specimens.

Thanks very much indeed!

Abstract

The present thesis deals with the structural instability of axially compressed thin-walled beams with open cross-section. Experimental and numerical (FEM) results will be shown for cruciform section beams with stiffeners placed in different positions. Such stiffeners are represented by longitudinal plates, which connect the flanges on a beam portion, thus providing intermediate warping restrictions.

This work is structured into five chapters.

Chapter 1 is an introductory chapter in which the problem is framed and early studies are mentioned.

Chapter 2 gives some remarks on the instability of thin-walled beams subject to compressive axial load.

Chapter 3 presents the experimental set-up and the instrumentation used to investigate buckling, as well as the programs used for data acquisition and processing. Furthermore, this chapter describes the experimental campaign and the results obtained under two end warping constraint conditions, i.e. free and (partially) restrained warping.

Chapter 4 is devoted to the numerical analyses. The numerical simulations were implemented in Lusas finite element code, and the results were compared with the experimental ones.

Finally, chapter 5 presents some conclusive considerations regarding the results obtained.

Contents

Acknowledgements	v
Abstract	vii
Chapter 1 Introduction	1
Chapter 2 Remarks on the flexural-torsional buckling of compressed thin-walled beams with open section	8
2.1 Torsional buckling of compressed beams	8
2.2 Flexural-torsional buckling of compressed beams	13
Chapter 3 Experimental campaign	19
3.1 Instrumentation used in the experimental campaign	19
3.1.1 Laser	19
3.1.2 Acquisition device	20
3.1.3 Control system	21
3.2 Stability test	23
3.2.1 Geometric and mechanical characteristic of the specimens	24
3.2.2 Description of the stability test	25
3.2.3 Constraint system	26
3.3 Results of the experimental campaign	27
3.4 Comparison of experimental results	48
Chapter 4 Numerical simulations and comparisons	49
4.1 Free warping	50
4.2 Fully-restrained warping	59
4.3 Mixed conditions	66
4.4 Further models	73
4.5 Comparisons between numerical simulations and experimental campaign	77
4.6 Comparisons between stiffened, uniform and weakened beam	81
4.7 Comparisons between beams with different stiffener	81
Chapter 5 Conclusion	83
References	85

Chapter 1

Introduction

The main problem in civil engineering is collapse. This can happen for two basic reasons:

- the material overcomes its resistance so the structure reaches unbearable stress levels;
- the structure loses stability and collapses because its stress levels are lower than the resistance limits of the materials;

The present thesis focuses on the structural instability of open thin-walled beams. In particular, the static behaviour of compressed beams of cruciform section (double I) with stiffeners placed in different positions, was investigated experimentally and numerically.

The stiffeners (buttens) are designed to increase the stiffness against cross-sectional warping. I have conducted an experimental campaign and a numerical analysis where two end constraint conditions were used: free warping and restrained warping. In this way a static stability study was carried out for each specimen to identify the buckling load. The results obtained were compared with the results from other experimental campaigns and finite element models.

In structural engineering, cruciform-sections are mostly used for compressed elements such as columns. Slender elements with cruciform sections are subject to compression instability which is generally manifested by pure torsion which consists in twisting around its own axis. This phenomenon will be dealt with in the next chapters.

In Italy the most important structure with cruciform columns is the De Cecco Headquarters in Pescara (figure 1.2), designed by Massimiliano Fuksas.

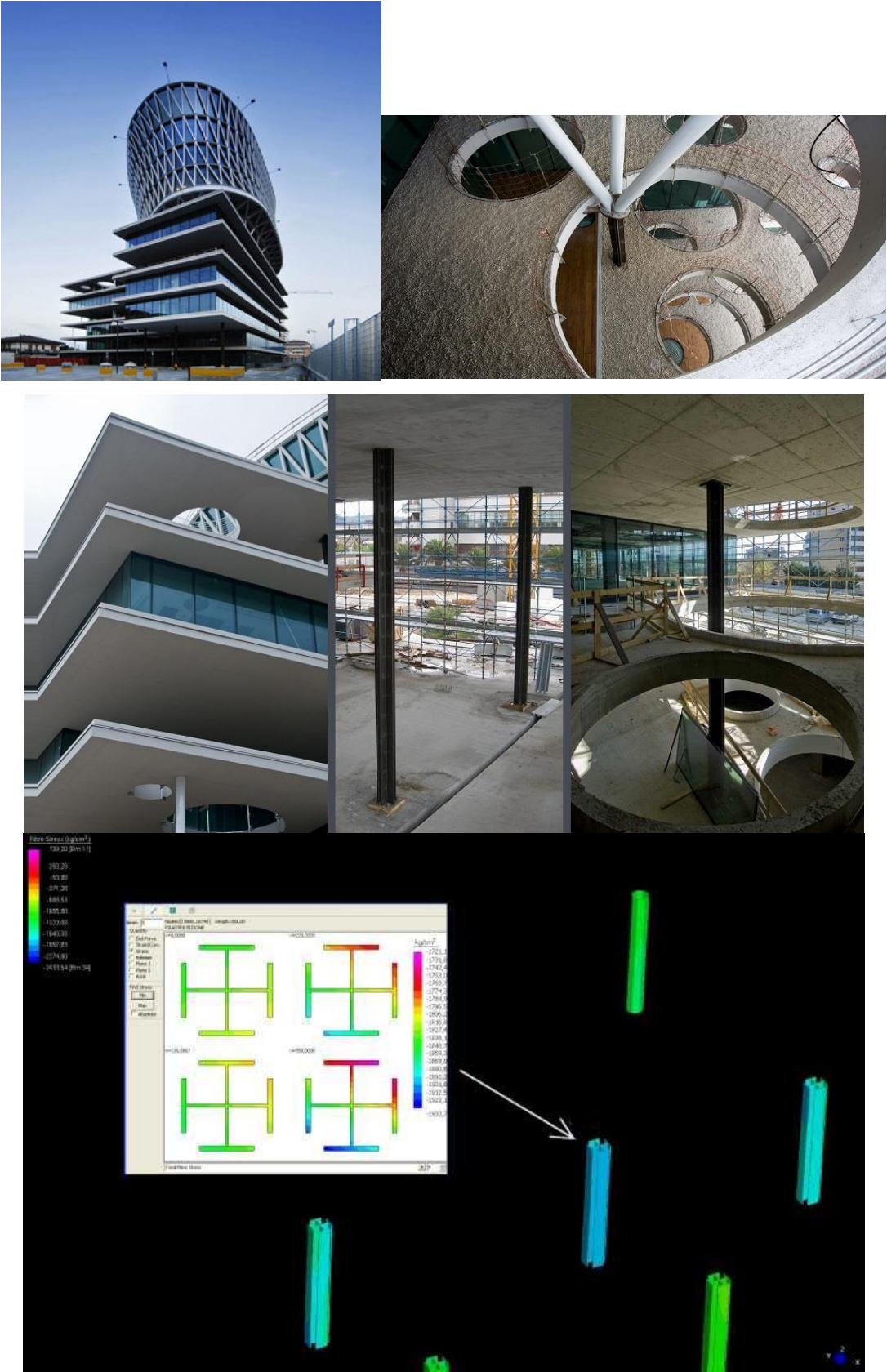


Figure 1.2 – Directional pole De Cecco

Before this thesis, other studies were carried out on compressed thin-walled beams with a double I symmetric section in aluminum in order to identify the buckling load. To test these

beams, a universal testing machine (MTS) and piezoelectric pickups were used. The specimens were tested under two axial constraint conditions, these are free and partially restrained warping of the end sections. The specimens were therefore subjected to increasing compressive axial displacement up to the post-buckling condition. Following this approach, several specimens were tested in order to study the effects of warping rigidity on buckling loads. The instability that has occurred is torsional, so the cross-section rotates around the beam axis, which remains straight.

Considering the beam in a free warping condition, the experimental critical load is about 16 kN, while the value given by the FEM is 16.5 kN. On the other hand, considering the beam in a semi-restrained warping condition, the experimental critical load is about 22 kN, while the value given by the FEM, for a fully restrained end warping, is 38.4 kN.

The buckled shape of the beam is similar in both constraint conditions. The difference is in the warping of the end sections, in one case it happens and in the other it doesn't.



Figure 1.3 - (a) Instability of the beam in the free warping condition: torsion buckling mode, detail of warping of the end sections. (b) Instability of the beam in the partially (experiments) and fully (FEM models) restrained warping condition: torsion buckling mode, detail of the end sections and top view of the plastic post-buckling twisted configuration.

The experimental results show an influence of warping and warping constraints. It was noticed that there was an increase of buckling loads due to the restriction of warping deformation of the end sections. (G. Piana et al., 1, 2017)

Another study was conducted before this thesis. It investigated the effect of an internal warping constraint (intermediate stiffener) on the stability of the same thin-walled profile. The stiffener connected the external flanges of the cross-section in such a way as to provide a four-cell box section.

Through numerical simulations, conducted by a finite difference (FD) model, it was shown that the introduction of a local stiffening could increase the critical load for torsion buckling

when the profile was axially compressed. However, the result also indicated that a wrong position of the stiffener (around the midpoint of the beam) could decrease the critical load. This is a counterintuitive result that requires a validation. The experiments and the numerical (FEM) simulations of the present thesis aim at a deeper investigation of this problem.

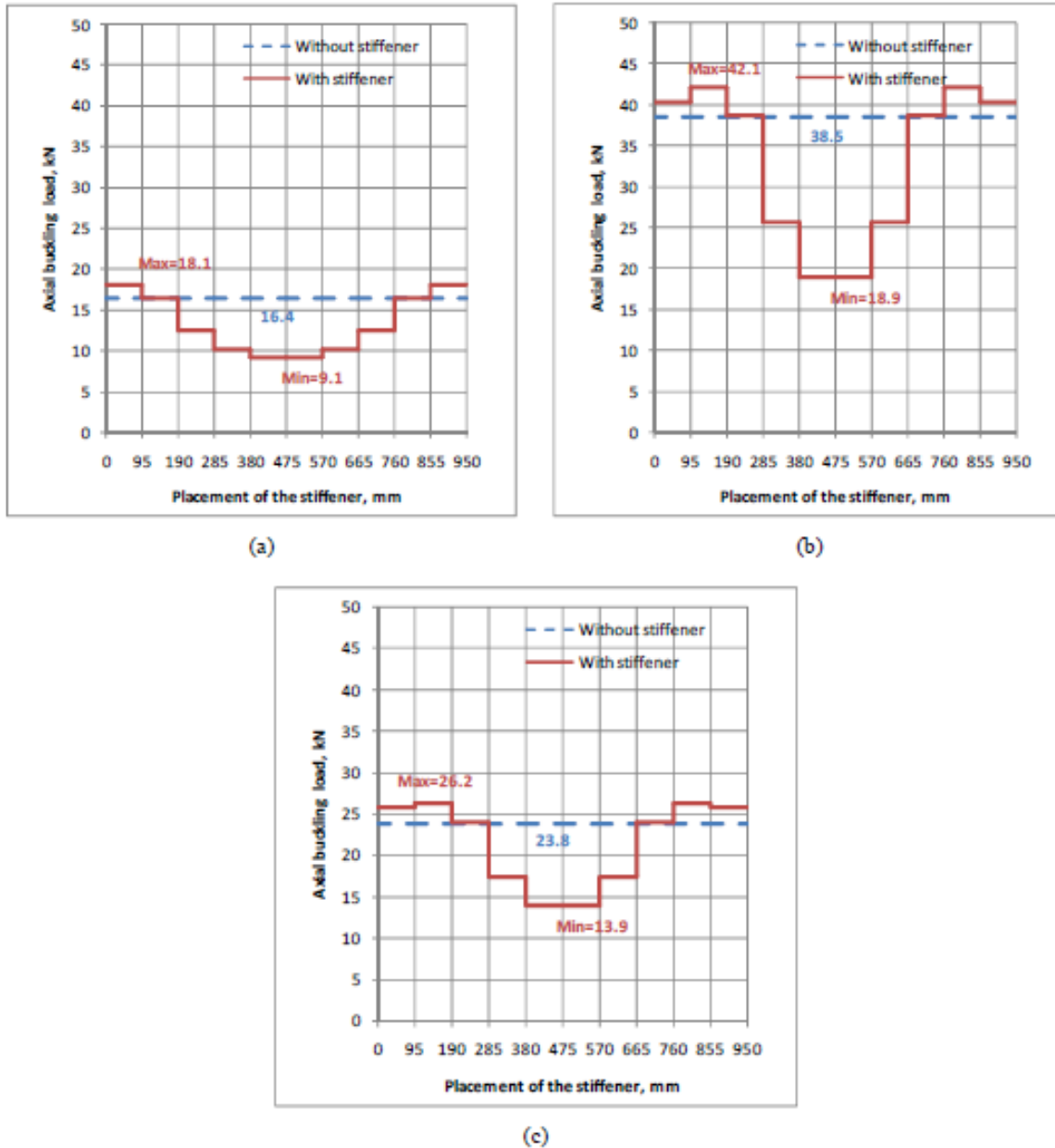


Figure 1.4 – Buckling compressive loads vs. locations of the stiffened cross-section: (a) free, (b) fully restrained, and (c) semi-restrained warping conditions.

For example, considering the beam with stiffness placed near one of the ends, in the condition of free warping in both ends of the beam, the critical load can increase up to 10%. If warping of both beams ends is restrained, the maximum increase is reached when the stiffener is placed between $l/10$ and $2l/10$, with a percentage gain of about 9% and 10%, for the fully and semi-restrained case, respectively. While the maximum decrease of the critical

loads is attained around midpoint of the beam, with a percentage gain of about 45%, 51%, and 42% for free, fully and semi-strained warping, respectively. (G. Piana et al., 2, 2017)

Finally, the last study I considered, was about the same cruciform beam but this time characterized by a localized cross-section reduction introduced by removing a small portion of the flanges on the beam. The reduction was 10 mm and simulated a local damage. This yielded a cruciform cross-section with negligible warping stiffness on a beam portion (10 mm). Also in this study, the beam was analyzed under free, semi-, and fully restrained warping at its ends. Comparing the damaged beam with the undamaged beam, a decrease of the buckling loads was found of 46%, 14% and 18% respectively for free, semi- and fully restrained warping conditions. At the end of the test the beam underwent a torsion buckling with the maximum rotation at the weakened section. (G. Piana et al., 3, 2017)

The studies mentioned above were developed at the Politecnico di Torino in cooperation with Sapienza University of Rome. Other studies concerning torsion, warping and stiffening emerged from bibliographic research.

Figure 1.4, taken from some lecture notes of Prof. P. Gelfi at University of Brescia, illustrates the effect of different stiffening plates on the torsion (uniform vs. non-uniform) of in I beam.

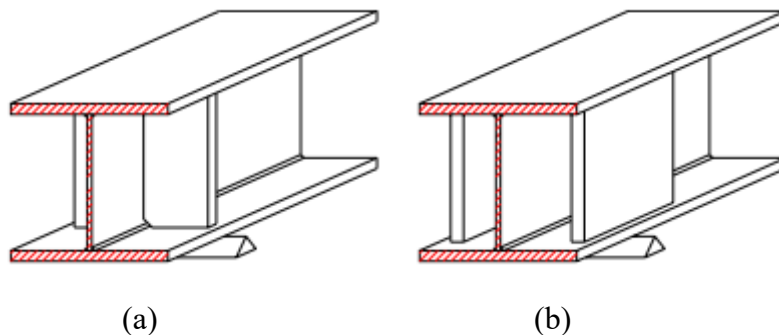


Figure 1.4 – (a): Torsional support; (b): semi-interlocking torsion.

Figure 1.4 (a) shows the case where the constraint is able to prevent the torsional rotation but not the warping. Conversely, Figure 1.4 (b) shows the case where warping is (at least partially) prevented.

In the first case there is pure torsion, while in the second one the stress state is called non-uniform torsion and it occurs when sectional warping is not constant along the beam due to the presence of the constraints or because the torque varies. (P. Gelfi, http://gelfi.unibs.it/lezioni_acciaio/Lezione10.pdf)

An article was written at Gdansk University of Technology dealing with “numerical simulation of a thin-walled beam with warping stiffeners undergoing torsion”.

Thin-walled beams with open cross-section have relatively small torsional stiffness. The performance of the structure can be considerably improved by adding some constructional

stiffeners like battens. This types of stiffeners partially prevent cross-section warping, as pointed out before.

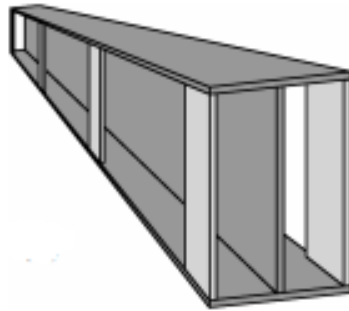


Figure 1.5 – Battens in I-beam

Numerical simulations performed for thin-walled beams with constructional stiffeners pointed out the essential influence of the analyzed stiffeners on the torsional behaviour of the structure. In fact they noticed that adding battens, the torsional rigidity of beams is increased by 64%. (Kreja and Szymczak, 2002)

Another very interesting article is written by Svensson and Plum, entitled "Stiffener Effects on Torsional Buckling of Columns". This paper presents an analytical evaluation of the effect of locally placed stiffeners. The section taken into consideration was the following:

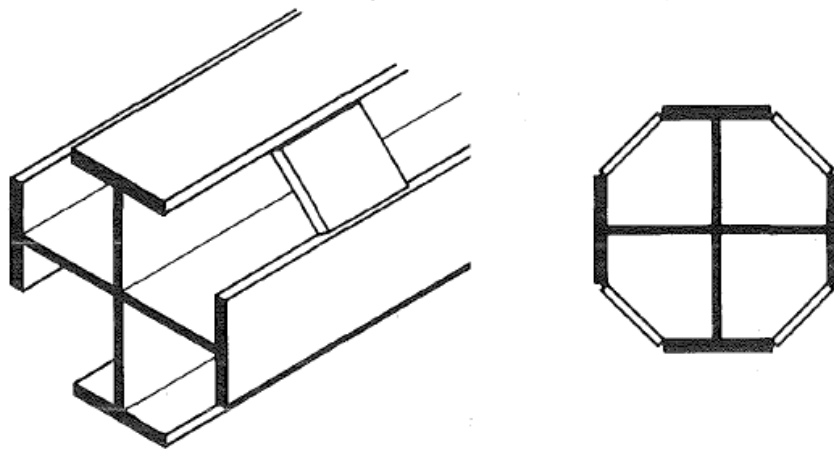


Figure 1.6 - Stiffening arrangement and stiffened section

These stiffeners are necessary to improve the torsional stability properties as they prevent or partially prevent warping.

The torsional buckling load for a column pinned at both ends is

$$P_{\theta} = \frac{C_1}{r^2 L^2} (\pi^2 + \beta^2)$$

While the torsional buckling load of the stiffened column is

$$P_{\theta_{stiff}} = \frac{C_1}{r^2 L^2} (\rho_{\theta}^2 + \beta^2)$$

Where:

- $\beta^2 = \frac{CL^2}{C_1}$. In this equation L is the length of the column, and C and C_1 are the torsional and warping rigidities.

- $r = \sqrt{(I_x + I_y)/A}$ is the polar radius of gyration.

It can be seen by comparing this expression for the unstiffened column, the effect of the stiffeners is measured by the value of $\rho_\theta \cdot \rho_\theta$ is a function of stiffeners position z_0 and stiffness k.

Two special cases are treated in detail. This allows for a quantitative measure of the effect of stiffeners as a function of their dimensionless warping restraint stiffness, k, and position. The column is supposed to have been pin supported at the ends. First, the case of one stiffener is investigated. It is demonstrated that the optimum position z_0 , measured from the end of the column, is 0.219L for $k \rightarrow \infty$ and slightly smaller for finite values of k. The case of two stiffeners symmetrically placed with respect to the column midspan is characterized by the presence of anti-symmetrical as well as symmetrical modes. As $k \rightarrow \infty$ anti-symmetrical modes are decisive for the stiffeners being placed between 0.15L and 0.25L from the ends. For $k < 27$ only symmetrical modes are of the interest irrespective of the position of the stiffeners.

Figure 1.7 shows an analogy between the section studied in that article and the one of this thesis. In chapter 4 a comparative analysis will be made in numerical terms. (S. E. Svensson et al., 1983)

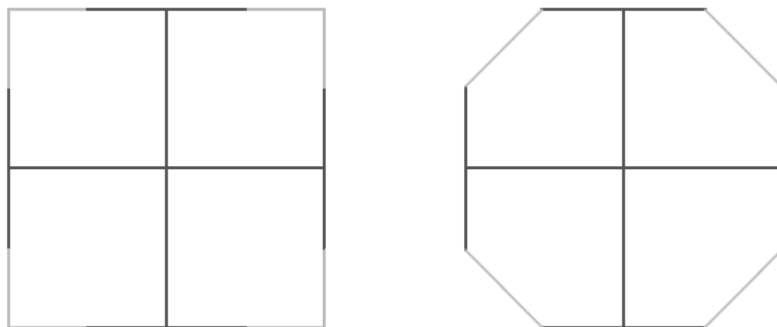


Figure 1.7 – (a) Stiffened section of the thesis; (b) Stiffened section of the article

Chapter 2

Remarks on the flexural-torsional buckling of compressed thin-walled beams with open section

Thin-walled open sections are characterized by very small torsional stiffness, so that buckling may occur with a twisting of the sections around a longitudinal axis (torsional instability), possibly accompanied by an inflection in one or both main planes of inertia (flexural-torsional instability).

2.1 Torsional buckling of compressed beams

Straight-axis beams subjected to axial load may be subjected to torsional balanced deformation.

We consider a beam with an open thin section and thickness δ variable with curvilinear abscissa s . The invariability of the shape of the section is assumed. Furthermore, the section can be variable with the abscissa z but the shear centres C are aligned and the straight line z of the centres cannot be deformed. The beam is loaded by axial compression forces. Deformation is characterized by the rotation θ of the straight section around the z axis, coinciding with the straight line of the shear centres. The derivative of θ represents the angle of rotation between two distant sections of the length unit.

$$\theta' = \frac{d\theta}{dz} \quad (2.1)$$

Due to the torsional deformation, the AP element is positioned in such a way as to determine the P'AP plane (figure 2.1).

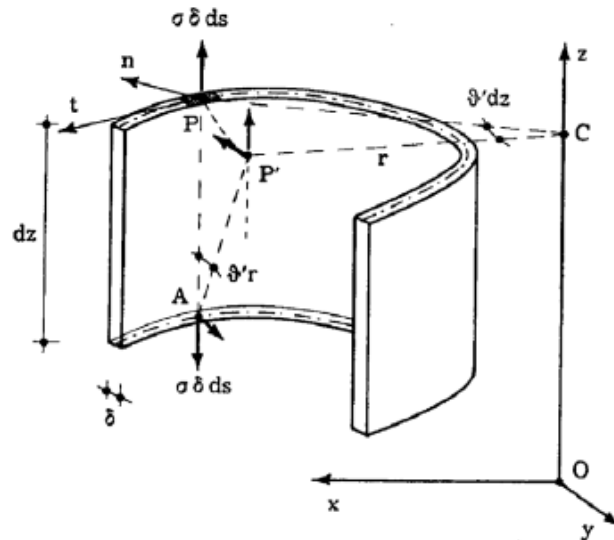


Figure 2.1 - Beam with an open thin section

The $\sigma \delta s$ forces applied in A and P' are no longer in equilibrium and for this reason they give rise to a moment $\sigma \delta s \theta' r$ that is equivalent to that of two $\sigma \delta s \theta' r$ forces. The $\sigma \delta s \theta' r$ force acting on the straight section of positive normal provides, for $\sigma > 0$ and $\theta' > 0$, a negative moment with respect to the centre C:

$$M_{tn} = -\frac{N}{A} \theta' \int_A \delta ds r^2 = -\frac{N}{A} \theta' I_c \quad (2.2)$$

where A represents the area of the straight section, and I_c its polar moment with respect to C. As already mentioned, the shear are aligned so that the torsion equation is

$$C_2 \theta^{IV} + C'_2 \theta''' - C_1 \theta'' - C'_1 \theta' = m_t = -\frac{dM_t}{dz} \quad (2.3)$$

where:

- $C_1 = G \frac{\int \delta^3 ds}{3}$ is the (primary or St. Venant) torsion rigidity;
- $C_2 = E \int_s (2A_s)^2 \delta ds$ is the warping rigidity (secondary, or Vlasov, torsion rigidity), A_s is the sectorial area;
- m_t is the distributed moment applied on the lateral surface.

Normal stress modifies (2.3) as follows

$$C_2 \theta^{IV} + C'_2 \theta''' - C_1 \theta'' - C'_1 \theta' = -\frac{dM_t}{dz} - \frac{dM_{tn}}{dz} = -\frac{dM_{tn}}{dz} + m_t \quad (2.4)$$

and replacing

$$C_2 \theta^{IV} + C'_2 \theta'''' - (C_1 + \frac{NI_c}{A}) \theta'' - (C_1 + \frac{NI_c}{A})' \theta' = m_t \quad (2.5)$$

Setting $M = 0$, (2.5) becomes the equation of varied equilibrium.

When the section is constant and the beam is loaded only at the ends by an axial force $N = -F$, the equation of varied equilibrium is written

$$C_2 \theta^{IV} - (C_1 + F \frac{I_c}{A}) \theta'' = 0 \quad (2.6)$$

To write the equation (2.6) in a more compact way, we place

$$k^2 = - \frac{C_1 - F \frac{I_c}{A}}{C_2} \quad (2.7)$$

So (2.6) becomes

$$\theta^{IV} + k^2 \theta'' = 0 \quad (2.8)$$

the solution of which is

$$\theta = A \text{ sen } kz + B \cos kz + C z + D \quad (2.9)$$

If the ends have constraints that prevent the rotation around the z axis $\theta = 0$, but not the warping $w \neq 0$, conditions at the limits are

$$\begin{aligned} z = 0 & \quad \theta = \theta'' = 0 \\ z = l & \quad \theta = \theta'' = 0 \end{aligned} \quad (2.10)$$

that for (2.9) are written

$$\begin{aligned} 0 &= B + D \\ 0 &= -k^2 B \\ 0 &= A \text{ sen } kl + B \cos kl + Cl + D \\ 0 &= -k^2 A \text{ sen } kl - k^2 B \cos kl \end{aligned}$$

The compatibility condition is

$$\begin{vmatrix} 0 & 1 & 0 & 1 \\ 0 & -k^2 & 0 & 0 \\ \text{sen } kl & \cos kl & 1 & 1 \\ -k^2 \text{ sen } kl & -k^2 \cos kl & 0 & 0 \end{vmatrix} = 0$$

which offers the solution

$$kl = n\pi \quad (2.11)$$

which corresponds to A undetermined and finite, B = C = D = 0.

For the (2.7)

$$F_a = \frac{A}{I_c} \left(C_1 + \frac{n^2 \pi^2}{l^2} C_2 \right) \quad (2.12)$$

at (2.12) corresponds the solution

$$\theta = A \text{ sen } \frac{n\pi z}{l} \quad (2.13)$$

in this case

$$F_c = \frac{A}{I_c} \left(C_1 + \frac{\pi^2}{l^2} C_2 \right) \quad (2.14)$$

If the ends have constraints that prevent both the rotation around the z axis and the warping, the conditions at the limits are

$$\begin{aligned} z = 0 & & \theta = \theta' = 0 \\ z = l & & \theta = \theta' = 0 \end{aligned} \quad (2.15)$$

that are written

$$\begin{aligned} 0 &= & B & + D \\ 0 &= kA & + C \\ 0 &= A \text{ sen } kl + B \cos kl + Cl + D \\ 0 &= k^2 A \cos kl - k^2 B \text{ sen } kl + C \end{aligned}$$

The compatibility condition is

$$\begin{vmatrix} 0 & 1 & 0 & 1 \\ k & 0 & 0 & 0 \\ \text{sen } kl & \cos kl & 1 & 1 \\ k \cos kl & -k \text{sen } kl & 0 & 0 \end{vmatrix} = 0$$

whose solutions are

$$\text{sen } \frac{kl}{2} = 0 \quad (2.16)$$

and

$$\text{tg } \frac{kl}{2} = \frac{kl}{2} \quad (2.17)$$

(2.16) offers

$$\frac{kl}{2} = n\pi \quad (2.18)$$

from which

$$F_a = \frac{A}{I_c} \left(C_1 + \frac{4 n^2 \pi^2}{l^2} C_2 \right) \quad (2.19)$$

in this case

$$F_c = \frac{A}{I_c} \left(C_1 + \frac{4 \pi^2}{l^2} C_2 \right) \quad (2.20)$$

This is true if the line z of the shear centres is constrained. In the absence of a constraint along z, when the centre of shear C coincides with the centre of gravity G, the previous formulas are valid. On the other hand, if $C \neq G$, in absence of a long constraint z, we must consider a flexion-torsional configuration.

2.2 Flexural-torsional buckling of compressed beams

If the centre of shear and the centre of gravity do not coincide, the equations of the deformed configuration can be obtained by effect of distributed applied torques m_t by first imposing the constraint along the straight line of the shear centres and then removing it.

The hypotheses that govern the treatment are:

- Constant section;
- Forces F applied to the ends.

In the presence of the constraint the θ rotation are provided by the (2.6). The normal stress $N(z)$ gives rise to the reactions $r(z)$ parallel to the xy plane, whose axes are parallel to the main axes of inertia ξ and η .

The $r(z)$ reactions generate shears in each section

$$T_{rx} = -\sigma \theta' \int_A y dA = -\sigma \theta' S_x \quad (2.21)$$

$$T_{ry} = -\sigma \theta' \int_A x dA = -\sigma \theta' S_y$$

By removing the constraint we need to apply the $-r(z)$ reactions which generate the shears

$$T_x = \sigma \theta' S_x = \sigma \theta' A y_G$$

$$T_y = \sigma \theta' S_y = -\sigma \theta' A x_G \quad (2.22)$$

that is, the displacements u and v governed by the equations

$$EI_\eta u'' = -F u - \sigma \theta A y_G = -F (u - \theta y_G) \quad (2.23)$$

$$EI_\xi v'' = -F v + \sigma \theta A x_G = -F (v + \theta x_G)$$

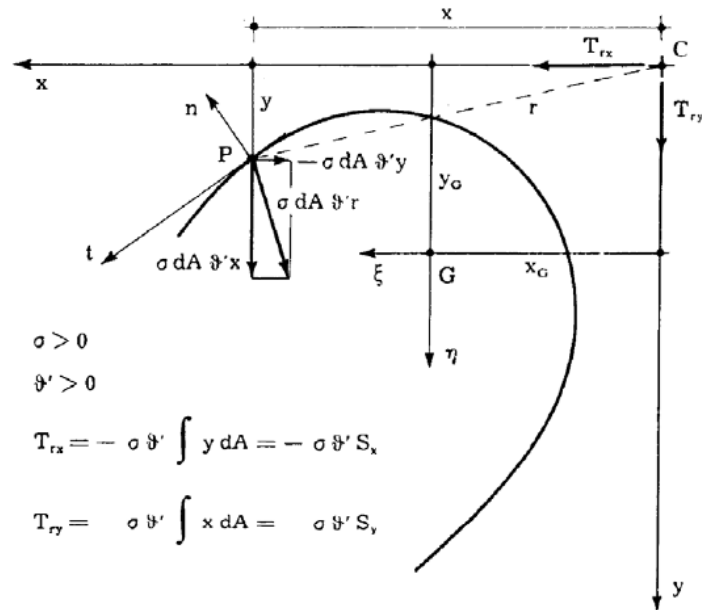


Figure 2.2 - Beam with open thin section and nomenclature

The inflection of components $u(z)$ and $v(z)$ causes the inclinations $u'(z)$ and $v'(z)$ of the normal to the straight section with respect to the z axis; the normal projections of the F on the straight section of positive normal thus inclined are provided by Fu' and Fv' . In this way the extra torque rises

$$M_{ts} = -F u' y_G + F v' x_G \quad (2.24)$$

in the presence of m_t applied, (2.6) changes

$$C_2 \theta^{IV} - (C_1 + F \frac{I_c}{A}) \theta'' = m_t - \frac{dM_{ts}}{dz} = m_t + F u'' y_G - F v'' x_G \quad (2.25)$$

Therefore the equations of the deformed configuration are

$$EI_\eta u'' = -F (u - \theta y_G)$$

$$EI_\xi v'' = -F (v + \theta x_G) \quad (2.26)$$

$$C_2 \theta^{IV} - (C_1 + F \frac{I_c}{A}) \theta'' - F u'' y_G + F v'' x_G = m_t$$

The equation of varied equilibrium are obtained by setting $m_t = 0$

$$EI_{\eta} u'' + F (u - \theta y_G) = 0$$

$$EI_{\xi} v'' + F (v + \theta x_G) = 0 \quad (2.27)$$

$$C_2 \theta^{IV} - (C_1 + F \frac{I_c}{A}) \theta'' - F u'' y_G + F v'' x_G = 0$$

If the ends are bound with common and torsional supports, the limit conditions are

$$\begin{aligned} z = 0 \quad \text{and} \quad z = l \quad & u = v = \theta = 0 \\ z = 0 \quad \text{and} \quad z = l \quad & u'' = v'' = \theta'' = 0 \end{aligned} \quad (2.28)$$

If $x_G = y_G = 0$ the critical solutions of (2.27) are

$$F_x = n^2 \pi^2 \frac{EI_{\xi}}{l^2}$$

$$F_y = n^2 \pi^2 \frac{EI_{\eta}}{l^2} \quad (2.29)$$

$$F_{\theta} = \frac{A}{I_c} (C_1 + \frac{n^2 \pi^2}{l^2} C_2)$$

In the case of $C \neq G$ a set of functions $u v w$ that satisfy the conditions at the limits (2.28) is

$$u = A_x \text{sen} \frac{n \pi z}{l}$$

$$v = A_y \text{sen} \frac{n \pi z}{l} \quad (2.30)$$

$$\theta = A_{\theta} \text{sen} \frac{n \pi z}{l}$$

as the section is constant, it also satisfies the (2.27) if it occurs

$$\begin{aligned}
 \left(F - EI_{\eta} \frac{n^2 \pi^2}{l^2}\right) A_x & & - F y_G A_{\theta} & = 0 \\
 \left(F - EI_{\xi} \frac{n^2 \pi^2}{l^2}\right) A_y & & + F x_G A_{\theta} & = 0 \\
 -F y_G A_x & & + F x_G A_y - \left(C_2 \frac{n^2 \pi^2}{l^2} + C_1 - F \frac{I_c}{A}\right) A_{\theta} & = 0
 \end{aligned}$$

and still, with the positions (2.29), if it is

$$\begin{vmatrix}
 F - F_y & 0 & -F y_G \\
 0 & F - F_x & F x_G \\
 -F y_G & F x_G & \frac{I_c}{A} (F - F_{\theta})
 \end{vmatrix} = 0$$

The cubic equation of the previous formulation can also be written

$$\frac{I_c}{A} (F - F_x)(F - F_y)(F - F_{\theta}) - F^2 y_G^2 (F - F_x) - F^2 x_G^2 (F - F_y) = 0$$

and calling I_G the centroidal polar moment,

$$\begin{aligned}
 f(F) = \frac{I_G}{I_c} F^3 + \left[\frac{A}{I_c} (F_x y_G^2 + F_y x_G^2) - (F_x + F_y + F_{\theta}) \right] F^2 + & \quad (F_x F_y \quad (2.31) \\
 F_x F_{\theta} + F_y F_{\theta}) F - F_x F_y F_{\theta} = 0 &
 \end{aligned}$$

The (2.31) provides three roots for F , an infinite number of these terms exist, ordered by increasing n . For $n = 1$ the smallest of the three roots provides the critical value of F .

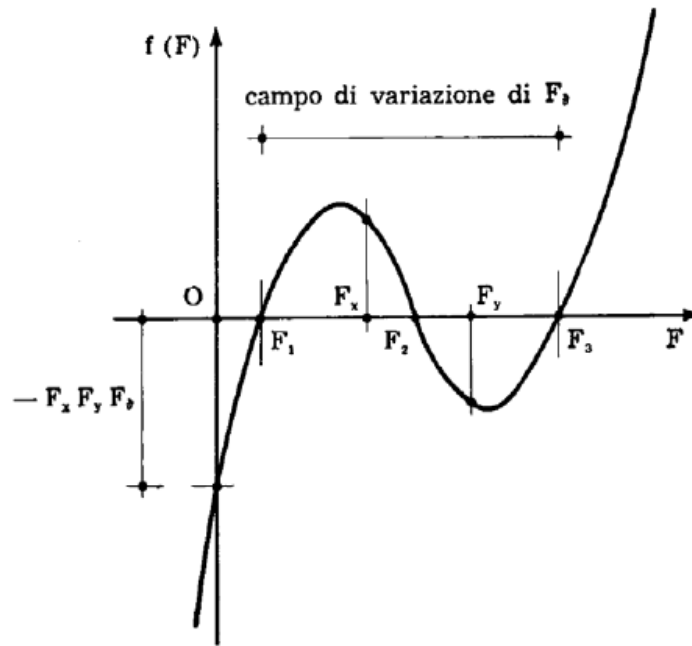


Figure 2.3 - Graph of the function $f(F)$

Intersections with the F axis provide the F_a values.

For $F = 0$, $f(F)$ is negative; for very high F , $f(F)$ takes the sign of the cubic term, which is positive.

If $F_x < F_y$:

$$f(F_x) = -\frac{A}{I_c} F_x^2 x_G^2 (F_x - F_y) > 0$$

$$f(F_y) = -\frac{A}{I_c} F_y^2 y_G^2 (F_y - F_x) < 0$$

So the (2.31) has three real roots $F_1 F_2 F_3$ and disagreements are valid

$$F_1 < F_x < F_2 < F_y < F_3$$

If F_θ is smaller than F_x and F_y , $f(F_\theta)$ is positive; in fact it is

$$f(F_\theta) = \frac{A}{I_c} F_\theta^2 [x_G^2 (F_y - F_\theta) + y_G^2 (F_x - F_\theta)] > 0$$

So also, if F_θ is greater than F_x and F_y , $f(F_\theta)$ is negative. However, this means

$$F_1 < F_\theta$$

$$F_3 > F_\theta$$

It is therefore concluded that of the three roots $F_1 F_2 F_3$ the smallest, F_1 , it is less than F_x , F_y , F_θ and the biggest, F_3 , is bigger than F_x , F_y , F_θ ; the second F_2 is intermediate between F_x and

F_y . The in-game call of torsional deformations lower the value of the Eulerian critical load. For beams of modest length and rigid section the instability is torsional. If instead the beam is long and with a rigid section, the Euler formula gives exact values.

If the ends are bound with common and torsional fixed joints, the limit conditions are

$$\begin{aligned} z = 0 \quad \text{and} \quad z = l \quad & u = v = \theta = 0 \\ z = 0 \quad \text{and} \quad z = l \quad & u' = v' = \theta' = 0 \end{aligned} \quad (2.32)$$

The first two (2.27) are modified as follows

$$\begin{aligned} EI_\eta u'' + F(u + \theta y_G) - EI_\eta(u'')_0 &= 0 \\ EI_\xi v'' + F(v + \theta x_G) - EI_\xi(v'')_0 &= 0 \end{aligned} \quad (2.33)$$

$$C_2 \theta^{IV} - (C_1 + F \frac{I_c}{A}) \theta'' + F u'' y_G - F v'' x_G = 0$$

A solution that satisfies them is

$$\begin{aligned} u &= A_x \left(1 - \cos 2 \frac{n \pi z}{l}\right) \\ v &= A_y \left(1 - \cos 2 \frac{n \pi z}{l}\right) \\ \theta &= A_\theta \left(1 - \cos 2 \frac{n \pi z}{l}\right) \end{aligned} \quad (2.34)$$

to be satisfied (2.33) with the null solution, it must be

$$\begin{vmatrix} F - EI_\eta A \frac{n^2 \pi^2}{l^2} & 0 & F y_G \\ 0 & F - EI_\xi A \frac{n^2 \pi^2}{l^2} & -F x_G \\ F y_G & -F x_G & \frac{I_c}{A} \left[F - \frac{A}{I_c} (C_1 + 4 \frac{n^2 \pi^2}{l^2} C_2) \right] \end{vmatrix} = 0$$

The equation that holds F is still the (2.31) and the solution process is the same.

Chapter 3

Experimental campaign

In this chapter we will present the instruments used in the experimental campaign, the type of test performed and finally the results obtained.

Static monotonic compression tests have been performed to determine the buckling load and the tested structure was a cruciform cross-section beam with end flanges and stiffeners placed in different positions in order to find the best configuration to make the beam more resistant.

To have the correct measurement of the quantity to be analyzed, it is necessary to define a set-up, in our case this is composed of:

- Structure to analyse;
- Sensor able to register the signal;
- Conversion system (acquisition device) that converts the signal from analogical to digital;
- Control system that saves processes and makes the digital signal analysable.

3.1 Instrumentation used in the experimental campaign

3.1.1 Laser

The sensor used in the experimental campaign was a laser which detected transverse displacements at a point.

The laser sensor is the opto NCDT 1302-20, a triangulating displacement transducer produced by Micro-Epsilon. It is a highly performing instrument that detects displacement in a precise and accurate manner. The advantage of this sensor is that it is noncontact one and therefore does not alter the behaviour of the object tested.



Figure 3.1 – Photo of laser opto NCDT 1302-20

The working principle is the classic one of triangulation. A laser diode projects a beam on the surface of the object and the reflected beam is captured by the sensor. The distance is calculated through a simple geometric algorithm.

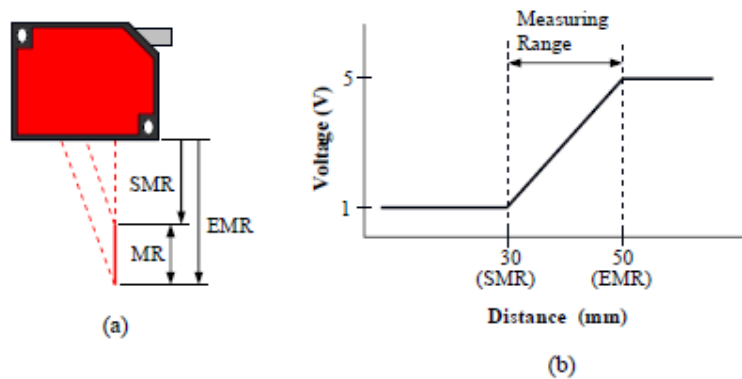


Figure 3.2 - Scheme of adopted laser triangulating displacement sensor (a) and corresponding characteristic curve (b) with indication of Start of Measuring Range (SMR) and End of Measuring Range (EMR).

Table 3.1. shows the main characteristics of the laser sensor:

Measuring Range (MR)	Start of Measuring Range (SMR)	Midrange (MR)	End of Measuring Range (EMR)	Resolution (Dynamic 750 Hz)
20 mm	30 mm	40 mm	50 mm	10 μ m

Table 3.1 - Main characteristics of the laser sensor.

3.1.2 Acquisition device

The aim of the acquisition device is to convert the signal that arrives from the sensor from analogical to digital. The NI 9215 device was used in the tests performed. This is produced by National Instruments and it is shown in figure 3.2:



Figure 3.3 - Acquisition device NI 9215

3.1.3 Control system

The control system used is an application software implemented in a programming environment LabVIEW (Laboratory Virtual Instrument Engineering Workbench). The aim of the control system is to read and register the digital signal from the acquisition device and then to make it analysable.

LabVIEW is a powerful data acquisition and analysis programming language for PCs, produced by National Instruments. This is able to interface with NI 9215 acquisition device. LabVIEW is a graphical programming language in fact the interface does not consist of text strings, but rather of icons and links.

The interface has two work plans:

- Front panel;
- Block diagram.

The first allows to define and introduce all the input and output quantities, while the second is the actual executable program.

Two LabVIEW programs have been used:

- Long-Time Acquisition;
- Reading and Writing to a file.

Long-Time Acquisition was used to register the acquired signal from the acquisition device, to report it on a graph and to make it analysable.

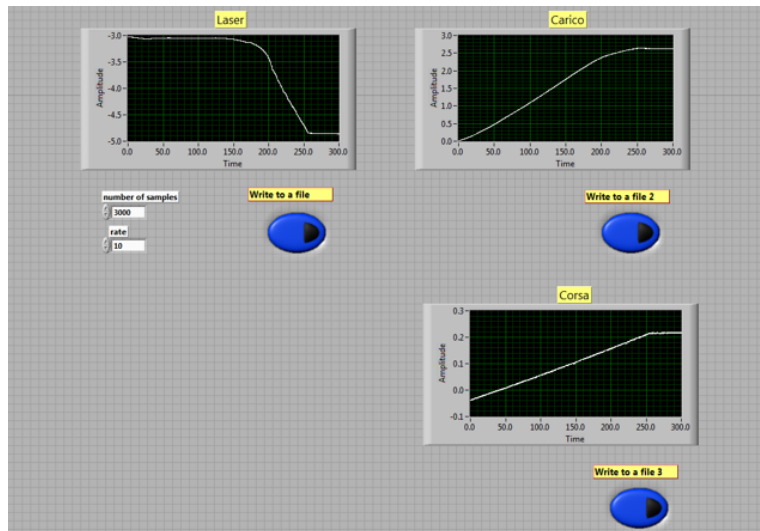


Figure 3.4 - Front panel of long-time acquisition program.

The input data were:

- Number of samples;
- Rate.

The bottom “write to a file” allows the signal to be saved or not.

The output data were:

- Laser (transversal displacement);
- Load;
- Axial displacement.

This three data output were reported on a time(s) - amplitude(V) graph.

Reading and Writing to a file reads the saved values by the acquisition program and creates a .txt file containing two column vectors whose elements are the acquisition time and signal voltage values.

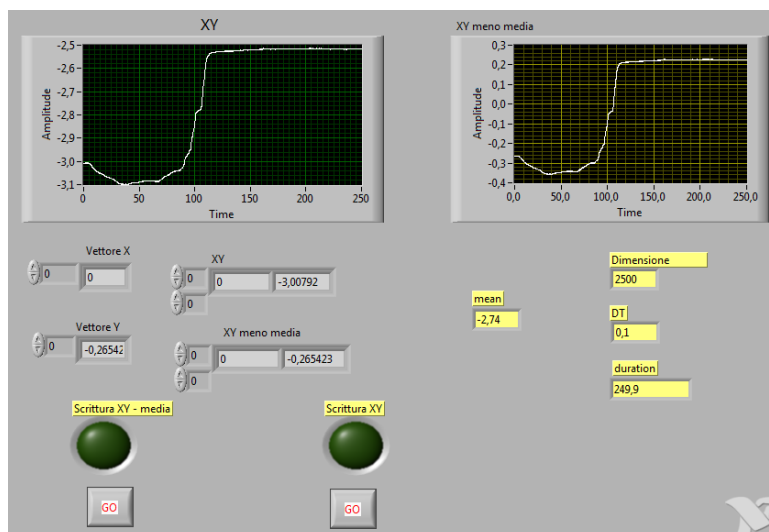


Figure 3.5 - Front panel of Reading and Writing to a file program.

3.2 Stability test

The experimental campaign was conducted using servo-hydraulic MTS testing machine, with a closed-loop electronic control and a maximum loading capacity of 100 kN. With this machine, stability tests for compression were carried out up to the post-critical branch and subsequent unloading.

Figure 3.5 shows the machine used.



Figure 3.6 - Servo-hydraulic MTS testing machine

The specimens were put in vertical position, constrained to the machine by connections which prevented displacements, rotations and twist of the end sections.

The results of this experimental campaign show the effect of intermediate warping stiffeners on the behaviour of thin-walled open profiles with cruciform (double I) cross-section.

Local stiffener connect the external flanges of the cross-section in such a way as to provide a four-cell box section.

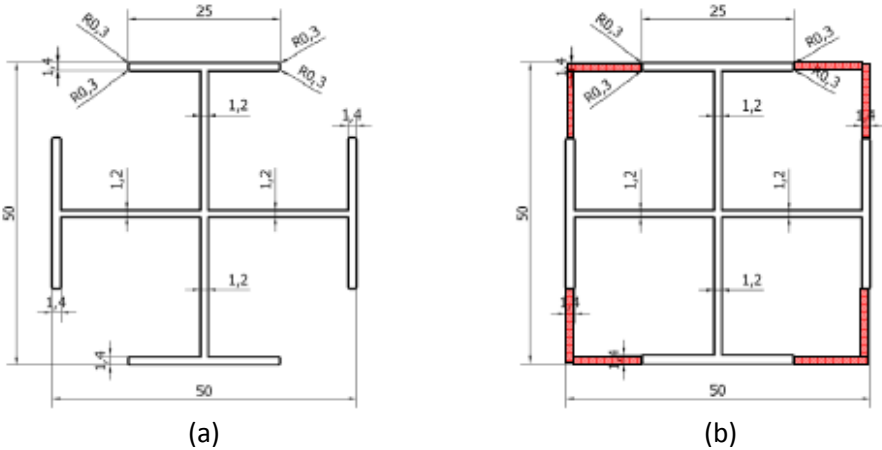


Figure 3.7 - (a) Actual and (b) stiffened cross-sections (dimensions in mm); red parts highlight the stiffening frame.

The shape of a double I implies high bending stiffness, modest torsion stiffness and non-negligible warping stiffness. Thus, such profiles are prone to buckling more in torsion than in bending.

3.2.1 Geometric and mechanical characteristic of the specimens

The beam is made of 6060-T5 aluminium alloy. The table 3.1 and the figure 3.7 describe the main geometrical and mechanical characteristics.

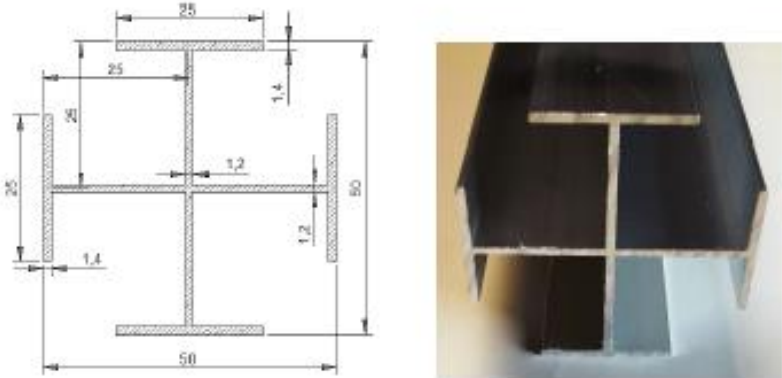


Figure 3.8 – (a) cruciform section; (b) photo of the section.

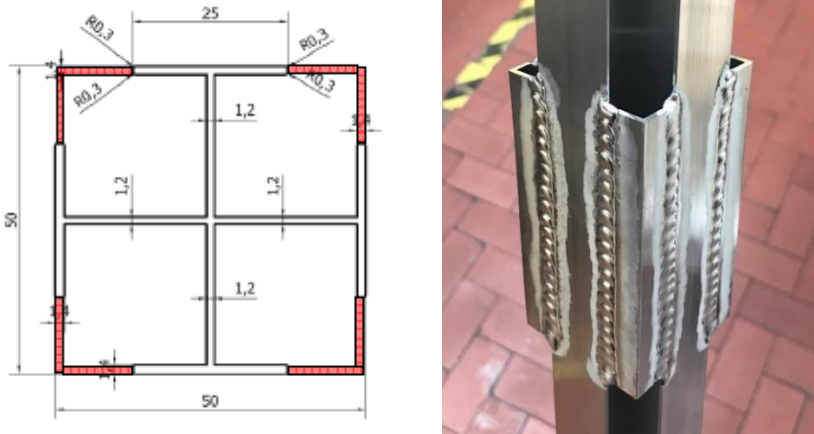


Figure 3.9 – (a) stiffened cross-sections; (b) photo of stiffener.

Table 3.1 - Geometric and mechanical characteristics

Section width	Section thickness		Length	Volumetric mass	Elastic module	Poisson coefficient
b (mm)	t1 (mm)	t2 (mm)	(mm)	ρ (kg/m ³)	E (N/mm ²)	(-)
50	1.2	1.4	950	2600	69000	0.3

Cross-section	A	$A_2=A_3$	$A_{23}=A_{32}$	J	I_c	$I_2=I_3$	$x_{c2}=x_{c3}$	$I_{f2}=I_{f3}$	Γ
	(mm ²)	(mm ²)	(mm ²)	(mm ⁴)	(mm ⁴)	(mm ⁴)	(mm)	(mm ⁵)	(mm ⁶)
Current	251.84	110.38	0	148.36	111'028	55'514	0	0	4'305'656
Stiffened	384.00	200.02	0	163'945	235'498	117'749	0	0	0
Diff., %	52	81	-	110'405	112	112	-	-	-100%

A, A_j , A_{ij} are the area, direct, and mixed shear shape modified areas, respectively; J is Saint-Venant's torsion factor; I_c is the polar moment of inertia with respect to the shear centre; I_j are the central principal moments of inertia; x_{cj} are the coordinates of the shear centre; I_{fj} are the flexural-torsion constant; and Γ is the warping constant. $A_{ij} = x_{cj} = I_{fj} = 0$.

The specimens were identified with the nomenclature shown in the table 3.2. The position of the stiffeners is measured from the base (right end in the figures of table 3.2).

Name specimen	Type of constraint	Stiffener position interval
 S1	Free warping	380-475 mm
 S2	Free warping	95-190 mm
 S3	Free warping	427.5-522.5 mm
 S4	Free warping	95-190 mm from each end
 S5	Free warping	0-95 mm
 S6	Free warping	0-95 from each end
 S7	Semi-restrained warping	427.5-522.5 mm
 S8	Semi-restrained warping	380-475 mm
 S9	Semi-restrained warping	95-190 mm
 S10	Semi-restrained warping	95-190 mm from each end
 S11	Semi-restrained warping	0-95 mm
 S12	Semi-restrained warping	0-95 from each end

Table 3.2 - Specimen nomenclature

3.2.2 Description of the stability test

The performed test was a direct compression conducted in axial displacement control. This static monotonic compression test was used to detect the buckling load.

The loading ramp was defined by imposing a hydraulic jack advancement speed equal to 0,01 mm/sec. Once the loading ramp was completed, the unloading ramp was started with a higher speed than the loading one.

The result of the test are curves:

- Axial load-Axial displacement;
- Axial load-Transverse displacement;

The buckling load is determined through these curves.

3.2.3 Constraint system

We used two constraint systems:

- semi-restrained warping;
- free warping.

The specimens were vertical, constrained to the machine by connections controlling displacement, rotations and twist of the section. Four brass elements were used as end connections.

Semi-restrained warping

For the semi-restrained warping, brass elements were used inside which the two ends of the beam were housed. In this condition, the whole section is inserted into the brass joint and both the web and the flanges are constrained.

In fact the warping is semi-restrained because the constraint does not react to traction, except for the small friction between the constraint and the specimen.

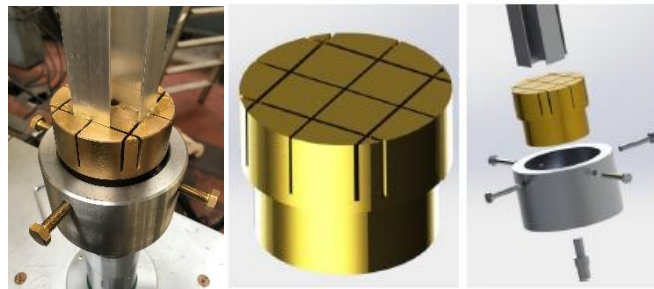


Figure 3.10 - Picture and rendering of lower end constraints

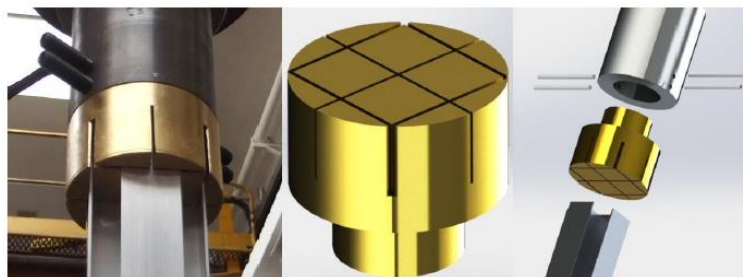


Figure 3.11 - Picture and rendering of upper end constraints

Free warping

Also for the free warping, brass elements were used in which the ends of the beam were housed.

These elements have a smaller diameter than the previous ones, so they leave the flanges outside. In fact just the web is constrained, while the flanges are left free to warp.



Figure 3.12 - Picture and rendering of lower end constraints

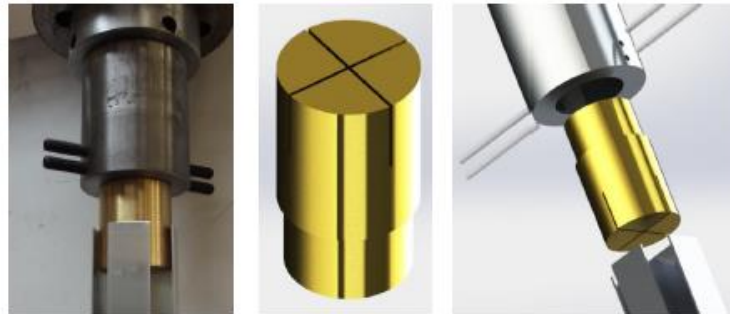


Figure 3.13 - Picture and rendering of upper end constraints

3.3 Results of the experimental campaign

Instability occurred by pure torsion of the specimen which twisted around its axis. This type of instability occurred in all the specimens. Moreover, the load curve shows that after the buckling load, it decreases and the torsional deformation enters its own plastic phase.

The axial load-axial displacement curves showed an initial setting, then a linear phase, and in the end a non-linear branch, reflecting the progressive degradation of the apparent beam stiffness. The load providing the end of the linear range can be assumed as a critical.

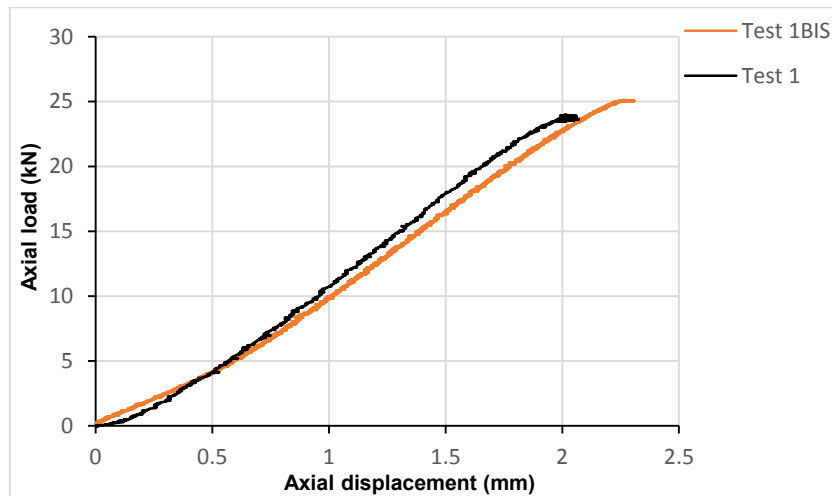
For some specimens it was possible to repeat the test because we had other virgin specimens.

Specimen S1

Specimen S1 and specimen S1 BIS have the stiffener positioned in the interval 380-475 mm, measured from the base and they are tested in the free warping constraint condition.

The graphs necessary to identify the buckling load are shown below:

- Axial load-Axial displacement

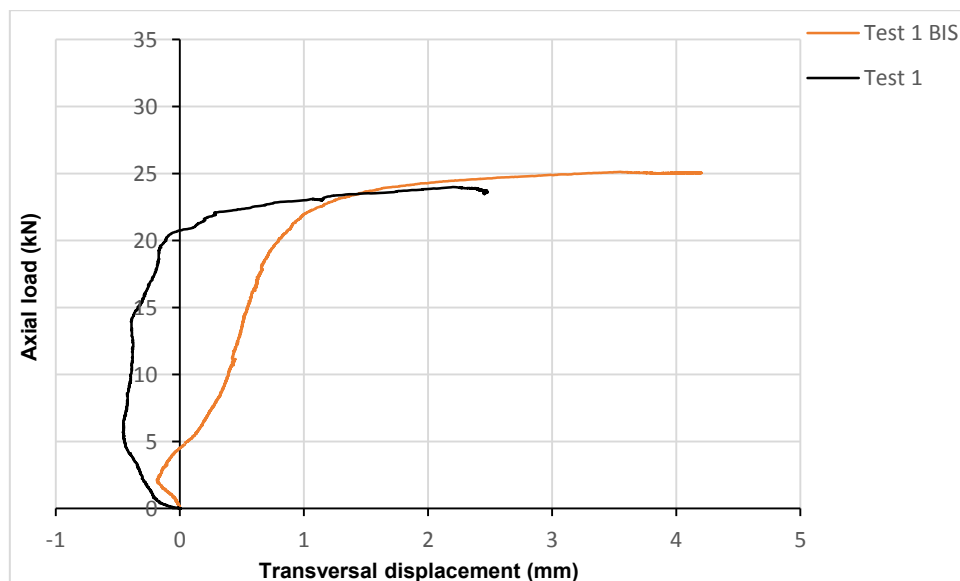


Graph 3.1 – Axial load-Axial displacement curve

Table 3.3 – Buckling load and associated displacement

	Buckling load	Displacement
Test 1	21 kN	1.84 mm
Test 1 BIS	21 kN	1.93 mm

- Axial load-Transverse displacement



Graph 3.2 – Axial load-Transverse displacement curve

The last two graphs confirm the value of the buckling load and the associated displacement identified through the axial load-axial displacement graph.

The curves show a post-critical behaviour of the unstable specimen.

Below there are some photos of the beam.

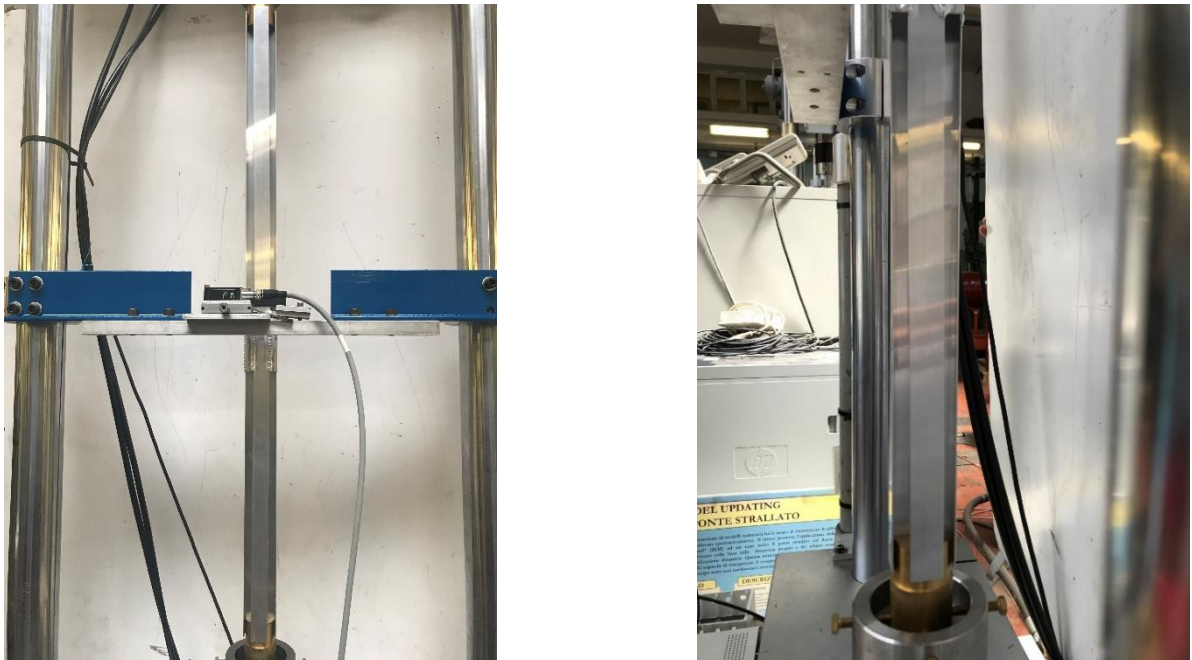


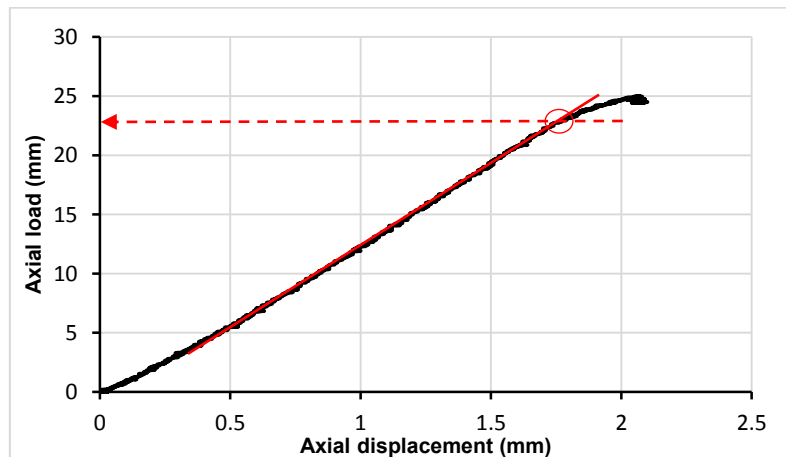
Figure 3.14 – Left: S1 specimen at the end of the test; Right: zoom on torsion instability

Specimen S2

Specimen S2 has the stiffener positioned in the interval 95-190 mm, measured from the base and it is tested in the free warping constraint condition.

The graphs necessary to identify the buckling load are shown below:

- Axial load-Axial displacement

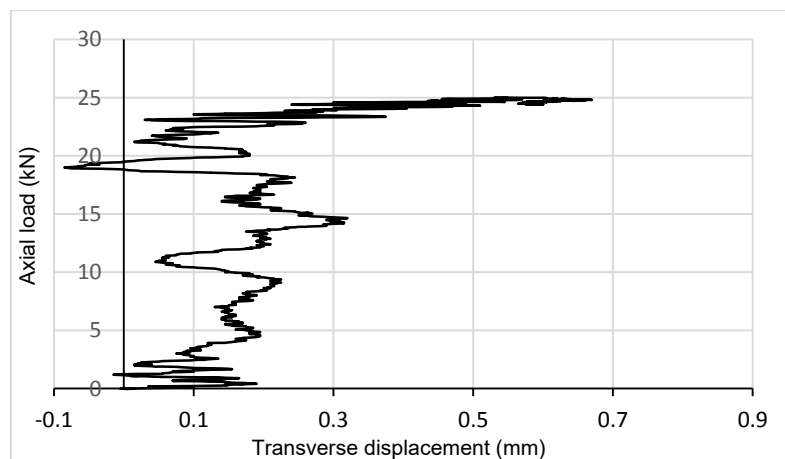


Graph 3.3 - Axial load-axial displacement curve

Table 3.4 – Buckling load and associated displacement

Buckling load	Displacement
23 kN	1.74 mm

- Axial load-Transverse displacement



Graph 3.4 – Axial load-Transverse displacement curve

The last two graphs confirm the value of the buckling load and the associated displacement identified through the axial load-axial displacement graph.

The curves show a post-critical behaviour of the unstable specimen.

Below are some photos of the beam.



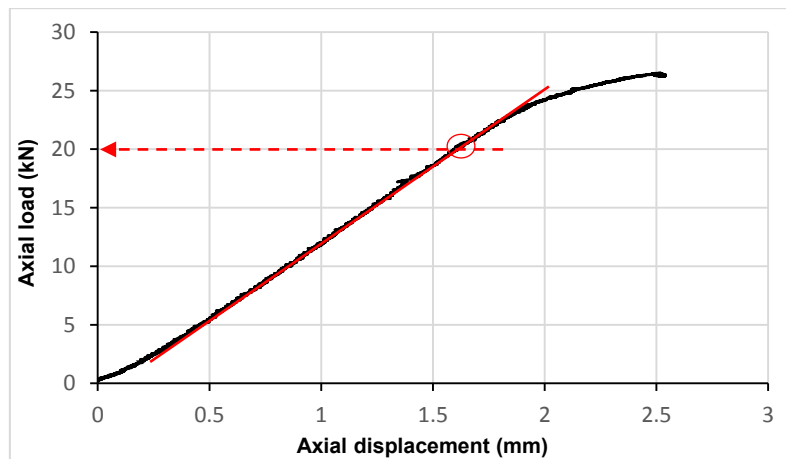
Figure 3.15 - S2 specimen at the end of the test.

Specimen S3

Specimen S3 has the stiffener positioned in the interval 427,5-522,5 mm, measured from the base and it is tested in the free warping constraint condition.

The graphs necessary to identify the buckling load are shown below:

- Axial load-Axial displacement

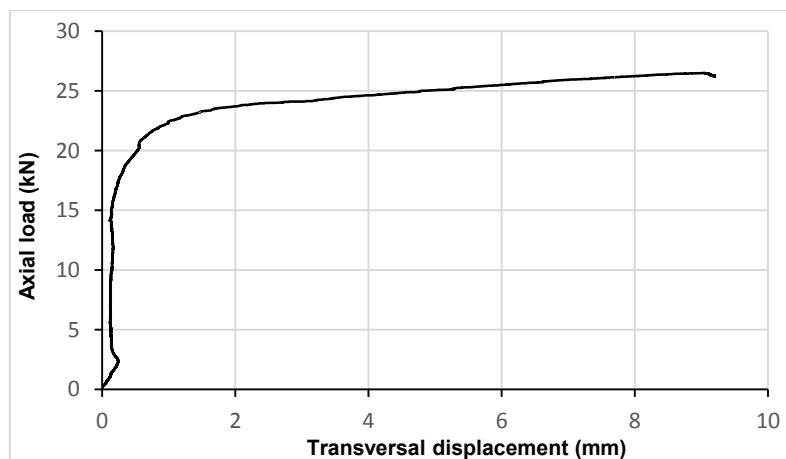


Graph 3.5 - Axial load-axial displacement curve

Table 3.5 – Buckling load and associated displacement

Buckling load	Displacement
20 kN	1.77 mm

- Axial load-Transverse displacement



Graph 3.6 – Axial load-Transverse displacement curve

The last two graphs confirm the value of the buckling load and the associated displacement identified through the axial load-axial displacement graph.

The curves show a post-critical behaviour of the unstable specimen.

Below are some photos of the beam.

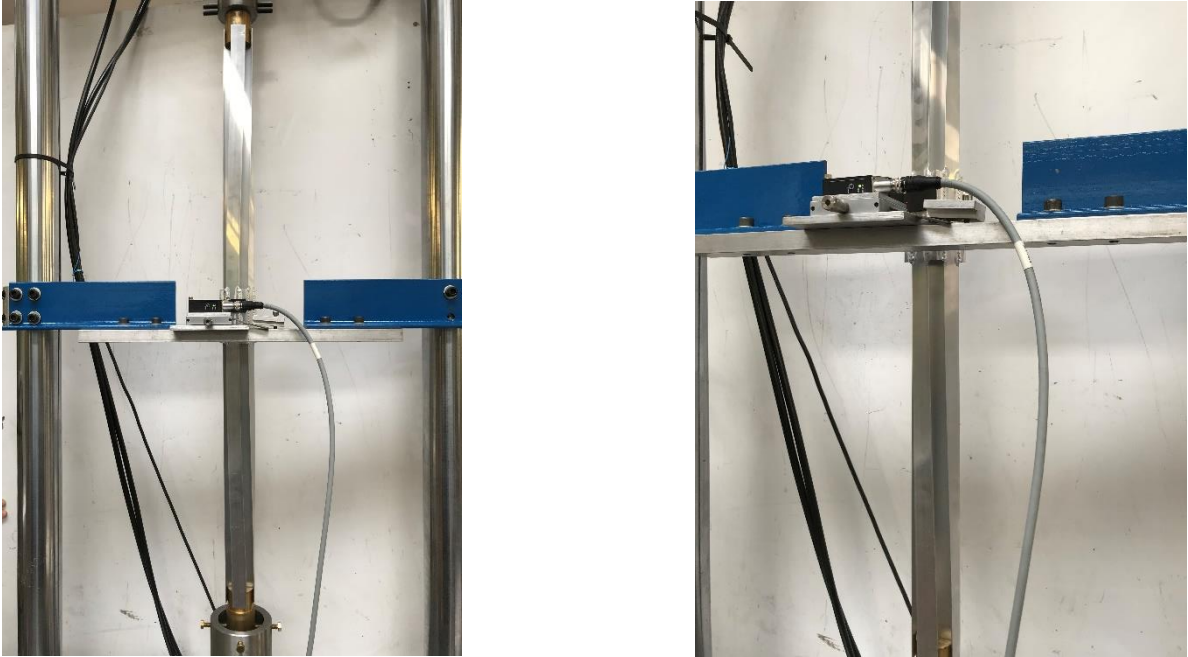


Figure 3.16 - Left: S1 specimen at the end of the test; Right: Zoom of torsional instability.

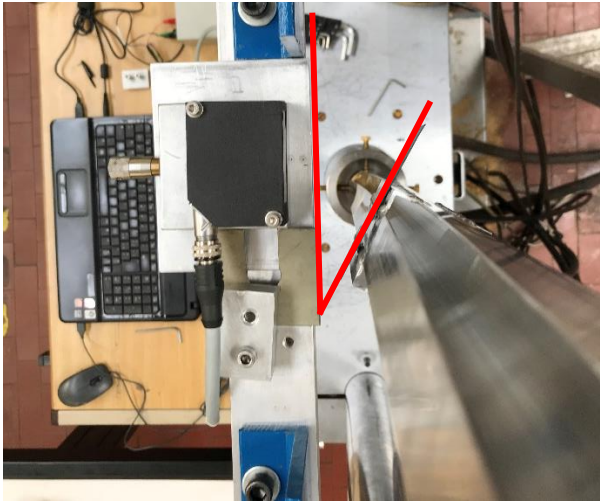


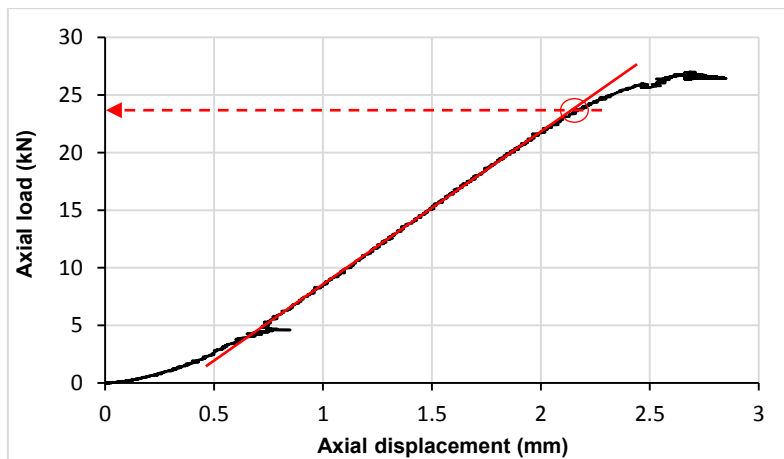
Figure 3.17 – Top view of torsion instability.

Specimen S4

Specimen S4 has the two stiffeners positioned in the interval 95-190 mm from each end. This specimen is tested in the free warping constraint condition.

The graphs necessary to identify the buckling load are shown below:

- Axial load-Axial displacement

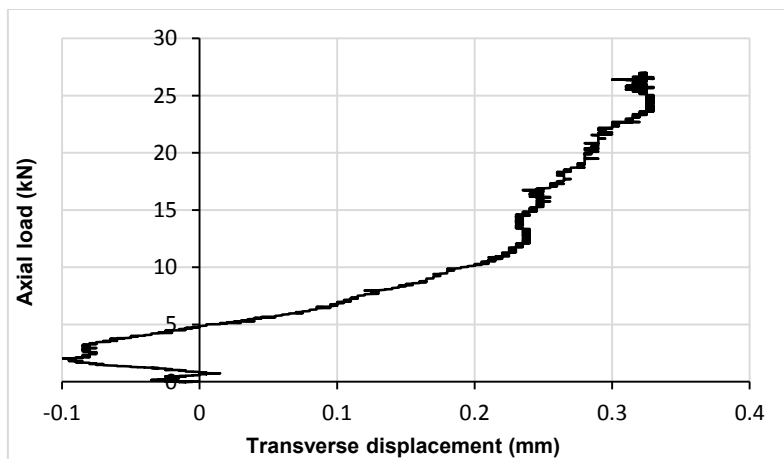


Graph 3.7 – Axial load-axial displacement curve

Table 3.6 – Buckling load and associated displacement

Buckling load	Displacement
24 kN	2.09 mm

- Axial load-Transverse displacement



Graph 3.8 – Axial load-Transverse displacement curve

The last two graphs confirm the value of the buckling load and the associated displacement identified through the axial load-axial displacement graph.

The curves show a post-critical behaviour of the unstable specimen.

From the axial load-transverse displacement curve it is noted how the stiffeners position stiffens a lot the beam.

Below are some photos of the beam.



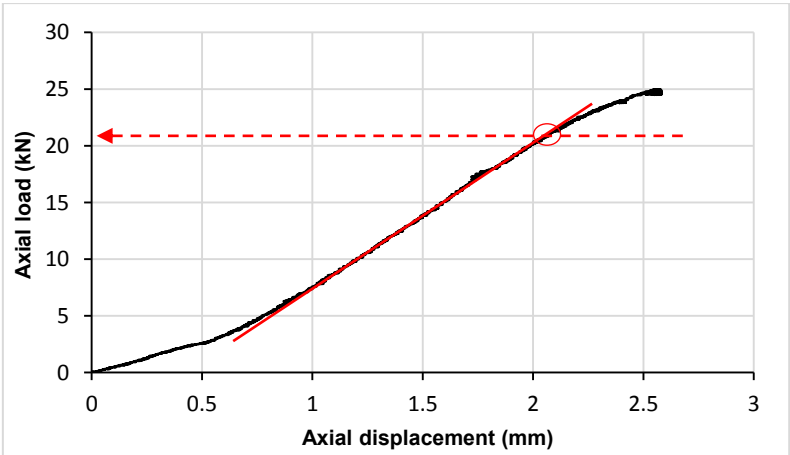
Figure 3.18 - S4 specimen at the end of the test.

Specimen S5

Specimen S5 has the stiffener positioned in the interval 0-95 mm, measured from the base and it is tested in the free warping constraint condition.

The graphs necessary to identify the buckling load are shown below:

- Axial load-Axial displacement

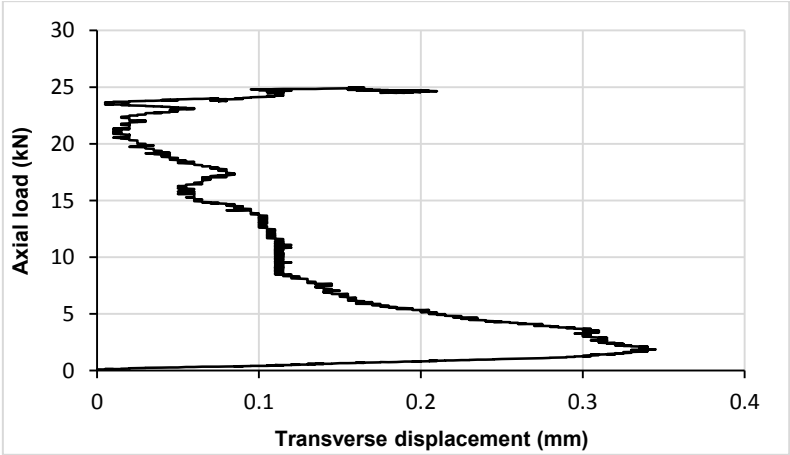


Graph 3.9 – Axial load-axial displacement curve

Table 3.7 – Buckling load and associated displacement

Buckling load	Displacement
21 kN	2.08 mm

- Axial load-Transverse displacement



Graph 3.10 – Axial load-Transverse displacement curve

The last two graphs confirm the value of the buckling load and the associated displacement identified through the axial load-axial displacement graph.

The curves show a post-critical behaviour of the unstable specimen.

Below are some photos of the beam.



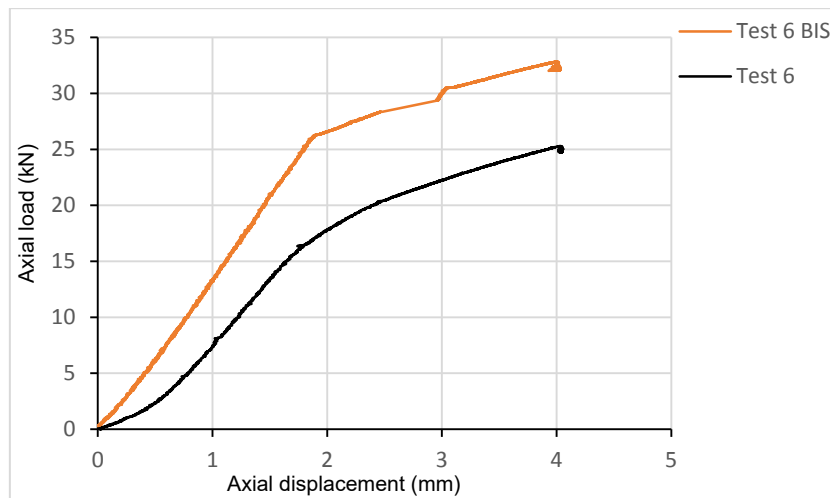
Figure 3.19 – Left: S5 specimen at the end of the test; Right: Zoom of torsion instability.

Specimen S6

Specimen S6 and specimen S6 BIS have the two stiffeners positioned in the interval 0-95 mm from each end. This specimens are tested in the free warping constraint condition.

The graphs necessary to identify the buckling load are shown below:

- Axial load-Axial displacement

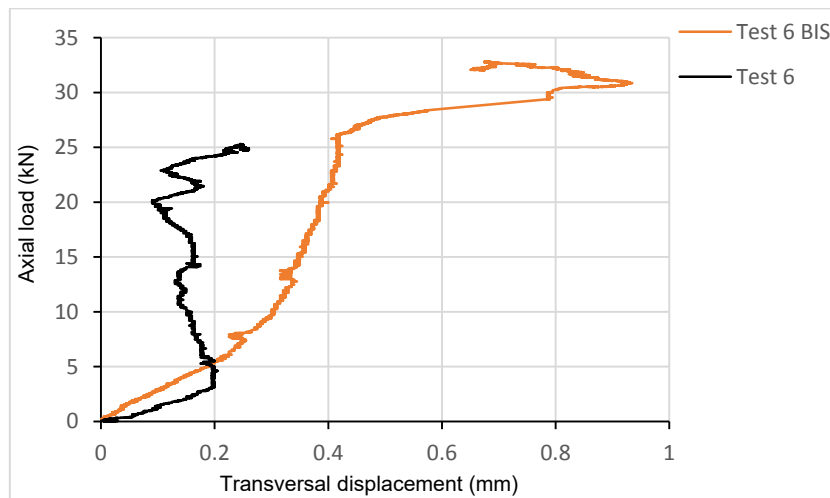


Graph 3.11 – Axial load-axial displacement curve

Table 3.8 – Buckling load and associated displacement

	Buckling load	Displacement
Test 6	16 kN	1.74 mm
Test 6 BIS	26 kN	1.89 mm

- Axial load-Transverse displacement



Graph 3.12 – Axial load-Transverse displacement curve

Note that the black curve and the orange curve have different trends and therefore provide different results.

Considering the S6 specimen, this has been tested without taking into account that the welding placed in contact with the constraints could alter the results. Subsequently, a virgin S6 specimen was tested, which was carefully filed in correspondence of the weld in such a way as to allow perfect contact between stiffeners and constraints.

The last two graphs confirm the value of the buckling load and the associated displacement identified through the axial load-axial displacement graph.

The curves show a post-critical behaviour of the unstable specimen.

Below is a photo of the beam.



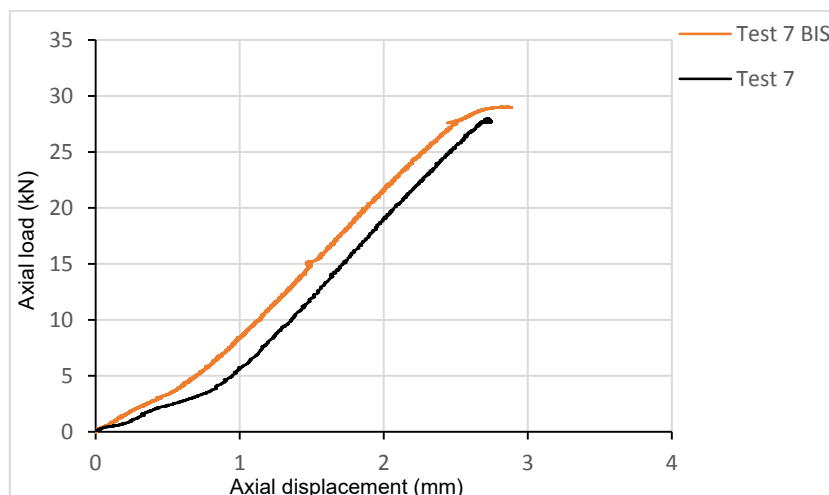
Figure 3.20 – S6 specimen at the end of the test.

Specimen S7

Specimen S7 and specimen S7 BIS have the stiffener positioned in the interval 427,5-522,5 mm, measured from the base and they are tested in the semi-restrained warping constraint condition.

The graphs necessary to identify the buckling load are shown below:

- Axial load-Axial displacement

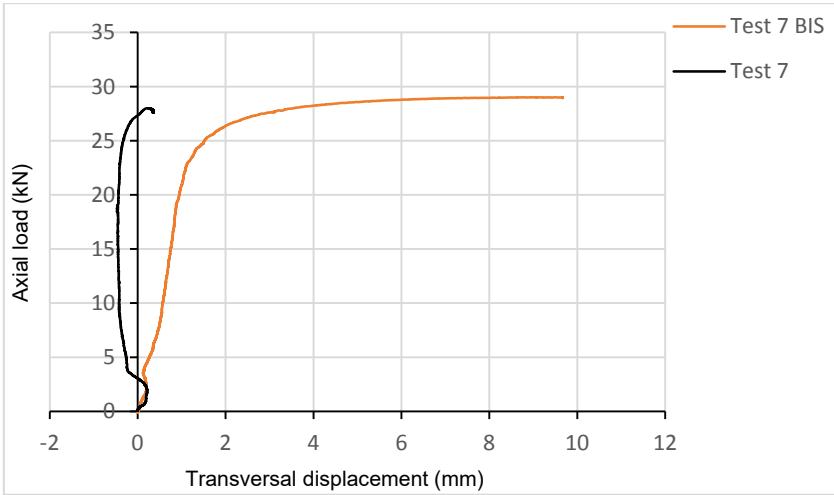


Graph 3.13 – Axial load-axial displacement curve

Table 3.9 – Buckling load and associated displacement

	Buckling load	Displacement
Test 7	27 kN	2.61 mm
Test 7 BIS	25 kN	2.27 mm

- Axial load-Transverse displacement



Graph 3.14 – Axial load-Transverse displacement curve

The last two graphs confirm the value of the buckling load and the associated displacement identified through the axial load-axial displacement graph.

The curves show a post-critical behaviour of the unstable specimen.

Below are some photos of the beam.

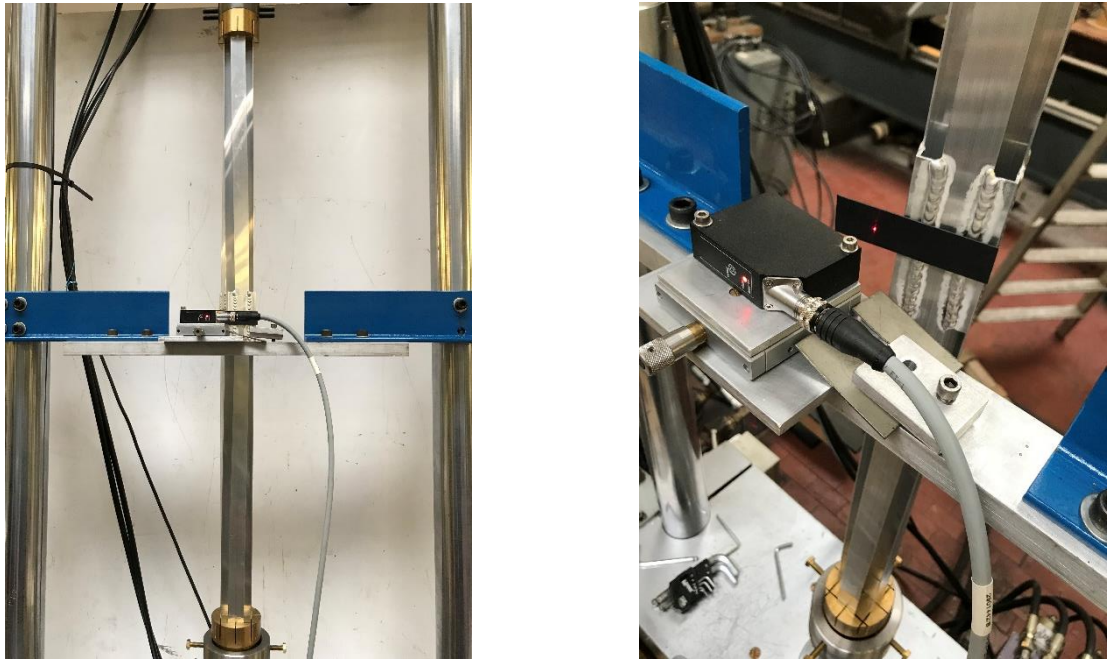


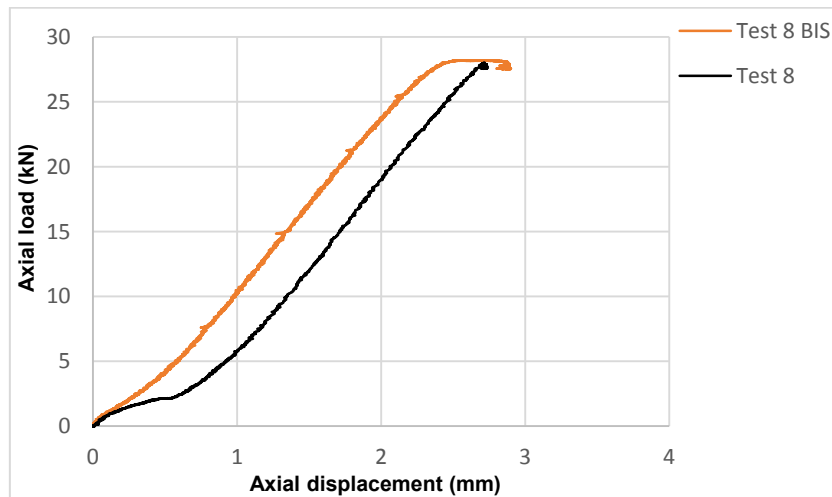
Figure 3.21 – Left: S7 specimen at the end of the test; Right: Zoom of torsional instability.

Specimen S8

Specimen S8 and specimen S8 BIS have the stiffener positioned in the interval 380-475 mm, measured from the base and they are tested in the semi-restrained warping constraint condition.

The graphs necessary to identify the buckling load are shown below:

- Axial load-Axial displacement

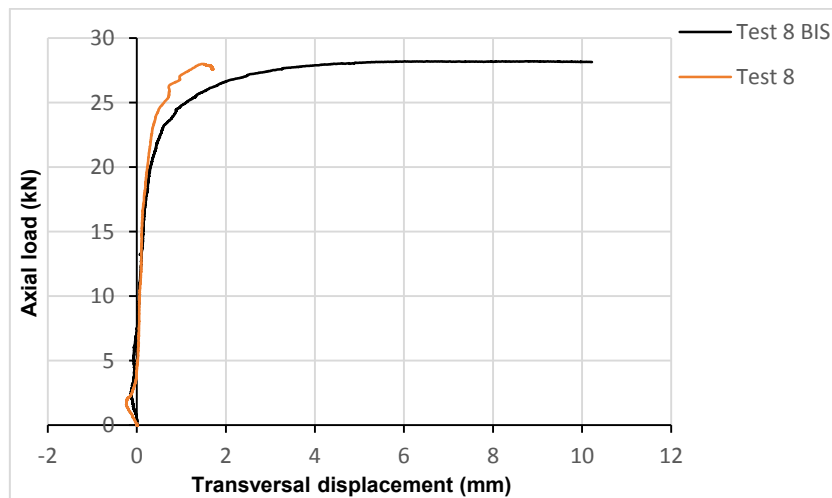


Graph 3.15 – Axial load-axial displacement curve

Table 3.10 – Buckling load and associated displacement

	Buckling load	Displacement
Test 8	27 kN	2.63 mm
Test 8 BIS	24 kN	2 mm

- Axial load-Transverse displacement



Graph 3.16 – Axial load-Transverse displacement curve

The last two graphs confirm the value of the buckling load and the associated displacement identified through the axial load-axial displacement graph.

The curves show a post-critical behaviour of the unstable specimen.

Below are some photos of the beam.

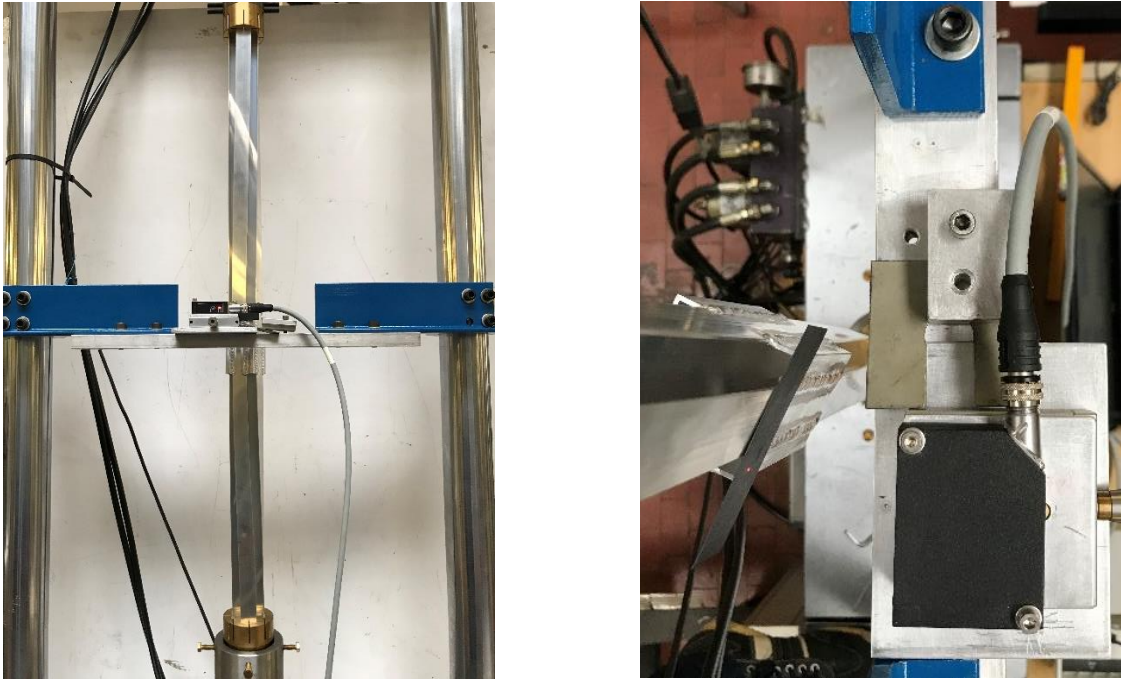


Figure 3.22 – Left: S8 specimen at the end of the test; Right: Top view of torsional instability.



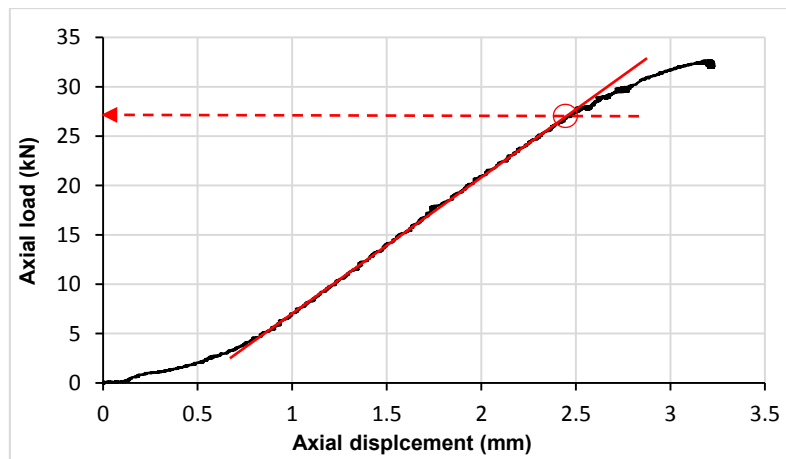
Figure 3.23 – Zoom of torsion instability.

Specimen S9

Specimen S9 has the stiffener positioned in the interval 95-190 mm, measured from the base and it is tested in the semi-restrained warping constraint condition.

The graphs necessary to identify the buckling load are shown below:

- Axial load-Axial displacement

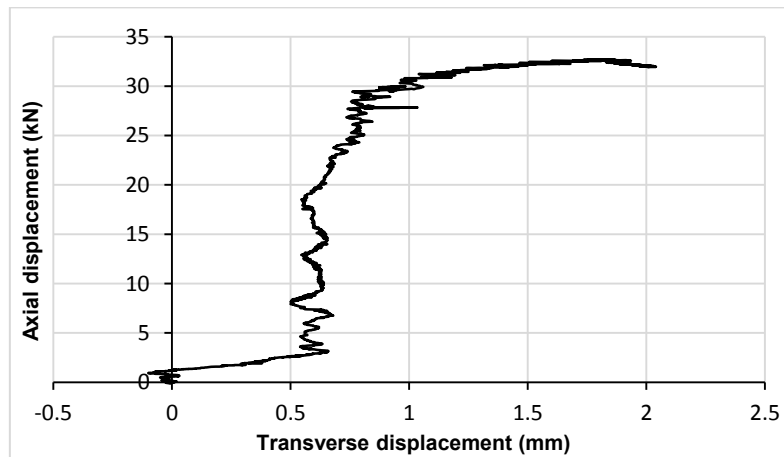


Graph 3.17 – Axial load-axial displacement curve

Table 3.11 – Buckling load and associated displacement

Buckling load	Displacement
27 kN	2.45 mm

- Axial load-Transverse displacement



Graph 3.18 – Axial load-Transverse displacement curve

The last two graphs confirm the value of the buckling load and the associated displacement identified through the axial load-axial displacement graph.

The curves show a post-critical behaviour of the unstable specimen.

Below are some photos of the beam.



Figure 3.24 – S9 specimen at the end of the test.

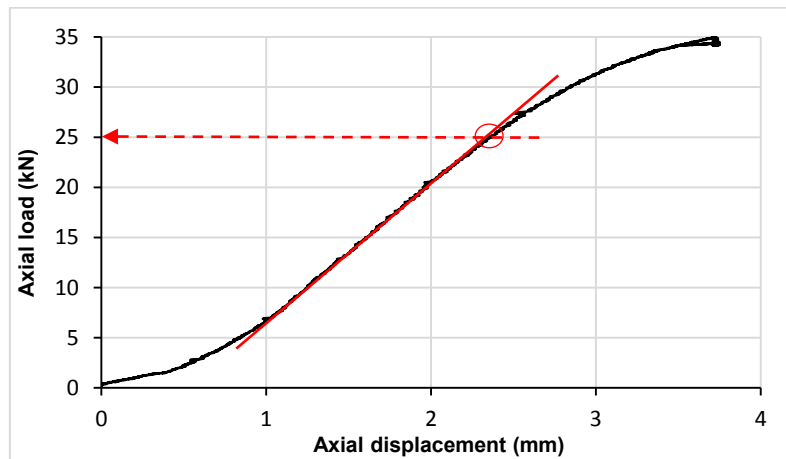


Figure 3.25 – Zoom of torsion instability.

Specimen S10

Specimen S10 has the two stiffeners positioned in the interval 95-190 mm from each end. This specimen is tested in in the semi-restrained warping constraint condition. The graphs necessary to identify the buckling load are shown below:

- Axial load-Axial displacement

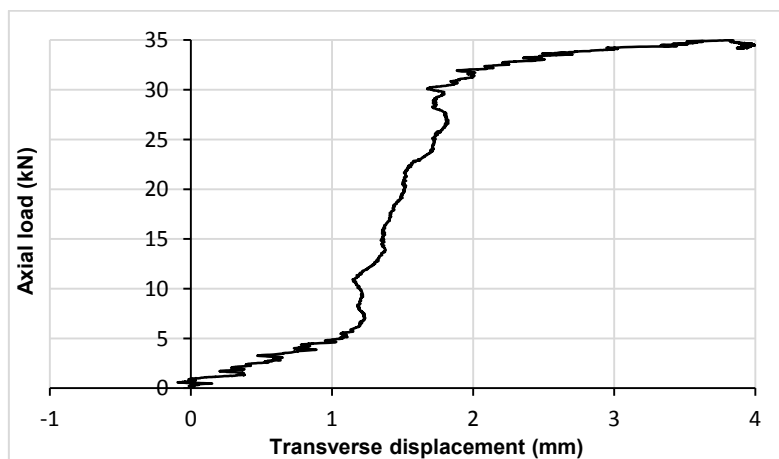


Graph 3.19 – Axial load-axial displacement curve

Table 3.12 – Buckling load and associated displacement

Buckling load	Displacement
25 kN	2.21 mm

- Axial load-Transverse displacement



Graph 3.20 – Axial load-Transverse displacement curve

The last two graphs confirm the value of the buckling load and the associated displacement identified through the axial load-axial displacement graph.

The curves show a post-critical behaviour of the unstable specimen.

Below are some photos of the beam.



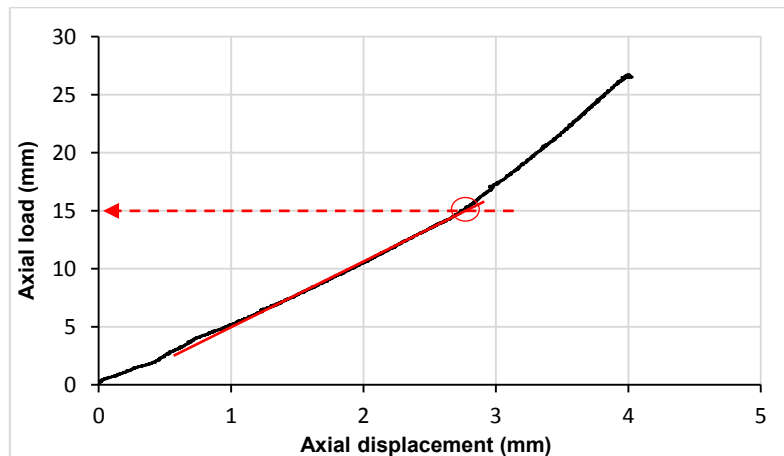
Figure 3.26 – S10 specimen at the end of the test.

Specimen S11

Specimen S11 has the stiffener positioned in the interval 0-95 mm, measured from the base and it is tested in the semi-restrained warping constraint condition.

The graphs necessary to identify the buckling load are shown below:

- Axial load-Axial displacement

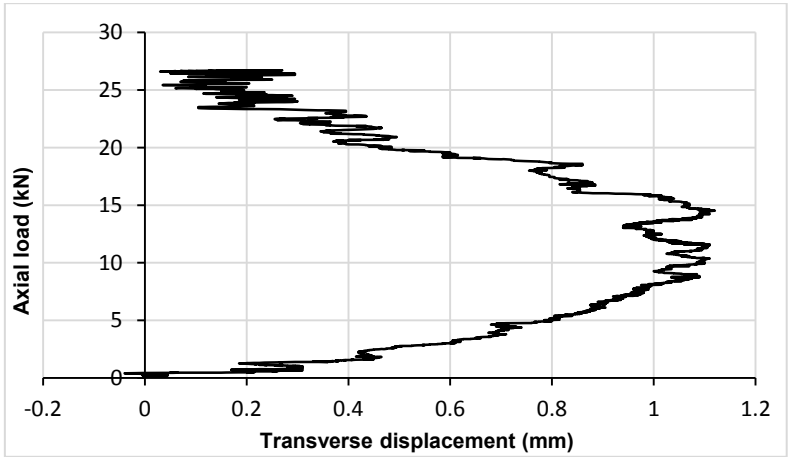


Graph 3.21 – Axial load-axial displacement curve

Table 3.12 – Buckling load and associated displacement

Buckling load	Displacement
15 kN	2.77 mm

- Axial load-Transverse displacement



Graph 3.22 – Axial load-Transverse displacement curve

The last two graphs confirm the value of the buckling load and the associated displacement identified through the axial load-axial displacement graph.

The curves show a post-critical behaviour of the unstable specimen.

The result of specimens S11 is not correct because the welding of the stiffener in contact with the constraint has distorted the test.

Below are some photos of the beam.



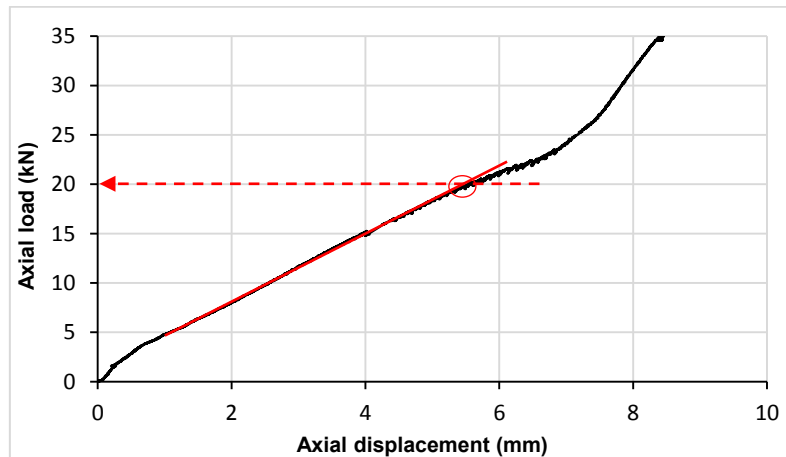
Figure 3.27 – S11 specimen at the end of the test.

Specimen S12

Specimen S12 has the two stiffeners positioned in the interval 0-95 mm from each end. This specimen is tested in in the semi-restrained warping constraint condition.

The graphs necessary to identify the buckling load are shown below:

- Axial load-Axial displacement

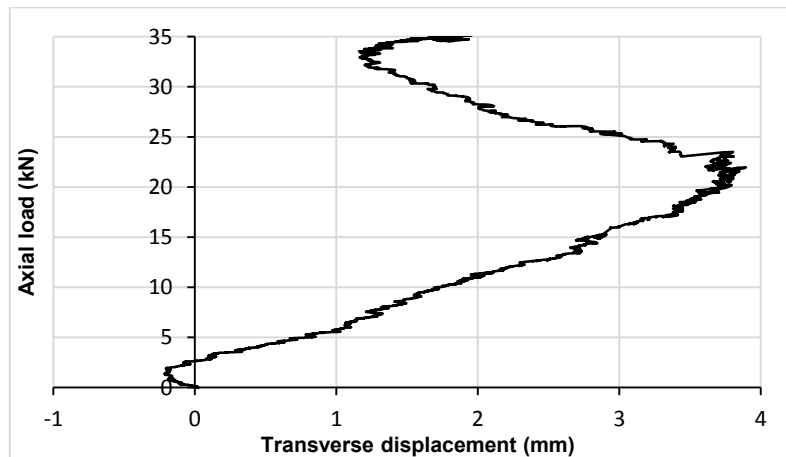


Graph 3.23 – Axial load-axial displacement curve

Table 3.13 – Buckling load and associated displacement

Buckling load	Displacement
20 kN	5.44 mm

- Axial load-Transverse displacement



Graph 3.24 – Transverse displacement-axial displacement curve

The last two graphs confirm the value of the buckling load and the associated displacement identified through the axial load-axial displacement graph.

The curves show a post-critical behaviour of the unstable specimen.

The result of specimens S12 is not correct because the welding of the stiffeners in contact with the constraints has distorted the test.

Below are some photos of the beam.



Figure 3.28 – Left : S12 specimen at the end of the test; Right: Zoom of torsion instability.

3.4 Comparison of experimental results

In the experimental campaign carried out, it was decided to use the laser to be able to extrapolate an extra curve in addition to the axial load-axial displacement in order to confirm the buckling load identified in the classic way.

All the specimens buckled by pure torsion as it is noted from the stability test.

Table 3.14 shows the comparisons between buckling loads in the various conditions investigated.

Table 3.14 – Comparison buckling loads

	Name specimen	Type of constraint	Stiffener position	Buckling load
	S1	Free warping	380-475 mm	21 kN
	S8	Semi-restrained warping	380-475 mm	24 kN
	S2	Free warping	95-190 mm	23 kN
	S9	Semi-restrained warping	95-190 mm	27 kN
	S3	Free warping	427.5-522.5 mm	20 kN
	S7	Semi-restrained warping	427.5-522.5 mm	25 kN
	S4	Free warping	95-190 mm from each end	24 kN
	S10	Semi-restrained warping	95-190 mm from each end	25 kN
	S5	Free warping	0-95 mm	21 kN
	S11	Semi-restrained warping	0-95 mm	15 kN
	S6	Free warping	0-95 from each end	26 kN
	S12	Semi-restrained warping	0-95 from each end	20 kN

From table 3.14 we can observe as the buckling load is conditioned by the type of constraint but above all by the position of the stiffener or the stiffeners.

Chapter 4

Numerical simulations and comparisons

The numerical simulations were developed using the LUSAS finite element calculation code. Numerical models were constructed which were able to reproduce the results obtained experimentally.

In the LUSAS environment the beam was modelled through thin shell elements. Figure 4.1 shows an example of a constructed numerical model.

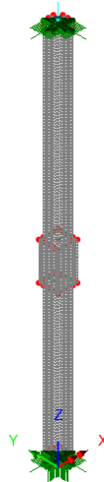


Figure 4.1 - Example of a constructed numerical model

The thin shell element used was the QSL8

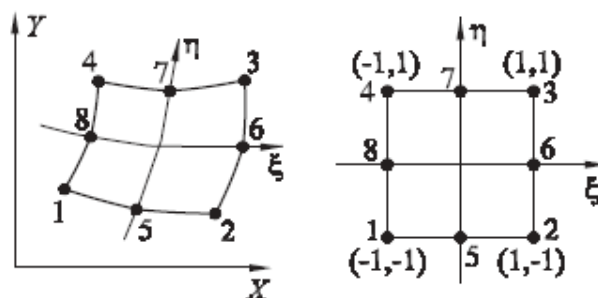


Figure 4.2 Finite element QSL8 (real), finite element QSL8 (parent)

Each numerical model has stiffener or stiffeners in different positions, so different meshes were created.

The beams tested are in aluminium alloy 6060 T5, so the material is isotropic and elastic-linear with the following properties:

- Elastic module $E = 69000 \text{ N/mm}^2$;
- Poisson coefficient $\nu = 0.3$.

The length of the beam is 950 mm while the stiffeners are 95 mm long. Moreover the geometry of the section has been created considering the average line.

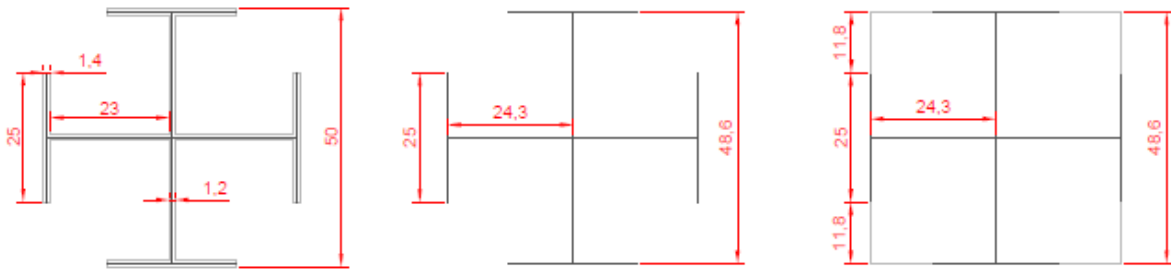


Figure 4.3 – Beam section

LUSAS was used to obtain the buckling loads, in particular for the analysis of critical loads of the first 3 mode (eigenvalue problem). The Buckling Analysis was carried out to do this.

The analyses were conducted for the following cases:

- Warping free at both ends (free warping condition);
- Warping restrained at both ends (restrained warping condition);
- Warping free at one end and restrained at the other (mixed warping condition).

4.1 Free warping

You can see the models with the constraint condition of free warping below. This condition was simulated by setting structural supports.

For the upper constraint in figure 4.2, the screenshot of the settings introduced in the calculation program is shown, so that the constraint condition is free warping. It is necessary to prevent the translation in x and y while in z the translation is free, and also to fix the rotations about x, y and z.

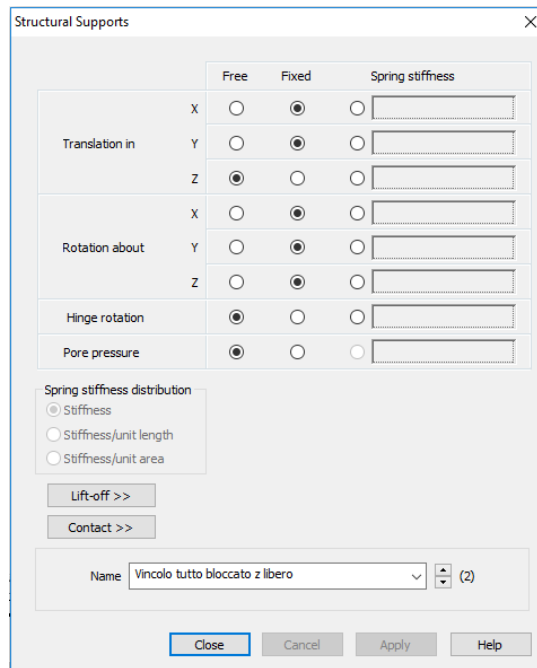


Figure 4.4 – Screenshot upper constraint

For the lower constraint in figure 4.3, the screenshot of the settings introduced in the calculation program is shown, so that the constraint condition is free warping. It is necessary to block translation and rotation in x, y and z.

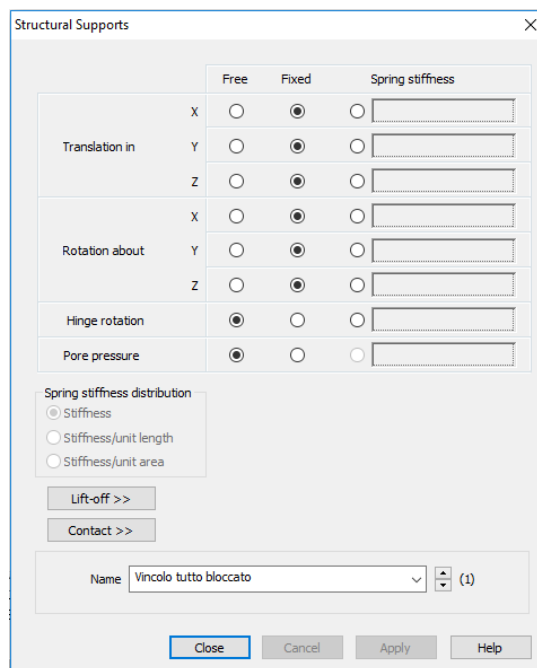


Figure 4.5 – Screenshot lower constraint

Figure 4.4 shows the image of the two constraints and the concentrated load of 1 kN.

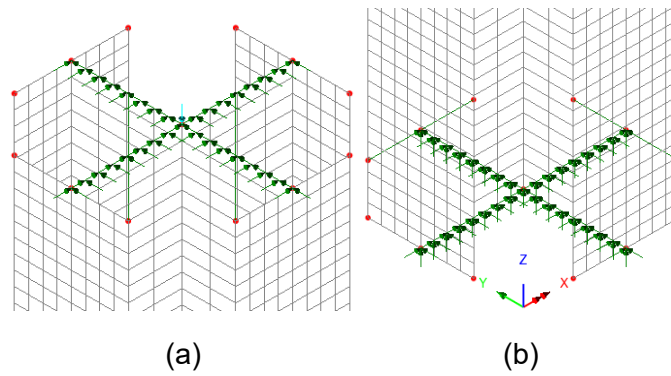


Figure 4.6 – (a) Upper constraint; (b) Lower constraints.

Model M1

Model M1 has the stiffener positioned in the interval 380-475 mm, measured from the base and it is analysed in the free warping condition.

Table 4.1 shows the results obtained from the buckling analysis of the structure for the first 3 modes.

Mode	N_{cr}	Error
1	18.79 kN	0.35E-06
2	73.56 kN	0.72E-06
3	79.78 kN	0.84E-05

Table 4.1 – Buckling loads of the first 3 mode.

The undeformed and deformed models of the first mode are shown below:

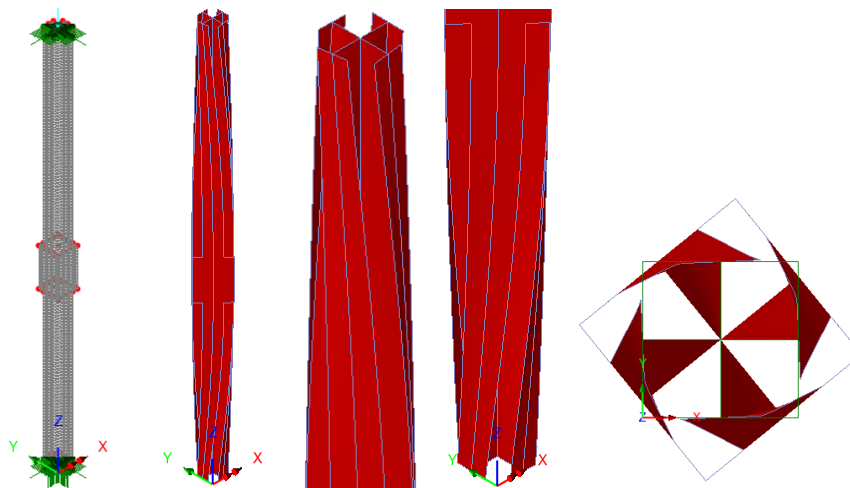


Figure 4.7 - From the left: undeformed, deformed, upper extremity, lower extremity and top view of the deformed.

It is possible to notice that the instability of mode 1 is of the torsional type, as already observed in the experimental campaign. Even that of mode 2 is of the torsional type while the instability of mode 3 is of the flexural type.

Focusing on the ends of the beam, the effect of the type of constraint is visible. As this is a case of free warping, the ends are deformed.

The longitudinal displacement values (DZ) shown in figure 4.8 are defined but for an arbitrary constant (eigenvalue problem). Their contour plot show as stiffeners prevent warping.

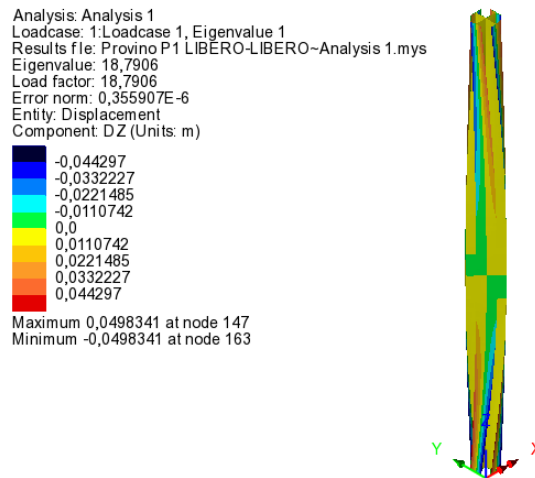


Figure 4.8 – Displacement DZ.

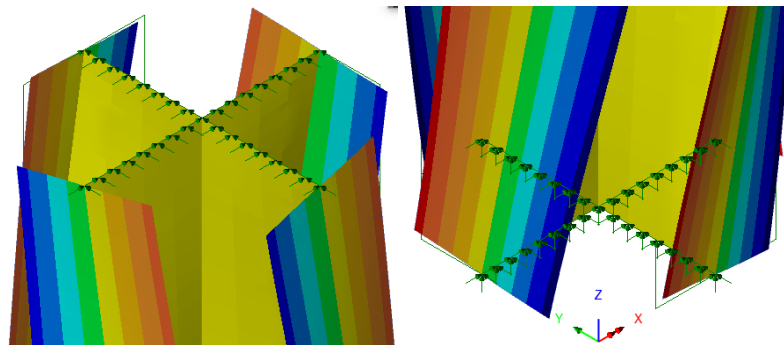


Figure 4.9 – Warping in the end sections.

Model M2

Model M2 has the stiffener positioned in the interval 95-190 mm, measured from the base and it is analysed in the free warping condition.

Table 4.2 shows the results obtained from the buckling analysis of the structure for the first 3 modes.

Mode	N_{cr}	Error
1	33.90 kN	0.46E-07
2	77.33 kN	0.33E-07
3	78.50 kN	0.11E-06

Table 4.2 – Buckling loads of the first 3 mode.

The undeformed and deformed models of the first mode are shown below:

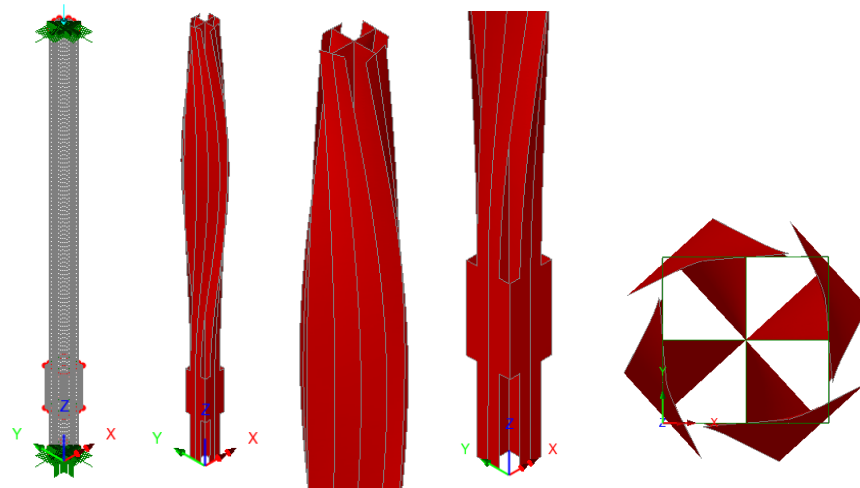


Figure 4.10 - From the left: undeformed, deformed, upper extremity, lower extremity and top view of the deformed.

It is possible to notice that the instability of mode 1 is of the torsional type, as already observed in the experimental campaign. Even that of mode 2 is of the torsional type while the instability of mode 3 is of the flexural type.

Focusing on the ends of the beam, the effect of the type of constraint is visible. In this case, the top end section warps, while warping is prevented near and below the stiffened zone (figure 4.11). Note that warping vanishes also between the stiffeners and the top end.

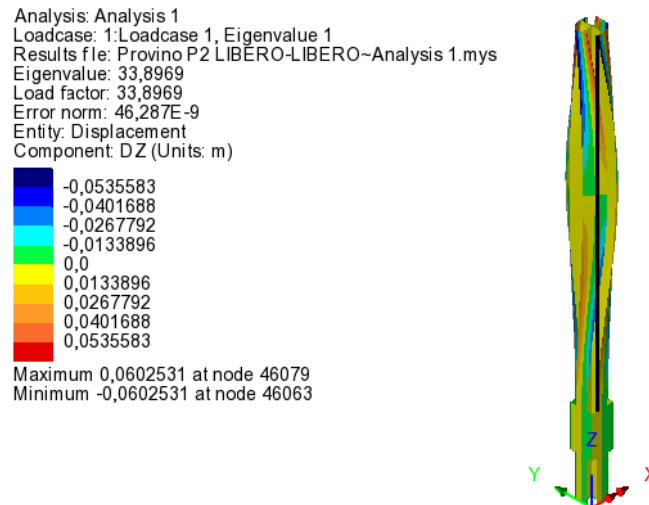


Figure 4.11 – Displacement DZ.

Model M3

Model M3 has the stiffener positioned in the interval 427,5-522,5 mm, measured from the base and it is analysed in the free warping condition.

Table 4.3 shows the results obtained from the buckling analysis of the structure for the first 3 modes.

Mode	N_{cr}	Error
1	18.34 kN	0.34E-07
2	81.07 kN	0.41E-07
3	81.07 kN	0.13E-07

Table 4.3 – Buckling loads of the first 3 mode.

The undeformed and deformed models of the first mode are shown below:

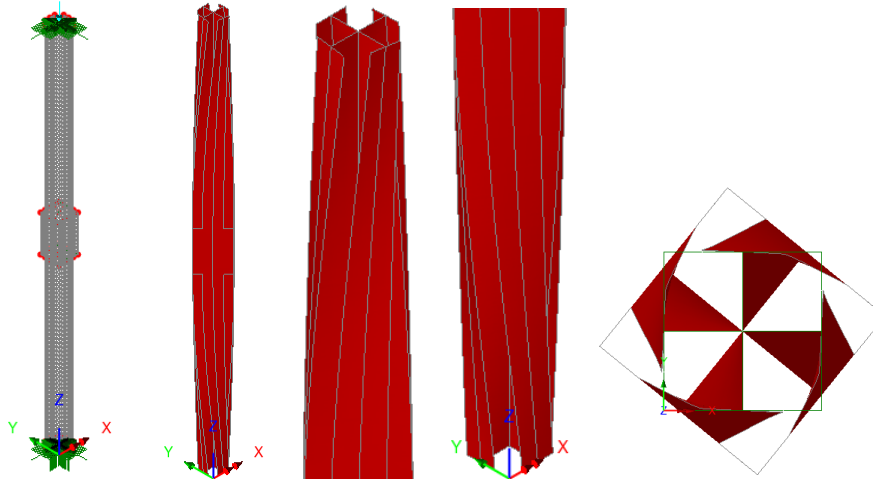


Figure 4.12 - From the left: undeformed, deformed, upper extremity, lower extremity and top view of the deformed.

It is possible to notice that the instability of mode 1 is of the torsional type, as already observed in the experimental campaign, while the ones of mode 2 and of mode 3 is of a flexural type.

Focusing on the ends of the beam, the effect of the type of constraint is visible. As this is a case of free warping, the ends are deformed. Warping tends to vanish moving from the ends toward the stiffened zone, where it is null (figure 4.13).

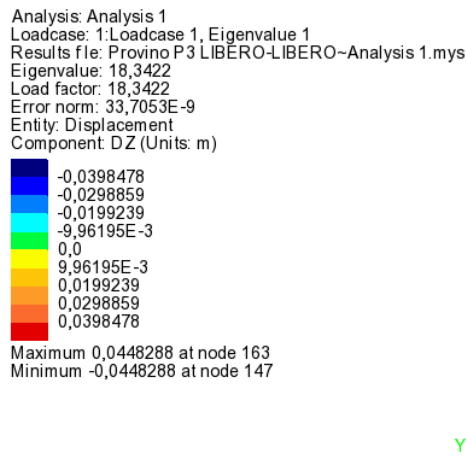


Figure 4.13 – Displacement DZ.

Model M4

Model M4 has the two stiffeners positioned in the interval 95-190 mm from each end. This model is analysed in the free warping condition.

Table 4.4 shows the results obtained from the buckling analysis of the structure for the first 3 modes.

Mode	N_{cr}	Error
1	81.15 kN	0.16E-09
2	81.15 kN	0.17E-09
3	84.26 kN	0.53E-09

Table 4.4 – Buckling loads of the first 3 mode.

The undeformed and deformed models of the first mode are shown below:

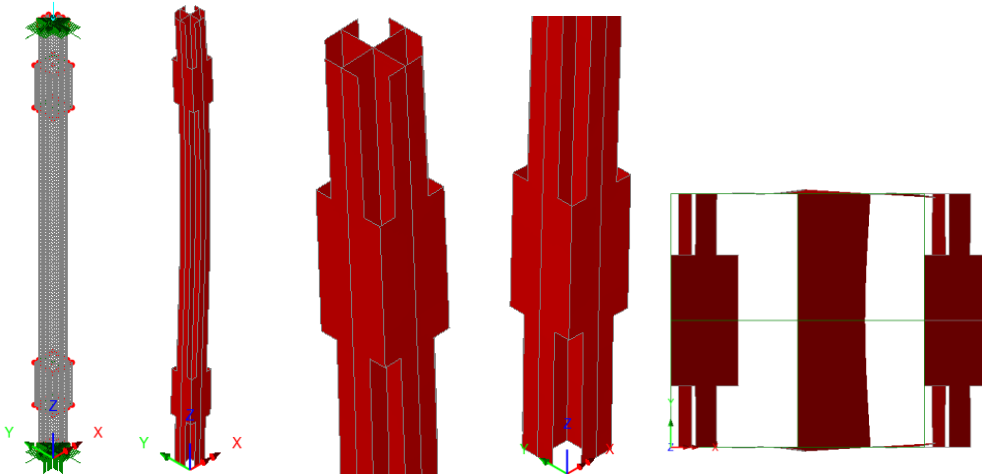


Figure 4.14 - From the left: undeformed, deformed, upper extremity, lower extremity and top view of the deformed.

It is possible to notice that the instability of mode 1 is of the bending type, as already observed in the experimental campaign; also that of mode 2 is of the bending type while the instability of mode 3 is of the torsional type.

The values of DZ and their contour plot in figure 4.15 show that all sections do not warp, i.e. remain plane (bending).

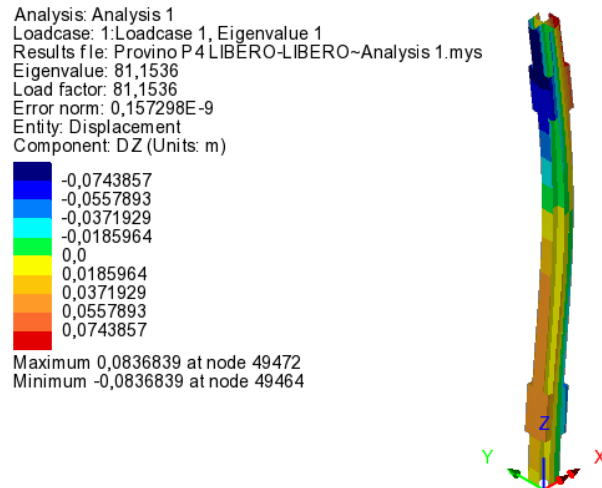


Figure 4.15 – Displacement DZ.

Model M5

Model M5 has the stiffener positioned in the interval 0-95 mm, measured from the base and it is analysed in the free warping condition.

Table 4.5 shows the results obtained from the buckling analysis of the structure for the first 3 modes.

Mode	N_{cr}	Error
1	28.67 kN	0.36E-07
2	63.64 kN	0.71E-07
3	79.75 kN	0.26E-05

Table 4.5 – Buckling loads of the first 3 mode.

The undeformed and deformed models of the first mode are shown below:

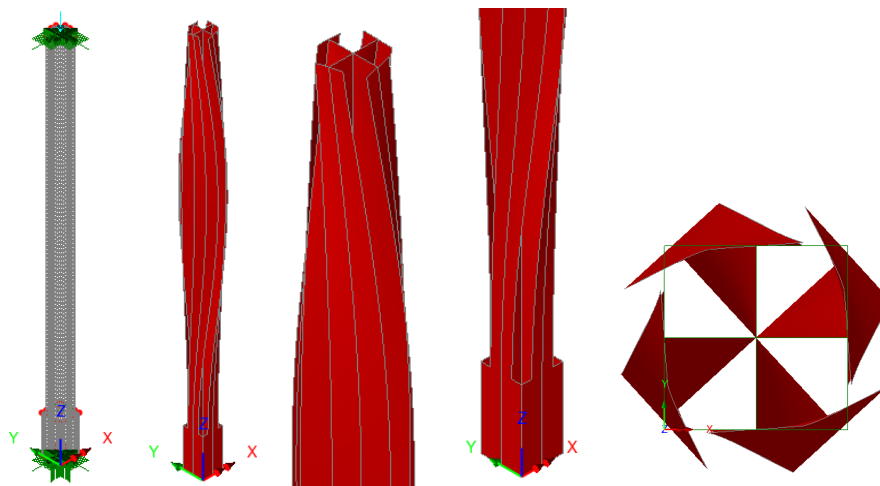


Figure 4.16 - From the left: undeformed, deformed, upper extremity, lower extremity and top view of the deformed.

It is possible to notice that the instability of mode 1 is of the torsional type, as already observed in the experimental campaign. Even that of mode 2 is of the torsional type while the instability of mode 3 is of the flexural type.

Figure 4.17 shows that the behaviour is similar to that of Model M2.

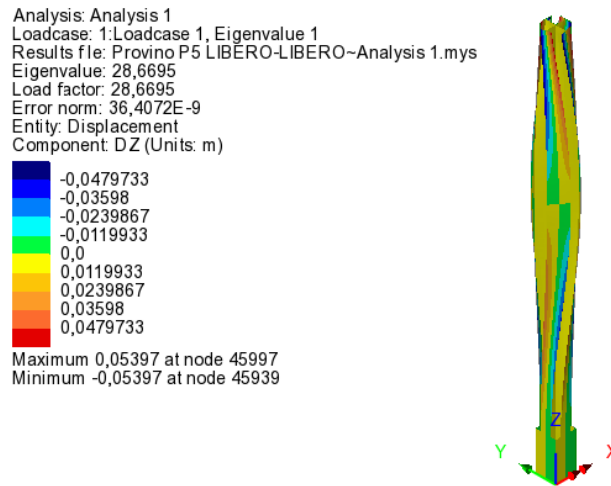


Figure 4.17 – Displacement DZ.

Model M6

Model M6 has the two stiffeners positioned in the interval 0-95 mm from each end. This model is analysed in the free warping condition.

Table 4.6 shows the results obtained from the buckling analysis of the structure for the first 3 modes.

Mode	N_{cr}	Error
1	52.35 kN	0.21E-06
2	80.63 kN	0.14E-05
3	80.63 kN	0.52E-07

Table 4.6 – Buckling loads of the first 3 mode.

The undeformed and deformed models of the first mode are shown below:

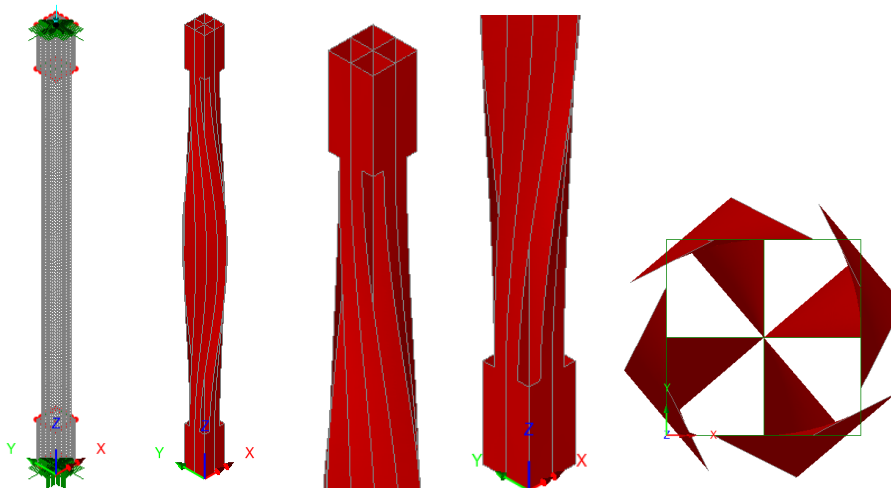


Figure 4.18 - From the left: undeformed, deformed, upper extremity, lower extremity and top view of the deformed.

It is possible to notice that the instability of mode 1 is of the torsional type, as already observed in the experimental campaign, while the ones of mode 2 and of mode 3 is of a flexural type.

Figure 4.19 shows how warping vanishes at the ends, because of the stiffeners, and at mid-length, because of the symmetry.

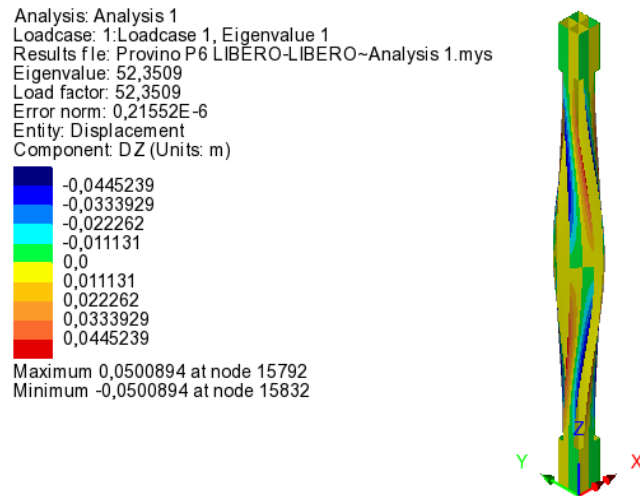


Figure 4.19 – Displacement DZ.

4.2 Fully-restrained warping

Now you can see the models analysed in condition of fully-restrained warping. This was simulated by setting structural supports.

The fully-restrained warping condition was simulated by introducing a 1 mm layer of high stiffness material ($E = 10^{15}$ Pa) on the upper end while on the lower end, some structural supports were simply placed. Then this layer of high-stiffness material was constrained and loaded in the same way as in the free warping condition.

Figure 4.20 shows the image of the two constraints and the concentrated load of 1 kN.

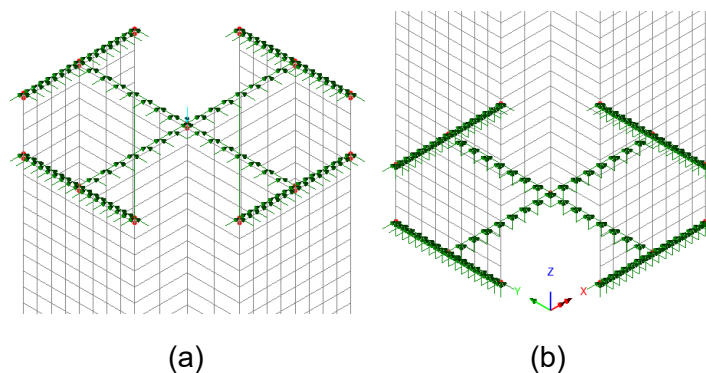


Figure 4.20 – (a) Upper constraint; (b) Lower constraints.

Model M7

Model M7 has the stiffener positioned in the interval 427,5-522,5 mm, measured from the base and it is analysed in fully-restrained warping condition.

Table 4.7 shows the results obtained from the buckling analysis of the structure for the first 3 modes.

Mode	N_{cr}	Error
------	----------	-------

1	43.34 kN	0.28E-04
2	120.72 kN	0.14E-06
3	120.72 kN	0.37E-07

Table 4.7 – Buckling loads of the first 3 mode.

The undeformed and deformed models of the first mode are shown below:

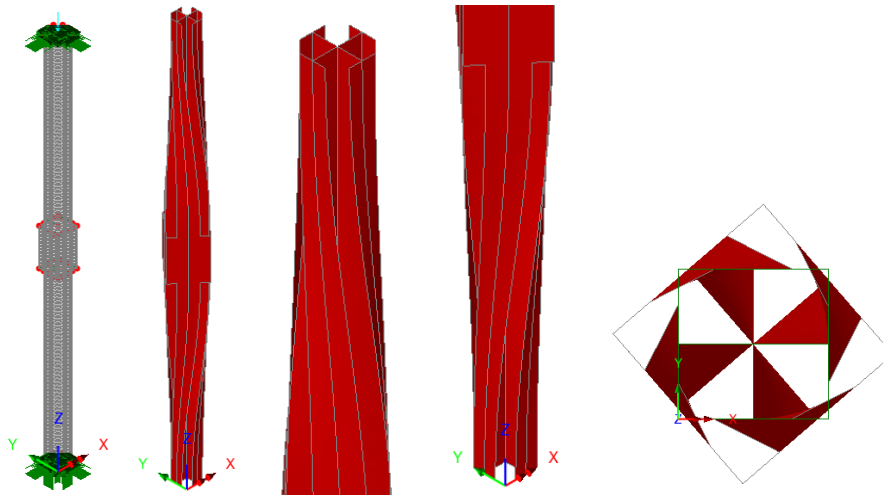


Figure 4.21 - From the left: undeformed, deformed, upper extremity, lower extremity and top view of the deformed.

It is possible to notice that the instability of mode 1 is of the torsional type, as already observed in the experimental campaign, while the ones of mode 2 and of mode 3 is of a flexural type.

Focusing on the ends of the beam, the effect of the type of constraint is visible. As this is a case of restrained warping, the ends are not deformed.

Contour plot and values in figure 4.22 show that warping is null at the ends and around the stiffened zone. A detail near the end sections is shown in figure 4.23.

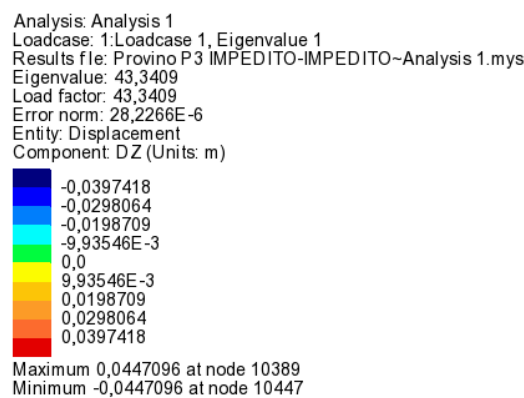


Figure 4.22 – Displacement DZ.

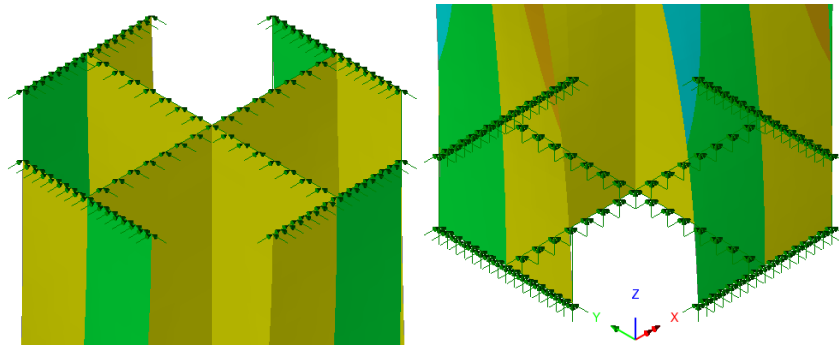


Figure 4.23 – Displacements DZ near the end sections (warping is null).

Model M8

Model M8 has the stiffener positioned in the interval 380-475 mm, measured from the base and it is analysed in the fully-restrained warping condition.

Table 4.8 shows the results obtained from the buckling analysis of the structure for the first 3 modes.

Mode	N_{cr}	Error
1	45.41 kN	0.22E-06
2	118.42 kN	0.37E-06
3	118.44 kN	0.28E-07

Table 4.8 – Buckling loads of the first 3 mode.

The undeformed and deformed models of the first mode are shown below:

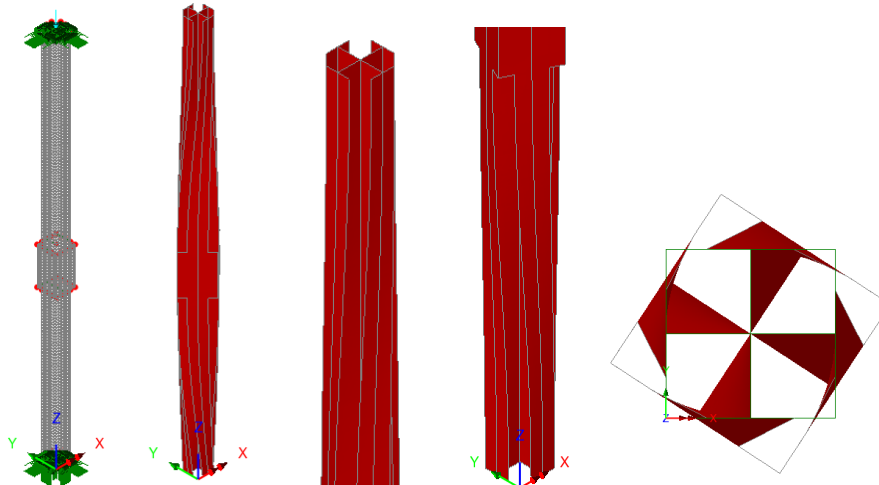


Figure 4.24 - From the left: undeformed, deformed, upper extremity, lower extremity and top view of the deformed.

It is possible to notice that the instability of mode 1 is of the torsional type, as already observed in the experimental campaign. Even that of mode 2 is of the torsional type while the instability of mode 3 is of the flexural type.

Figure 4.25 shows that the behaviour is similar to that of Model M8, exception made for the symmetry.

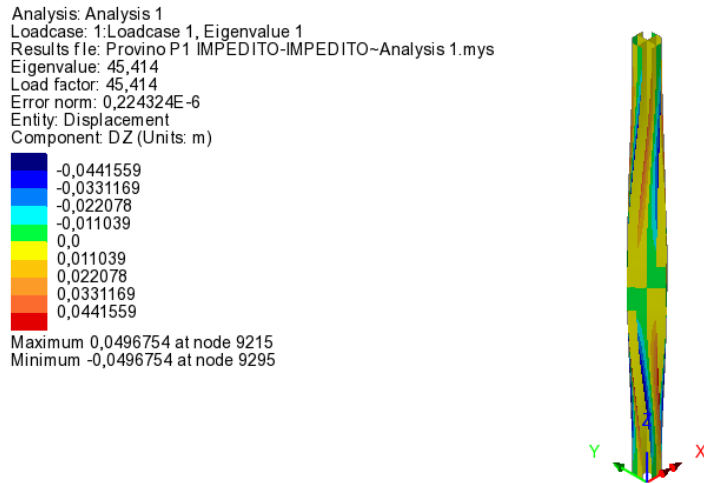


Figure 4.25 – Displacement DZ.

Model M9

Model M9 has the stiffener positioned in the interval 95-190 mm, measured from the base and it is analysed in the fully-restrained warping condition.

Table 4.9 shows the results obtained from the buckling analysis of the structure for the first 3 modes.

Mode	N_{cr}	Error
1	53.21 kN	0.95E-04
2	98 kN	0.59E-04
3	114.84 kN	0.32E-07

Table 4.9 – Buckling loads of the first 3 mode.

The undeformed and deformed models of the first mode are shown below:

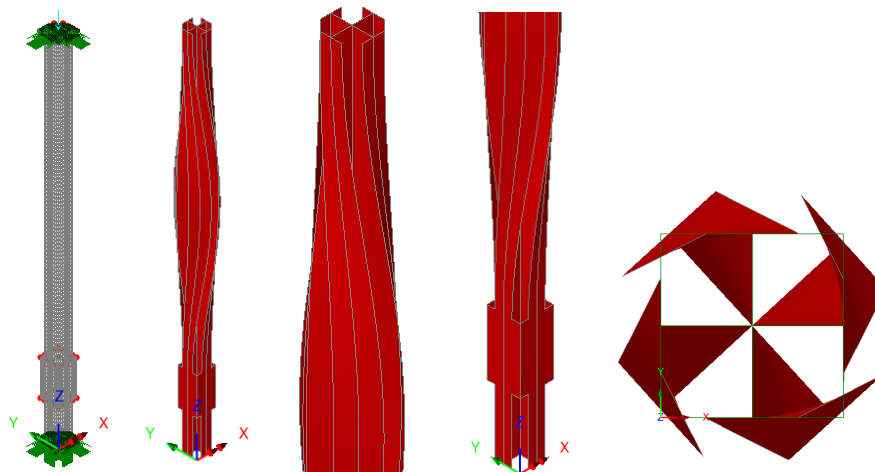


Figure 4.26 - From the left: undeformed, deformed, upper extremity, lower extremity and top view of the deformed.

It is possible to notice that the instability of mode 1 is of the torsional type, as already observed in the experimental campaign. Even that of mode 2 is of the torsional type while the instability of mode 3 is of the flexural type.

Figure 4.27 shows that warping vanishes at the ends, near the stiffened portion, and between the top and the stiffeners. The behaviour is, thus, similar to that of Model M2, but here with no warping at the top, and therefore with a stiffer response.

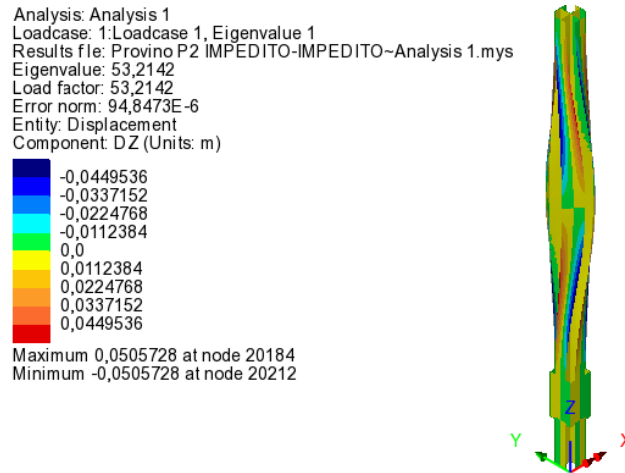


Figure 4.27 – Displacement DZ.

Model M10

Model M10 has the two stiffeners positioned in the interval 95-190 mm from each end. This model is analysed in the fully-restrained warping condition.

Table 4.10 shows the results obtained from the buckling analysis of the structure for the first 3 modes.

Mode	N_{cr}	Error
1	84.26 kN	0.54E-04
2	116.40 kN	0.30E-07
3	116.40 kN	0.65E-06

Table 4.10 – Buckling loads of the first 3 mode.

The undeformed and deformed models of the first mode are shown below:

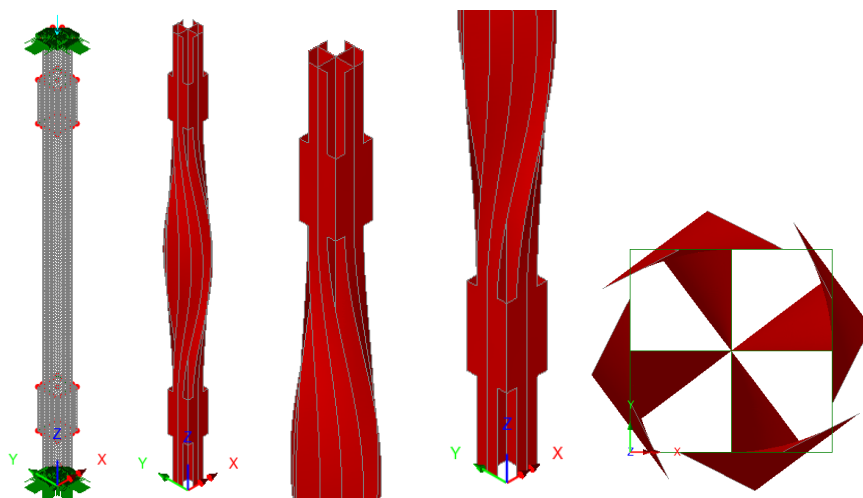


Figure 4.28 - From the left: undeformed, deformed, upper extremity, lower extremity and top view of the deformed.

It is possible to notice that the instability of mode 1 is of the torsional type, as already observed in the experimental campaign, while the ones of mode 2 and of mode 3 is of a flexural type.

Figure 4.29 shows that warping occurs only in the part comprised between the two stiffened zones, and vanishes at the mid-section because of the symmetry.

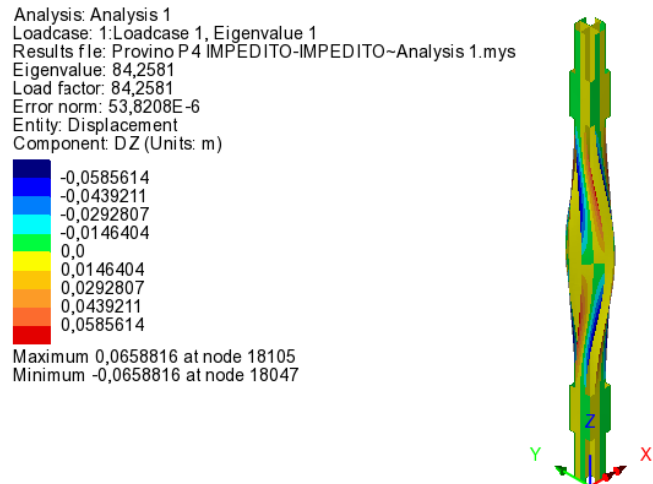


Figure 4.29 – Displacement DZ.

Model M11

Model M11 has the stiffener positioned in the interval 0-95 mm, measured from the base and it is analysed in the fully-restrained warping condition.

Table 4.11 shows the results obtained from the buckling analysis of the structure for the first 3 modes.

Mode	N_{cr}	Error
1	44.10 kN	0.11E-03
2	80.08 kN	0.32E-04
3	119.50 kN	0.32E-07

Table 4.11 – Buckling loads of the first 3 mode.

The undeformed and deformed models of the first mode are shown below:

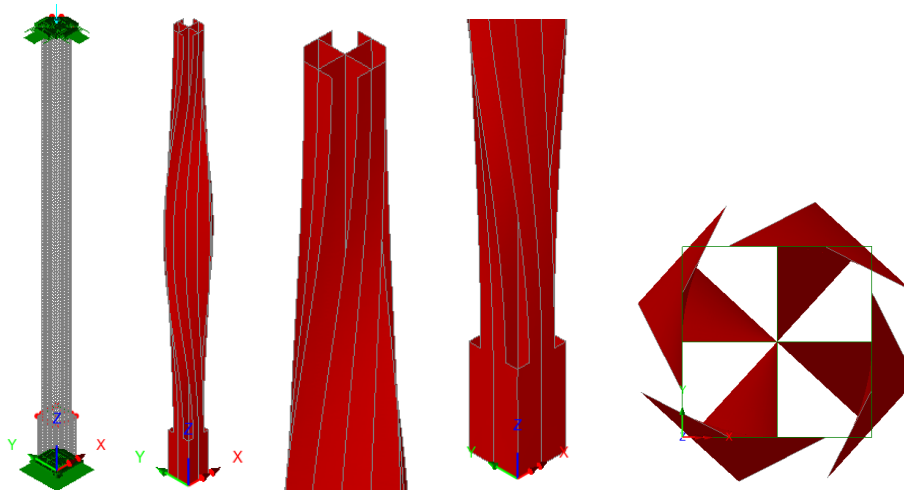


Figure 4.30 - From the left: undeformed, deformed, upper extremity, lower extremity and top view of the deformed.

It is possible to notice that the instability of mode 1 is of the torsional type, as already observed in the experimental campaign. Even that of mode 2 is of the torsional type while the instability of mode 3 is of the flexural type.

Figure 4.31 shows that warping vanishes at the top, around the stiffened zone, and in an intermediate region.

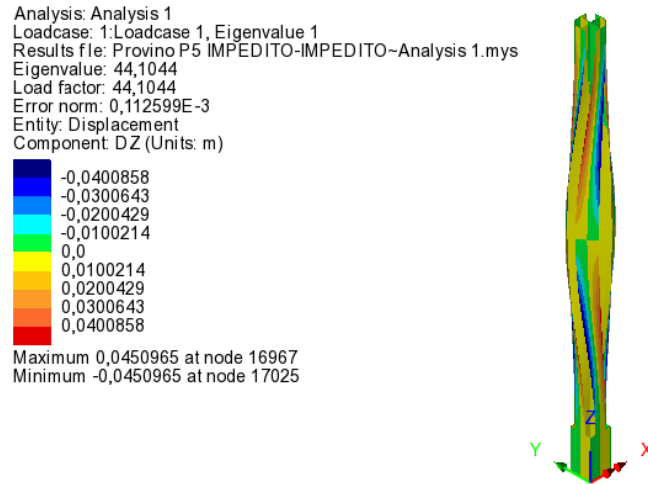


Figure 4.31 – Displacement DZ.

Model M12

Model M12 has the two stiffeners positioned in the interval 0-95 mm from each end. This model is analysed in the fully-restrained warping condition.

Table 4.12 shows the results obtained from the buckling analysis of the structure for the first 3 modes.

Mode	N_{cr}	Error
1	52.35 kN	0.15E-04
2	96.49 kN	0.59E-05
3	123.26 kN	0.26E-08

Table 4.12 – Buckling loads of the first 3 mode.

The undeformed and deformed models of the first mode are shown below:

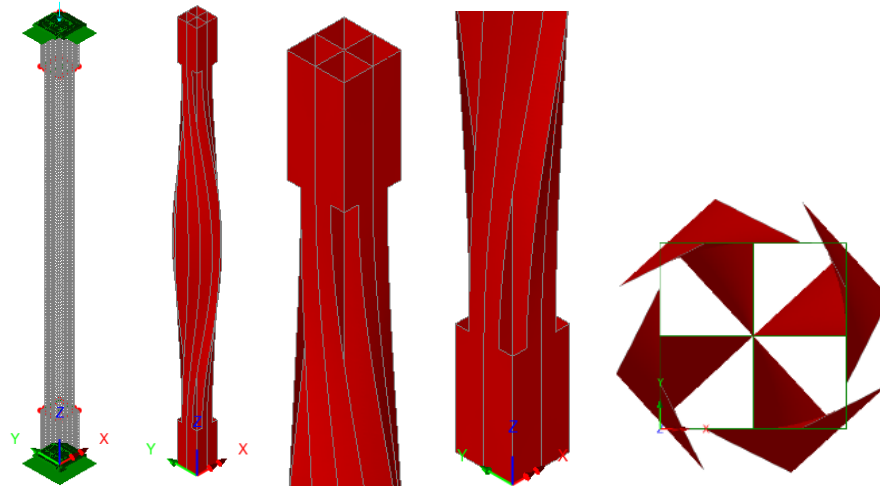


Figure 4.32 - From the left: undeformed, deformed, upper extremity, lower extremity and top view of the deformed.

It is possible to notice that the instability of mode 1 is of the torsional type, as already observed in the experimental campaign. Even that of mode 2 is of the torsional type while the instability of mode 3 is of the flexural type.

Figure 4.33 shows that warping vanishes around the stiffened zones and at mid-length, because of the symmetry.

Analysis: Analysis 1
 Loadcase: 1: Loadcase 1, Eigenvalue 1
 Results file: Provino P6 IMPEDITO-IMPEDITO-Analysis 1.mys
 Eigenvalue: 52,3487
 Load factor: 52,3487
 Error norm: 14,9396E-6
 Entity: Displacement
 Component: DZ (Units: m)

Blue	-0,044523
Dark Blue	-0,0333923
Light Blue	-0,0222615
Cyan	-0,0111308
Green	0,0
Yellow	0,0111308
Orange	0,0222615
Red	0,0333923
Dark Red	0,044523

Maximum 0,0500884 at node 16026
 Minimum -0,0500884 at node 16066



Figure 4.33 – Displacement DZ.

4.3 Mixed conditions

Once the free warping and restrained warping models were completed, the mixed conditions not analysed in the experimental campaign were studied.

The mixed condition was simulated by combining the free warping and the fully-restrained warping condition. So, the structural supports were:

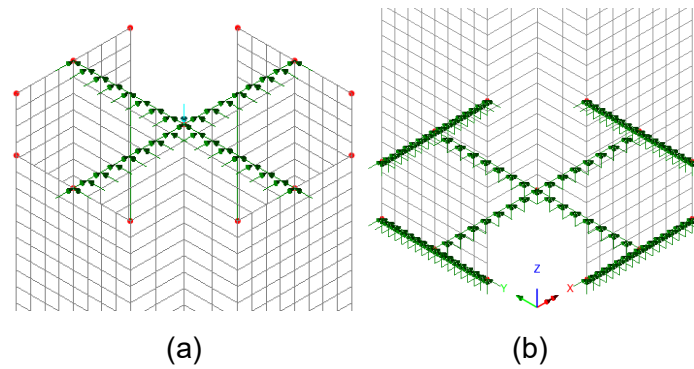


Figure 4.34 – (a) Upper constraint: warping free; (b) Lower constraints: warping restrained.

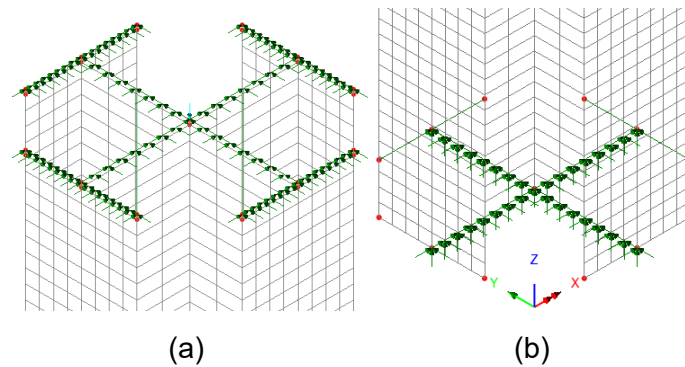


Figure 4.35 – (a) Upper constraint: warping restrained; (b) Lower constraints: warping free.

Model M13 and Model M14

Models M13 and M14 have the stiffener positioned in the interval 427,5-522,5 mm, measured from the base and these are analysed in the mixed condition.

Model M13 is constrained so that on the top, warping is prevented and on the bottom it is free, while vice versa is in model M14.

Table 4.13 shows the results obtained from the buckling analysis of the structure for the first 3 modes.

Mode	N_{cr}	Error	Mode	N_{cr}	Error
1	29.49 kN	0.83E-05	1	31.64 kN	0.12E-07
2	85.41 kN	0.19E-05	2	84.65 kN	0.21E-08
3	108.52 kN	0.14E-06	3	84.65 kN	0.12E-08

Table 4.13 – Buckling loads of the first 3 mode. Left: M13; Right: M14.

The undeformed and deformed models M13 and M14 of the first mode are shown below:

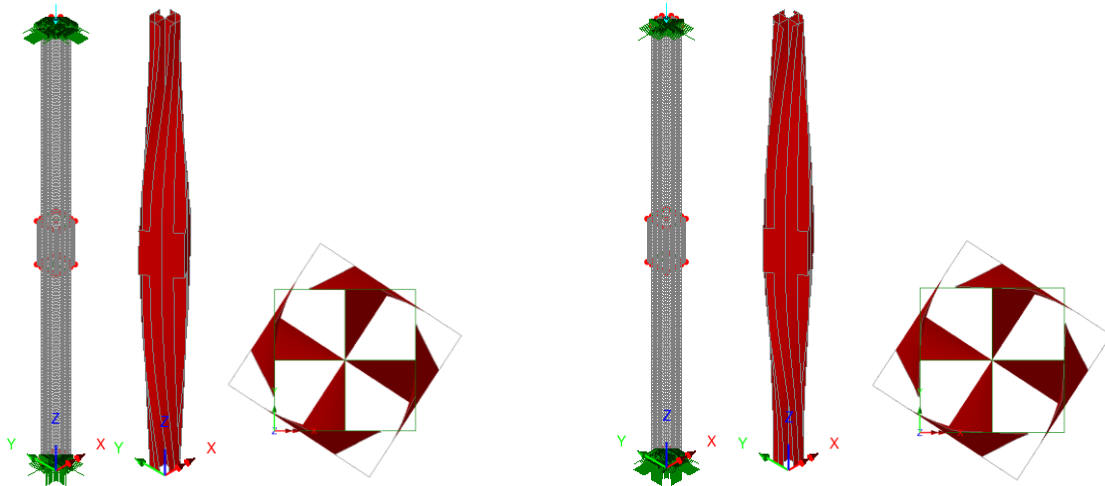


Figure 4.36 – From the left: undeformed, deformed and top view of the deformed. Left: M13; Right: M14.

For the model M13 it is possible to notice that the instability of mode 1 is of the torsional type, as already observed in the experimental campaign, as well as that of mode 2, while the instability of mode 3 is of the flexural type. For model M14 the instability of mode 1 is of the torsional type, as already observed in the experimental campaign, while that of mode 2 and of mode 3 is of the flexural type.

Focusing on the ends of the beam, the effect of the type of constraint is visible. As this is a case of mixed condition one end is deformed and the other is not.

The response in terms of longitudinal displacements field of the first buckling mode is shown in figure 4.37.

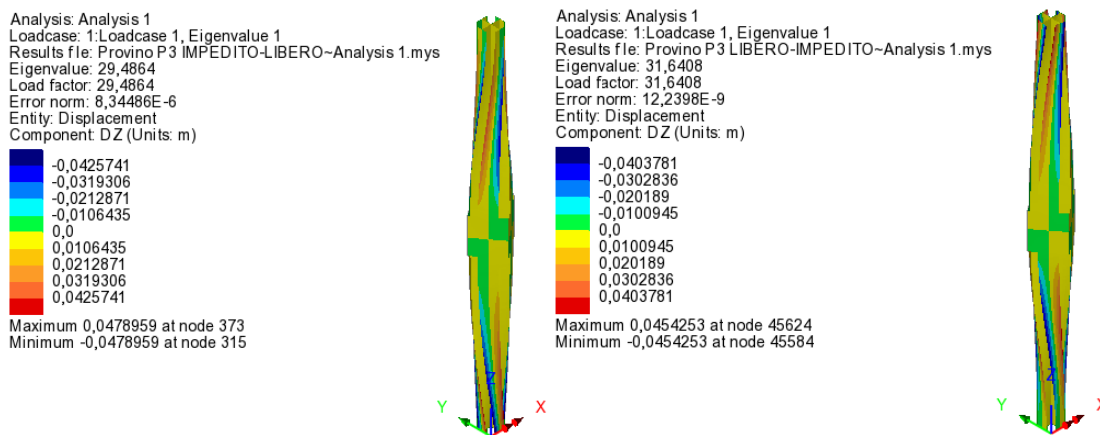


Figure 4.37 – Displacement DZ. Left: M13; Right: M14.

Model M15 and Model M16

Models M15 and M16 have the stiffener positioned in the interval 380-475 mm, measured from the base and these are analysed in the mixed condition.

Model M15 is constrained so that on the top, warping is prevented and on the bottom it is free, while vice versa is in model M16.

Table 4.14 shows the results obtained from the buckling analysis of the structure for the first 3 modes.

Mode	N_{cr}	Error	Mode	N_{cr}	Error
1	27 kN	0.90E-06	1	36.93 kN	0.12E-07
2	104.92 kN	0.34E-06	2	74.48 kN	0.71E-07
3	106.61 kN	0.41E-07	3	83.25 kN	0.23E-05

Table 4.14 – Buckling loads of the first 3 mode. Left: M15; Right: M16.

The undeformed and deformed models M15 and M16 of the first mode are shown below:

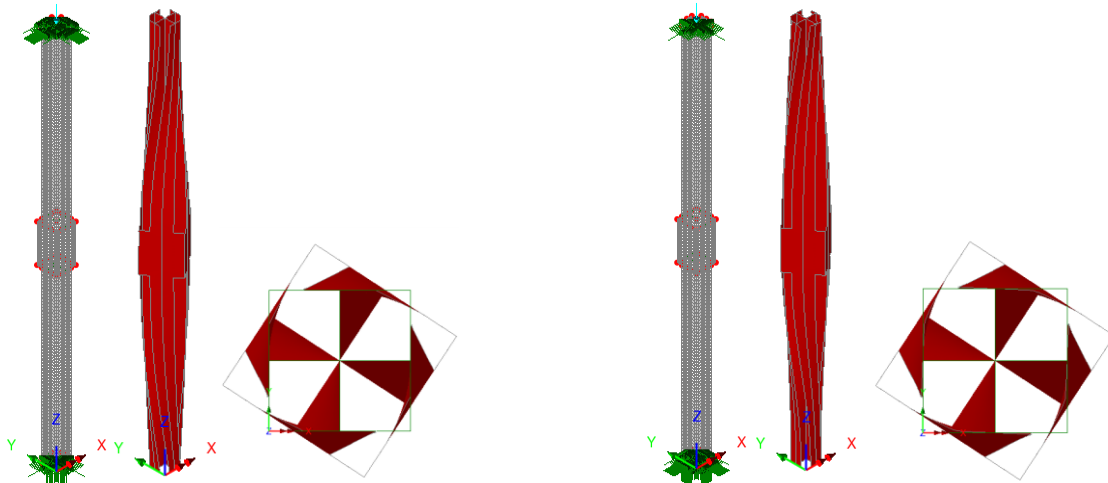


Figure 4.38 – From the left: undeformed, deformed and top view of the deformed. Left: M15; Right: M16.

Both for model M15 and model M16 it is possible to notice that the instability of mode 1 is of the torsional type, as already observed in the experimental campaign, as well as that of mode 2, while the instability of mode 3 is of the flexural type.

The response in terms of longitudinal displacements field of the first buckling mode is shown in figure 4.39.

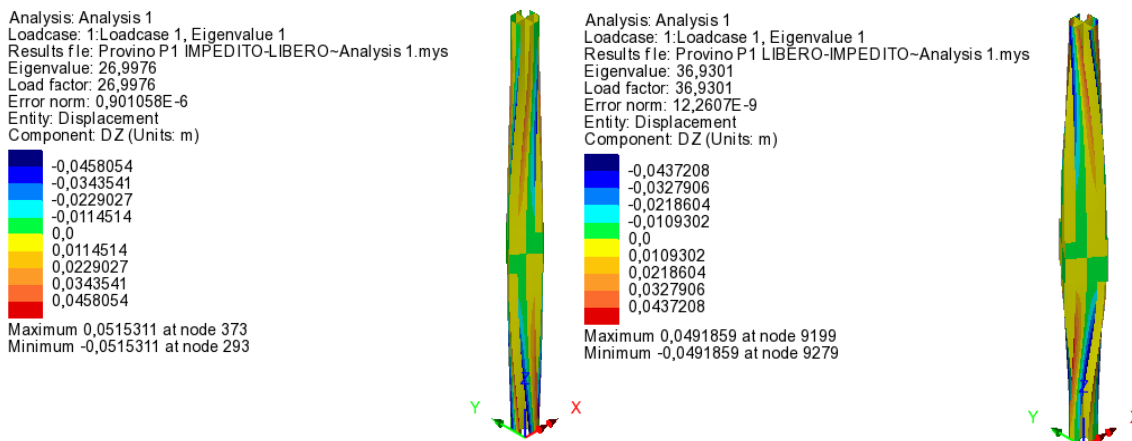


Figure 4.39 – Displacement DZ. Left: M15; Right: M16.

Model M17 and Model M18

Models M17 and M18 have the stiffeners positioned in the interval 95-190 mm, measured from the base and these are analysed in the mixed condition.

Model M17 is constrained so that on the top, warping is prevented and on the bottom it is free, while vice versa is in model M18.

Table 4.15 shows the results obtained from the buckling analysis of the structure for the first 3 modes.

Mode	N_{cr}	Error	Mode	N_{cr}	Error
1	53.21 kN	0.27E-03	1	33.92 kN	0.58E-07
2	96.78 kN	0.23E-05	2	77.56 kN	0.19E-07
3	108.55 kN	0.37E-07	3	82.87 kN	0.42E-07

Table 4.15 – Buckling loads of the first 3 mode. Left: M17; Right: M18.

The undeformed and deformed models M17 and M18 of the first mode are shown below:

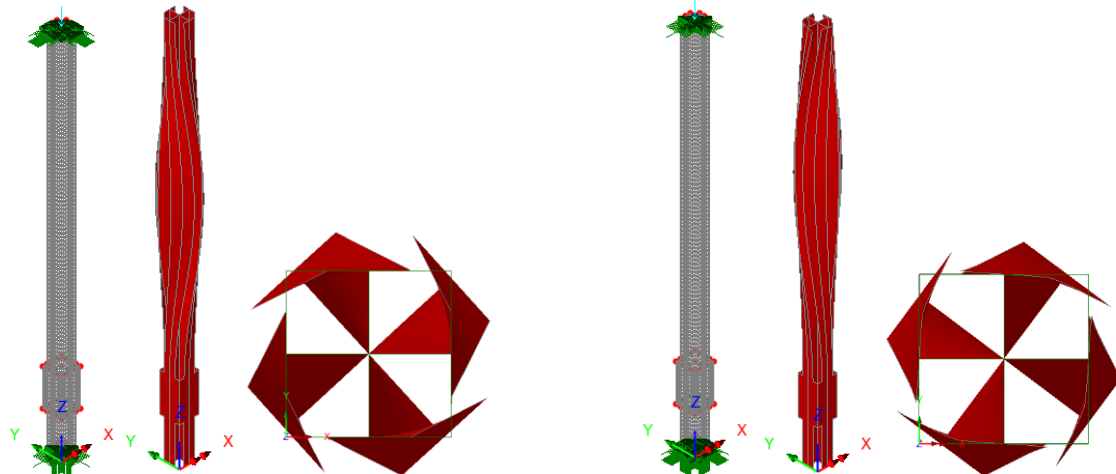


Figure 4.40 – From the left: undeformed, deformed and top view of the deformed. Left: M17; Right: M18.

Both for model M17 and model M18 it is possible to notice that the instability of mode 1 is of the torsional type, as already observed in the experimental campaign, as well as that of mode 2, while the instability of mode 3 is of the flexural type.

The response in terms of longitudinal displacements field of the first buckling mode is shown in figure 4.41.

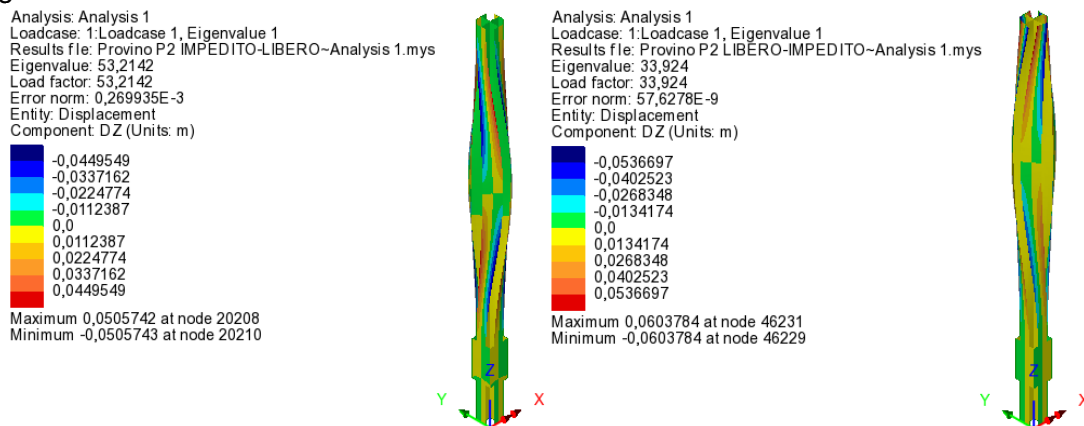


Figure 4.41 – Displacement DZ. Left: M17; Right: M18.

Model M19 and Model M20

Models M19 and M20 have the two stiffeners positioned in the interval 95-190 mm from each end. This models are analysed in the mixed condition.

Model M19 is constrained so that on the top, warping is prevented and on the bottom it is free, while vice is versa in model M20.

Table 4.16 shows the results obtained from the buckling analysis of the structure for the first 3 modes.

Mode	N_{cr}	Error	Mode	N_{cr}	Error
1	84.26 kN	0.43E-05	1	84.56 kN	0.70E-09
2	104.31 kN	0.48E-06	2	85.96 kN	0.15E-07
3	104.31 kN	0.63E-08	3	85.96 kN	0.23E-07

Table 4.16 – Buckling loads of the first 3 mode. Left: M19; Right: M20.

The undeformed and deformed models M19 and M20 of the first mode are shown below:

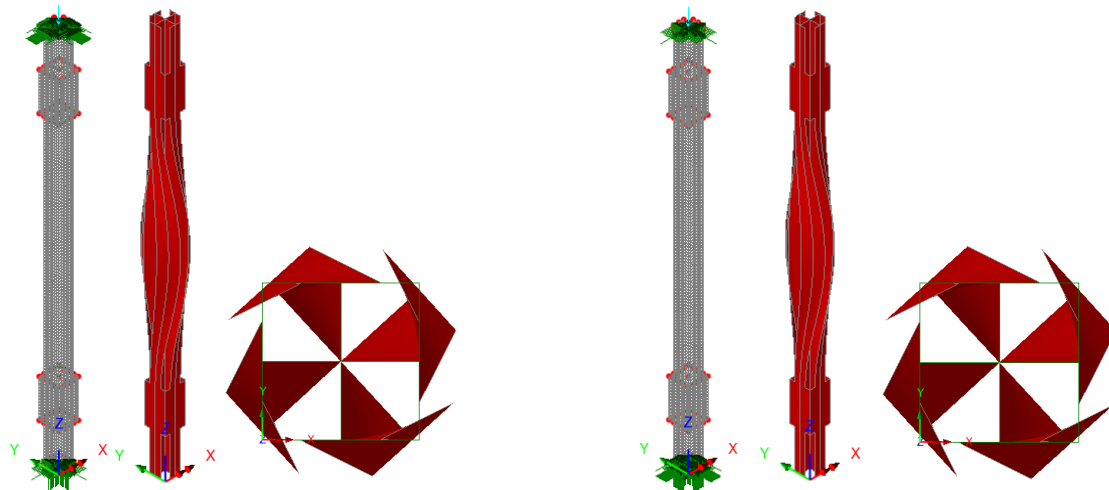


Figure 4.42 – From the left: undeformed, deformed and top view of the deformed. Left: M19; Right: M20.

Both for model M19 and model M20 it is possible to notice that the instability of mode 1 is of the torsional type, as already observed in the experimental campaign, while that of mode 2 and of mode 3 is of a flexural type.

The response in terms of longitudinal displacements field of the first buckling mode is shown in figure 4.43.

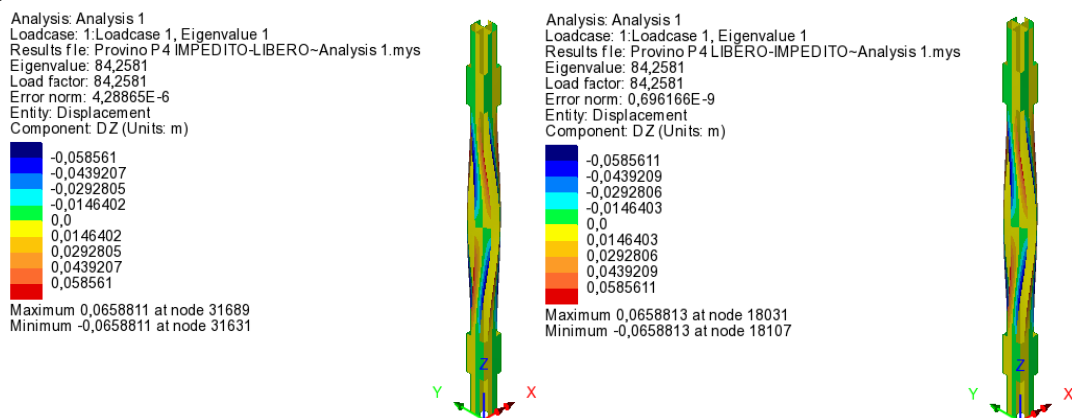


Figure 4.43 – Displacement DZ. Left: M19; Right: M20.

Model M21 and Model M22

Models M21 and M22 have the stiffeners positioned in the interval 0-95 mm, measured from the base and these are analysed in the mixed condition.

Model M21 is constrained so that on the top, warping is prevented and on the bottom it is free, while vice versa is in model M22.

Table 4.17 shows the results obtained from the buckling analysis of the structure for the first 3 modes.

Mode	N_{cr}	Error	Mode	N_{cr}	Error
1	44.10 kN	0.52E-03	1	28.67 kN	0.75E-07
2	80.07 kN	0.49E-04	2	63.64 kN	0.45E-07
3	110.34 kN	0.13E-04	3	86.39 kN	0.13E-05

Table 4.17 – Buckling loads of the first 3 mode. Left: M21; Right: M22.

The undeformed and deformed models M21 and M22 of the first mode are shown below:

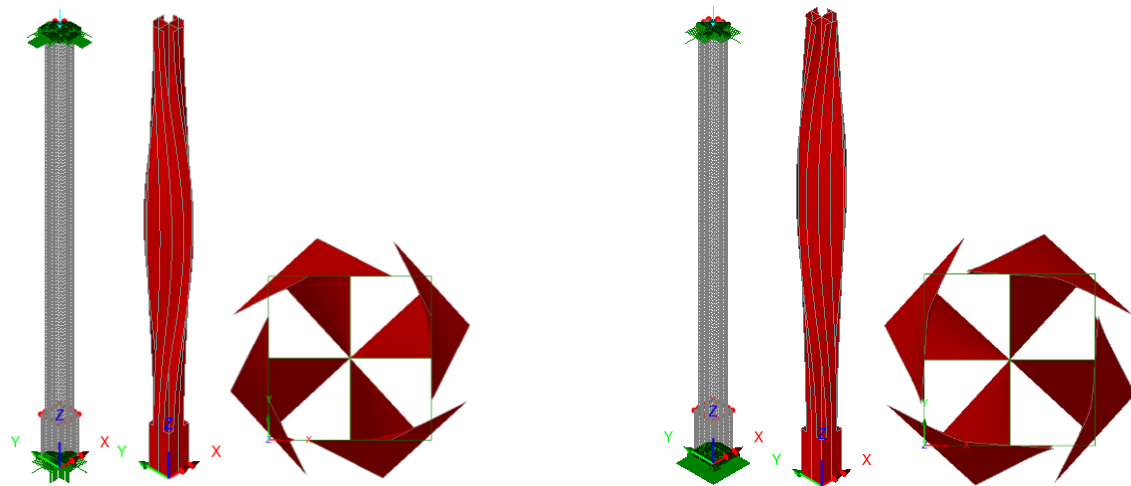


Figure 4.44 – From the left: undeformed, deformed and top view of the deformed. Left: M21; Right: M22.

Both for model M21 and model M22 it is possible to notice that the instability of mode 1 is of the torsional type, as already observed in the experimental campaign, as well as that of mode 2, while the instability of mode 3 is of the flexural type.

The response in terms of longitudinal displacements field of the first buckling mode is shown in figure 4.45.

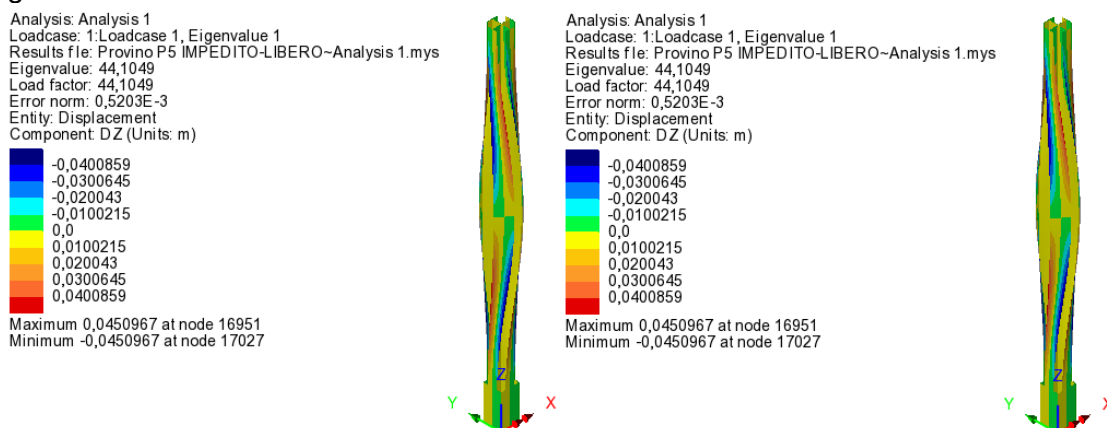


Figure 4.45 – Displacement DZ. Left: M21; Right: M22.

Model M23 and Model M24

Models M23 and M24 have the two stiffeners positioned in the interval 0-95 mm from each end. These models are analysed in the mixed condition.

Model M23 is constrained so that on the top, warping is prevented and on the bottom it is free, while vice versa is in model M24.

Table 4.18 shows the results obtained from the buckling analysis of the structure for the first 3 modes.

Mode	N_{cr}	Error	Mode	N_{cr}	Error
1	52.35 kN	0.93E-04	1	52.35 kN	0.19E-05
2	96.49 kN	0.66E-05	2	87.52 kN	0.15E-06
3	113.73 kN	0.17E-06	3	87.52 kN	0.22E-06

Table 4.18 – Buckling loads of the first 3 mode. Left: M23; Right: M24.

The undeformed and deformed models M23 and M24 of the first mode are shown below:

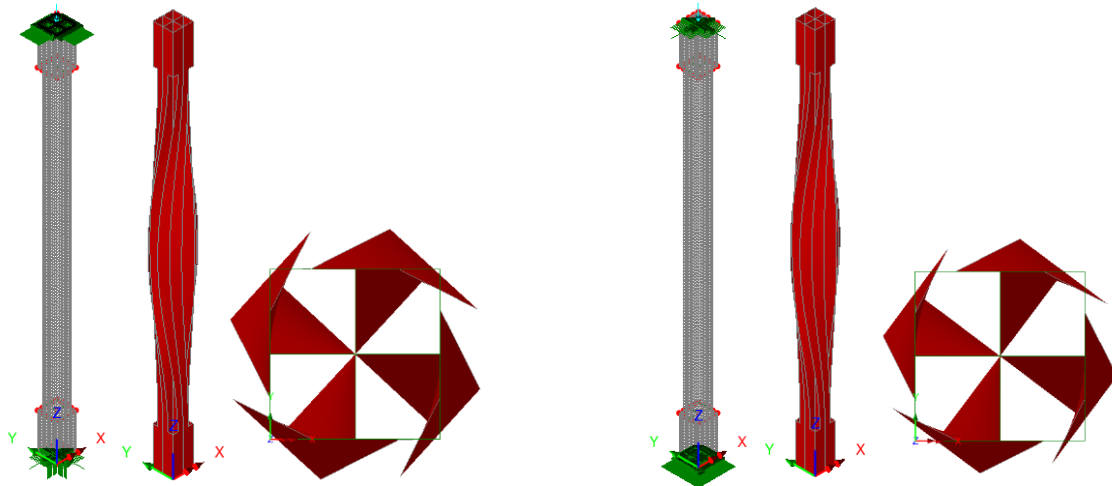


Figure 4.46 – From the left: undeformed, deformed and top view of the deformed. Left: M23; Right: M24.

For the model M23 it is possible to notice that the instability of mode 1 is of the torsional type, as already observed in the experimental campaign, as well as that of mode 2, while the instability of mode 3 is of the flexural type. For model M24 the instability of mode 1 is of the torsional type, as already observed in the experimental campaign, while that of mode 2 and of mode 3 is of the flexural type.

The response in terms of longitudinal displacements field of the first buckling mode is shown in figure 4.47.

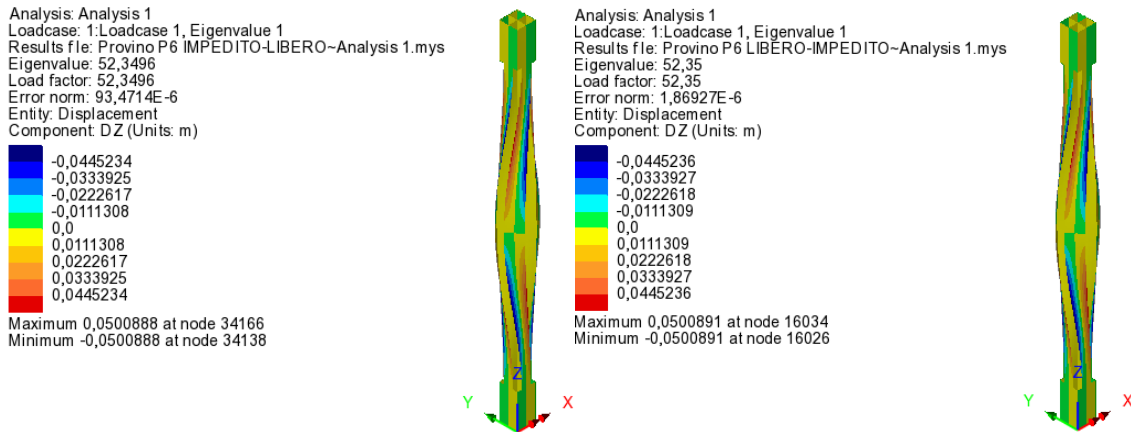


Figure 4.47 – Displacement DZ. Left: M23; Right: M24.

4.4 Further models

To complete the study and to understand what is the best position of the stiffener, six further models have been studied in both free warping and fully-restrained warping conditions.

Model M25 and Model M26

Models M25 and M26 have the stiffener positioned in the interval 190-285 mm, measured from the base.

Model M25 is analysed in the free warping condition while model M26 in the fully-restrained warping condition.

Table 4.19 shows the results obtained from the buckling analysis of the structure for the first 3 modes.

Mode	N_{cr}	Error	Mode	N_{cr}	Error
1	39.01 kN	0.25E-07	1	59.96 kN	0.69E-07
2	46.57 kN	0.21E-07	2	59.96 kN	0.46E-07
3	52.9 kN	0.71E-04	3	62.53 kN	0.70E-09

Table 4.19 – Buckling loads of the first 3 mode. Left: M25; Right: M26.

The undeformed and deformed models M25 and M26 of the first mode are shown below:

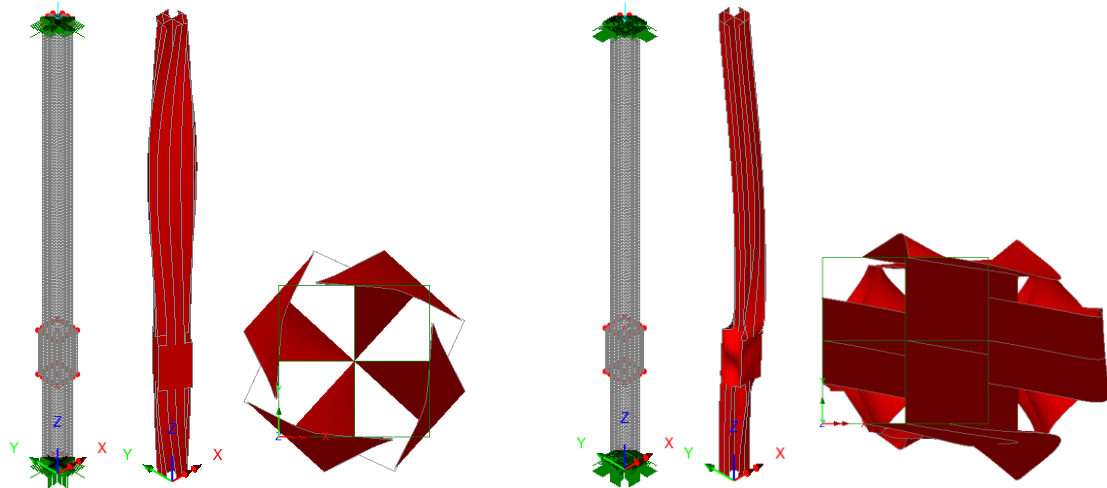


Figure 4.48 – From the left: undeformed, deformed and top view of the deformed. Left: M25; Right: M26.

For the model M25 it is possible to notice that the instability of mode 1 is of the torsional type as well as that of mode 2, while the instability of mode 3 is of the flexural type. For model M26 the instability of the first three modes is of the flexural type with local buckling phenomena.

The response in terms of longitudinal displacements field of the first buckling mode is shown in figure 4.49.

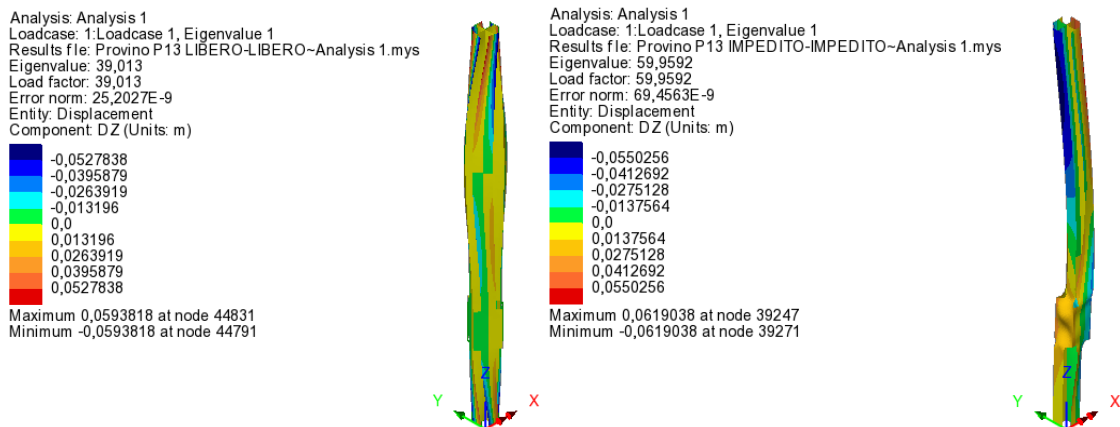


Figure 4.49 – Displacement DZ. Left: M25; Right: M26.

Model M27 and Model M28

Models M27 and M28 have the two stiffeners positioned in the interval 190-285 mm from each end.

Model M27 is analysed in the free warping condition while model M28 in the fully-restrained warping condition.

Table 4.20 shows the results obtained from the buckling analysis of the structure for the first 3 modes.

Mode	N_{cr}	Error	Mode	N_{cr}	Error
1	51.40 kN	0.99E-10	1	60.21 kN	0.36E-06
2	53.76 kN	0.15E-09	2	60.21 kN	0.93E-06
3	53.76 kN	0.19E-09	3	62.53 kN	0.19E-07

Table 4.20 – Buckling loads of the first 3 mode. Left: M27; Right: M28.

The undeformed and deformed models M27 and M28 of the first mode are shown below:

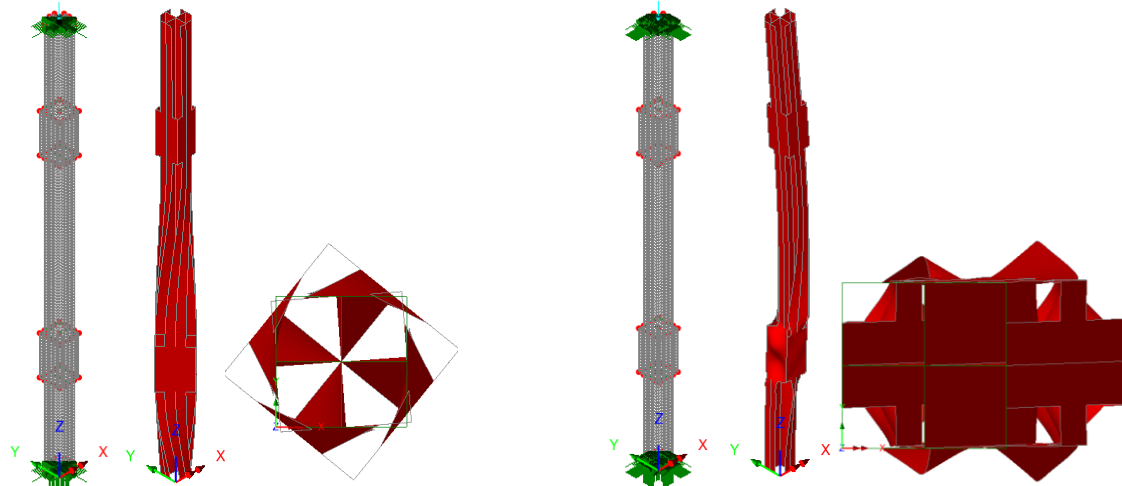


Figure 4.50 – From the left: undeformed, deformed and top view of the deformed. Left: M27; Right: M28.

For the model M27 it is possible to notice that the instability of mode 1 is of the torsional type, while that of mode 2 and of mode 3 is of the flexural type. For model M28 the instability of the first three modes is of the flexural type with local buckling phenomena.

The response in terms of longitudinal displacements field of the first buckling mode is shown in figure 4.51.

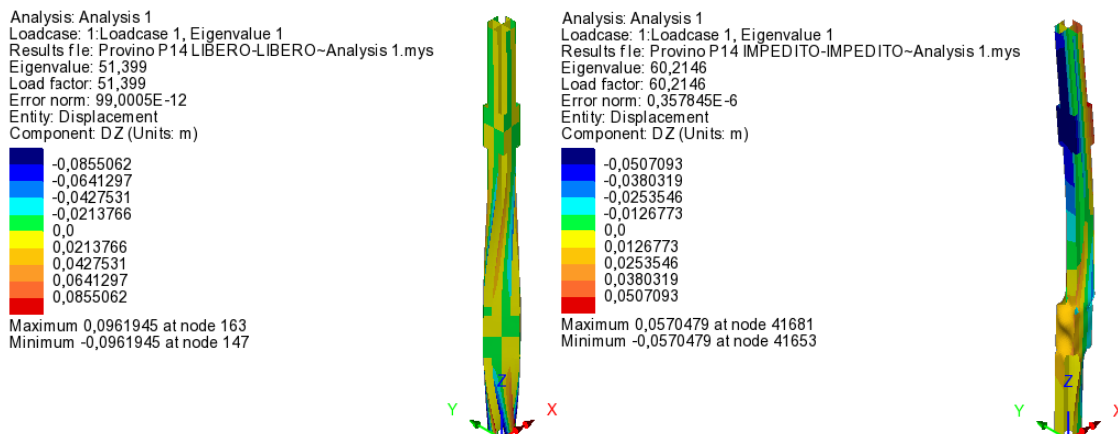


Figure 4.51 – Displacement DZ. Left: M27; Right: M28.

Model M29 and Model M30

Models M29 and M30 have the two stiffeners positioned in the interval 285-380 mm from each end.

Model M29 is analysed in the free warping condition while model M30 in the fully-restrained warping condition.

Table 4.21 shows the results obtained from the buckling analysis of the structure for the first 3 modes.

Mode	N_{cr}	Error	Mode	N_{cr}	Error
1	30.06 kN	0.14E-07	1	83.94 kN	0.18E-04
2	84.45 kN	0.24E-05	2	125.06 kN	0.26E-06
3	84.45 kN	0.75E-07	3	125.17 kN	0.27E-06

Table 4.21 – Buckling loads of the first 3 mode. Left: M29; Right: M30.

The undeformed and deformed models M29 and M30 of the first mode are shown below:

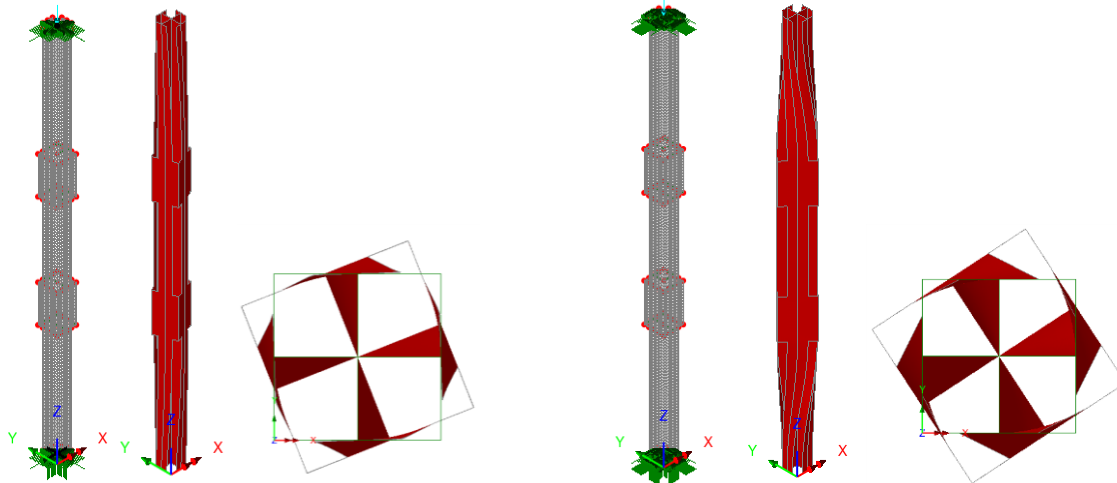


Figure 4.52 – From the left: undeformed, deformed and top view of the deformed. Left: M29; Right: M30.

Both for model M29 and model M30 it is possible to notice that the instability of mode 1 is of the torsional type, while that of mode 2 and of mode 3 is of the flexural type.

The response in terms of longitudinal displacements field of the first buckling mode is shown in figure 4.53.

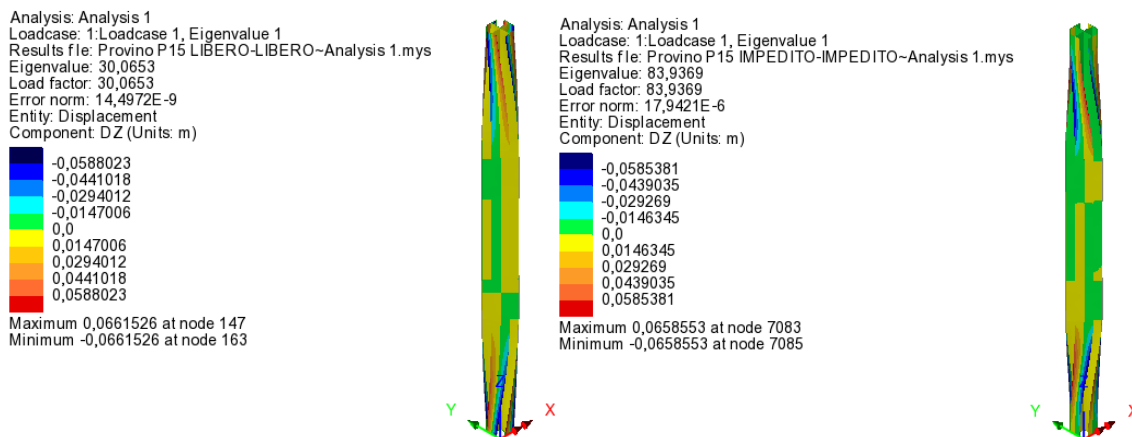


Figure 4.53 – Displacement DZ. Left: M29; Right: M30.

4.5 Comparisons between numerical simulations and experimental campaign

Table 4.22 shows the critical stresses that will be compared with yield stress to understand if the specimen before reaching the buckling load has become yielded.

$$\sigma_{cr,e} = \frac{N_{cr,e}}{A}$$

Where:

- $A = 251,84 \text{ mm}^2$;

	Model	$N_{cr,e}$	$\sigma_{cr,e}$	Elastic Buckling ($\sigma_{cr,e} < \sigma_y$)
	M1	18,79	74,61	Yes
	M2	33,9	134,61	Yes
	M3	18,34	72,82	Yes
	M4	81,15	322,23	No
	M5	28,67	113,84	Yes
	M6	52,35	207,87	No
	M7	43,34	172,09	No
	M8	45,41	180,31	No
	M9	53,21	211,28	No
	M10	84,26	334,58	No
	M11	44,1	175,11	No
	M12	52,35	207,87	No
	M13	29,45	116,94	Yes
	M14	31,6	125,48	Yes
	M15	27	107,21	Yes
	M16	36,93	146,64	No
	M17	53,21	211,28	No
	M18	33,9	134,61	Yes
	M19	84,26	334,58	No
	M20	84,26	334,58	No
	M21	44,1	175,11	No
	M22	28,67	113,84	Yes
	M23	52,35	207,87	No
	M24	52,35	207,87	No
	M25	39	154,86	No
	M26	59,95	238,05	No
	M27	51,4	204,10	No
	M28	60,21	239,08	No
	M29	30,07	119,40	Yes
	M30	83,94	333,31	No

Table 4.22 - Results of numerical simulations, elastic critical stress and yield test.

The yield stress range of 6060-T5 aluminum alloy is between 120 MPa and 165 MPa. To evaluate if the model was subject to elastic buckling, the average value of yield stress range was considered.

When the beam is not yielded, σ_{cr} must be less than the yield stress $\sigma_y = 142,5$ MPa. So, through the comparison among this two stresses it was understood if the model collapse for instability or it was yielded. Table 4.22 shows for what models the buckling load is really had. To understand which numerical and experimental values can be compared, it was necessary to evaluate the critical stress it in the elasto-plastic range. This was obtained by referring to Johnson's parabola as for the flexural buckling. There may be two cases:

- $\sigma_{cr,e} < \sigma_e \rightarrow N_{cr} = N_{cr,e}$, there is elastic instability;
- $\sigma_{cr,e} > \sigma_e \rightarrow \sigma_{cr,ep} = \sigma_s - \frac{\sigma_s^2}{4 \sigma_{cr,e}} \rightarrow N_{cr} = \sigma_{cr,ep} A$, there is elasto-plastic instability.

Where

- $\sigma_e = \frac{\sigma_y}{2}$.

So, instability has existed for all models, or in the elastic range or in the elasto-plastic range, in how much all have been subject to a torsion produced by a compression of the same model.

Model	$\sigma_{y,min}$			$\sigma_{y,max}$		
	$N_{cr,e}$ (kN)	$\sigma_{cr,e}$ (MPa)	$\sigma_{cr,ep}$ (MPa)	$N_{cr,ep}$ (kN)	$\sigma_{cr,ep}$ (MPa)	$N_{cr,ep}$ (kN)
M1	18,79	74,61	71,75	18,07	-	18,79
M2	33,9	134,61	93,26	23,49	114,44	28,82
M3	18,34	72,82	70,57	17,77	-	18,34
M4	81,15	322,23	108,83	27,41	143,88	36,23
M5	28,67	113,84	88,38	22,26	105,21	26,50
M6	52,35	207,87	102,68	25,86	132,26	33,31
M7	43,34	172,09	99,08	24,95	125,45	31,59
M8	45,41	180,31	100,03	25,19	127,25	32,05
M9	53,21	211,28	102,96	25,93	132,79	33,44
M10	84,26	334,58	109,24	27,51	144,66	36,43
M11	44,1	175,11	99,44	25,04	126,13	31,77
M12	52,35	207,87	102,68	25,86	132,26	33,31
M13	29,45	116,94	89,21	22,47	106,80	26,90
M14	31,6	125,48	91,31	23,00	110,76	27,89
M15	27	107,21	86,42	21,76	101,52	25,57
M16	36,93	146,64	95,45	24,04	118,59	29,86

M17	53,21	211,28	102,96	25,93	132,79	33,44
M18	33,9	134,61	93,26	23,49	114,44	28,82
M19	84,26	334,58	109,24	27,51	144,66	36,43
M20	84,26	334,58	109,24	27,51	144,66	36,43
M21	44,1	175,11	99,44	25,04	126,13	31,77
M22	28,67	113,84	88,38	22,26	105,21	26,50
M23	52,35	207,87	102,68	25,86	132,26	33,31
M24	52,35	207,87	102,68	25,86	132,26	33,31
M25	39	154,86	96,75	24,37	121,05	30,48
M26	59,95	238,05	104,88	26,41	136,41	34,35
M27	51,4	204,10	102,36	25,78	131,65	33,16
M28	60,21	239,08	104,94	26,43	136,53	34,38
M29	30,07	119,40	89,85	22,63	108,00	27,20
M30	83,94	333,31	109,20	27,50	144,58	36,41

Table 4.23 – Critical load in elasto-plastic range

From the analysed models it is evident as the type of constraint influences the behaviour of the beam.

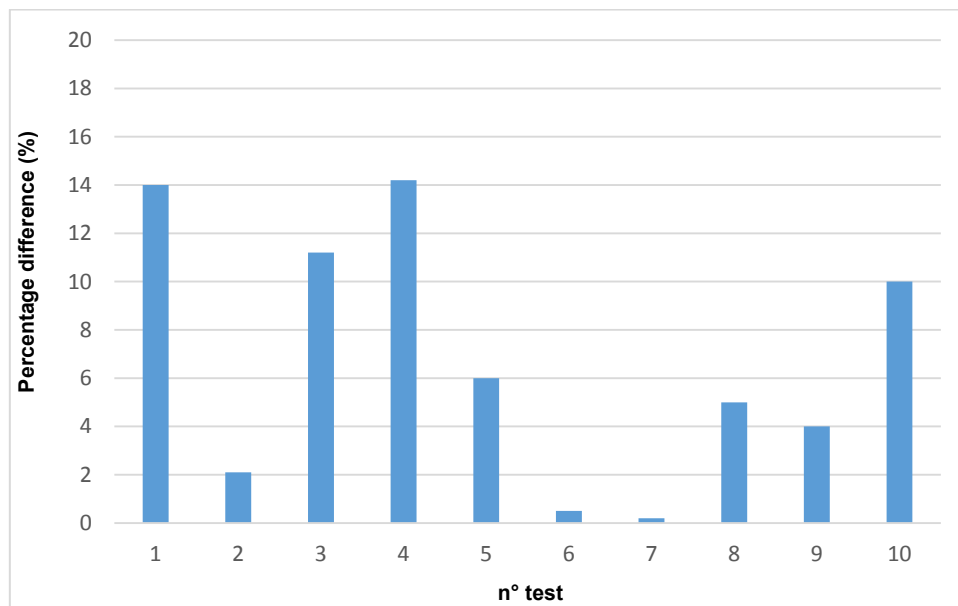
To make comparisons between numerical and experimental results, the minimum yield stress was considered because it provided buckling load results more similar to the experimental ones.

Comparisons between the results are shown in table 4.24.

Name	Type of constraint	Numerical buckling load (N _{c,num})	Experimental buckling load (N _{c,exp})	Percentage different $(N_{c,num} - N_{c,exp}) / N_{c,exp} \times 100$
M1-S1	Free warping	18.07 kN	21 kN	-14 %
M8-S8	Restrained warping	25.19 kN	24 kN	5%
M15	Mixed condition	21.76 kN	-	-
M16	Mixed condition	24.04 kN	-	-
M2-S2	Free warping	23.49 kN	23 kN	2.1 %
M9-S9	Restrained warping	25.93 kN	27 kN	-4 %
M17	Mixed condition	25.93 kN	-	-
M18	Mixed condition	23.49 kN	-	-
M3-S3	Free warping	17.77 kN	20 kN	-11.2 %
M7-S7	Restrained warping	24.95 kN	25 kN	-0.2 %
M13	Mixed condition	22.47 kN	-	-
M14	Mixed condition	23 kN	-	-
M4-S4	Free warping	27.41 kN	24 kN	14.2 %
M10-S10	Restrained warping	27.51 kN	25 kN	10 %
M19	Mixed condition	27.51 kN	-	-
M20	Mixed condition	27.51 kN	-	-
M5-S5	Free warping	22.26 kN	21 kN	6 %
M11-S11	Restrained warping	25.04 kN	unreliable	-
M21	Mixed condition	25.04 kN	-	-
M22	Mixed condition	22.26 kN	-	-
M6-S6	Free warping	25.86 kN	26 kN	-0.5 %
M12-S12	Restrained warping	25.86 kN	unreliable	-
M23	Mixed condition	25.86 kN	-	-
M24	Mixed condition	25.86 kN	-	-

Table 4.24 - Comparison between numerical and experimental results.

Graph 4.1 shows the percentage differences between numerical and experimental results.



Graph 4.1 – Percentage difference between numerical and experimental results

As already mentioned in chapter 3, the experimental results of specimens S11 and S12 are not correct because the welding of the stiffeners in contact with the constraints has distorted the test. The results of these cases are thus unreliable.

4.6 Comparisons between stiffened, uniform and weakened beam

It was interesting to compare the FEM results obtained from the stiffened beam with those of the beam without stiffeners (uniform beam) and of the beam with a local reduction of the warping stiffness represented by the absence of the flanges for a beam portion 1 cm long placed at one fourth of the beam length (see Piana et al., 2017c).

	Uniform beam	Stiffened beam	Weakened beam
	N _{cr} FEM (kN)	N _{cr} FEM (kN)	N _{cr} FEM (kN)
Free warping	16.5	39	9.8
Fully-restrained warping	38.4	59.95	29.6

Table 4.24 - Comparisons of FEM buckling loads of the stiffened, uniform and weakened beam

In this thesis, beams were analysed with stiffener in different positions. In the table 4.24 the beam was considered with the stiffener placed at $y = 237.5$ mm. In this way it is possible to compare with the weakened beam with damage placed at $y = 240$ mm. It must be observed, however, that the stiffening and the weakening have different lengths.

4.7 Comparisons between beams with different stiffener

The article by Svensson and Plum, entitled "Stiffener Effects on Torsional Buckling of Columns" cited in chapter 1, presents an analytical evaluation of the effect of locally placed stiffeners.

Figure 1.7 shows an analogy between the section studied in that article and the one of this thesis. The stiffened section, in one case is octagonal while in the other it is squared. For this reason, to make a comparison between the two studies, through the use of LUSAS it was possible to obtain the buckling load. Two models were compared in two different warping restraint conditions, free warping and fully restrained warping. The length of the beams is 950 mm while the stiffener length is 95 mm.

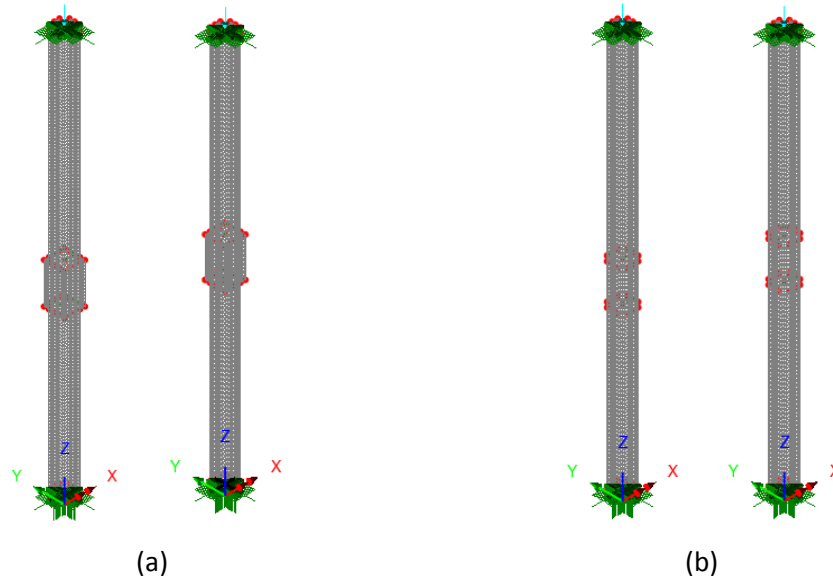


Figure 3.54 – (a) Models of this thesis; (b) Models of the article

In first model the stiffening is placed at $y = 475$ mm while in second model at $y = 427.5$ mm. By setting an eigenvalue problem it was possible to obtain the buckling loads of the different models. Table 4.25 shows buckling loads.

	Free warping		Fully restrained warping	
	Thesis	Article	Thesis	Article
M1	18.79 kN	18.52 kN	45.41 kN	44.36 kN
M2	18.34 kN	18.09 kN	43.34 kN	41.56 kN

Table 4.25 - Comparison between buckling loads

The buckling load values between thesis and scientific paper are only slightly different. The instability of all the analysed models is torsional.

Both types of stiffener represent constraints to cross-sectional warping. The one studied in this thesis stiffens more but is more difficult to realise in practice, while that of the article stiffens less but is easier to realise.

Chapter 5

Conclusion and future developments

The aim of this thesis was to analyze the structural instability of open thin-walled beams. Specifically, numerical and experimental investigation were conducted to analyze the static behaviour (torsional instability due to compression) of beams with cruciform section with flanges, stiffened by longitudinal plates located in different positions.

Different end constraint conditions were analyzed: warping free at both ends, warping restrained at both ends, and the mixed conditions. So, the buckling load was identified both numerically and, for the previous two constraint conditions, experimentally, for a subsequent comparison.

In addition to the finite element program (Lusas), the LabVIEW programming software was essential to achieve the result.

In the experimental campaign a laser displacement transducer was used to register the transverse displacement at a point (see Chapter 3). This was done to identify buckling occurrence from axial load vs. transverse displacement curves, in addition to the axial load-axial displacement curves given by the MTS.

Through this study, it was clear that all the beams were subject to instability. For some the instability occurred in the elastic range while for others in the elasto-plastic range.

The beams analyzed had one or two stiffeners. The search of buckling load made it possible to identify the optimal position of the stiffener(s). Therefore, from the results we deduce that the stiffeners must be placed where the warping is maximum in the unstiffened beam.

Considering the beam with only one stiffener in the conditions of both free and restrained warping, the ideal position of the stiffener is around $L/4$ from an end.

On the other hand, considering the beam with two stiffeners in the condition of both free and restrained warping, the ideal stiffeners position is approximately $L/8$ from the ends for both upper and lower stiffener.

In the first case, in the free warping condition the buckling load value is 39 kN while, in the restrained warping condition of 59.95 kN. In the second case, in the free warping condition the buckling load value is 81.15 kN while, in the restrained warping condition of 84.26 kN. The previous values were obtained from finite element models. Below are shown the models with optimal position of stiffeners.

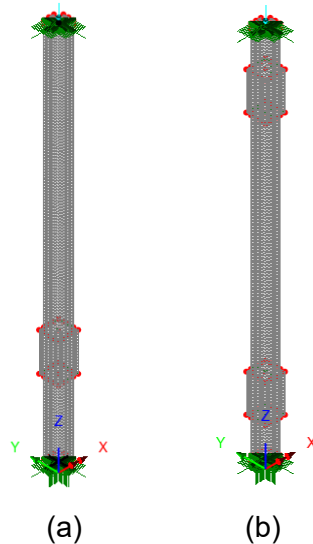


Figure 5.1 – Optimal model: (a) with only one stiffener; (b) with two stiffeners.

The work of this thesis was very interesting because there are no closed solutions of these beams with this particular section. For this reason, it was necessary to conduct an experimental campaign with an parallel numerical analysis, fundamental to validate the experimental results.

Possible developments of the present study may concern the analysis of the flexural-torsional instability in section beams with a single axis of symmetry or without symmetry axes. A further step forward in the study could instead have as its object the stability of thin-wall beams subject to transverse loading.

References

- [1] G. Piana, E. Lofrano, A. Manuello, G. Ruta, A. Carpinteri, *Compressive buckling for symmetric TWB with non-zero warping stiffness*, Engineering Structures, 135, 246-258, 2017.
- [2] G. Piana, E. Lofrano, A. Carpinteri, G. Ruta, *Buckling of an open thin-walled beam with an intermediate stiffener*, Aimeta, Salerno, Italy, 4-7 September, 2017.
- [3] G. Piana, A. Carpinteri, E. Lofrano, G. Ruta, *Vibration and buckling of open TWBs with local weakening*, Procedia Engineering, 199, 242-247, 2017.
- [4] P. Gelfi, *Torsione da ingobbamento impedito*.
http://gelfi.unibs.it/lezioni_acciaio/Lezione10.pdf
- [5] I. Kreja, C. Szymczak, *Numerical simulation of a thin-walled beam with warping stiffeners undergoing torsion*, Task Quarterly 6 No 3, 453-460, 2002.
- [6] S. E. Svensson, C. M. Plum, *Stiffener effects on torsional buckling of columns*, Struct. Engng., ASCE, 109 758, 1983.
- [7] V. Franciosi, *Instabilità torsio-flessionale delle travi compresse*, Scienza delle Costruzioni Vol. 5, Chapter 7, Liguori editore, Napoli 1967.
- [8] M. Tonici, *Indagini sperimentali sulla dinamica e la stabilità di elementi snelli mediante l'utilizzo di sensori piezoelettrici*, Tesi di laurea magistrale in Ingegneria civile, Politecnico di Torino, Luglio 2015.